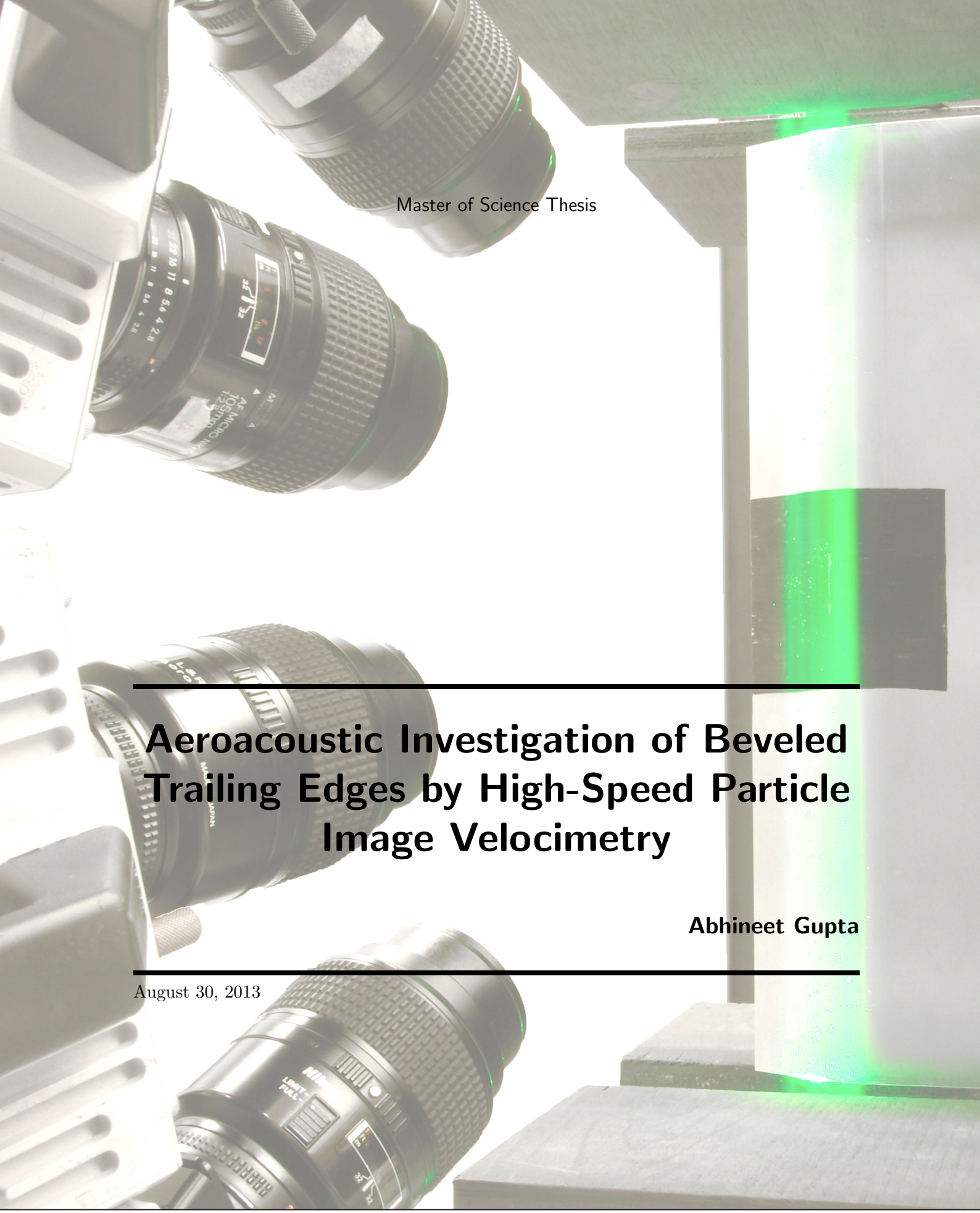

Master of Science Thesis

Aeroacoustic Investigation of Beveled Trailing Edges by High-Speed Particle Image Velocimetry

Abhineet Gupta

August 30, 2013

Aerodynamics

Faculty of Aerospace Engineering

TU Delft

Delft University of Technology

Aeroacoustic Investigation of Beveled Trailing Edges by High-Speed Particle Image Velocimetry

Master of Science Thesis

For obtaining the degree of Master of Science in Aerospace Engineering
at Delft University of Technology

Abhineet Gupta

August 30, 2013

Faculty of Aerospace Engineering · Delft University of Technology

Delft University of Technology

DELFT UNIVERSITY OF TECHNOLOGY
DEPARTMENT OF AERODYNAMICS

The undersigned hereby certify that they have read and recommend to the Faculty of Aerospace Engineering for acceptance the thesis entitled **"Aeroacoustic Investigation of Beveled Trailing Edges by High-Speed Particle Image Velocimetry"** by **Abhineet Gupta** in fulfillment of the requirements for the degree of **Master of Science**.

Dated: August 30, 2013

Supervisors:

Prof. Dr. F. Scarano

Dr. D. Ragni

Dr. M. Kotsonis

Stefan Pröbsting, MSc

Acknowledgements

I am dedicating this thesis to my family, especially my lovely parents: Yogesh Gupta and Anju Gupta for their unconditional love and support. It is only because of you that I have reached this mark in my life and I really can not express my feelings of love and gratitude towards you in words.

I am thankful to Prof. Fulvio Scarano for his supervision and giving me the opportunity to work on this project. Many words of gratitude to Stefan Pröbsting for the friendly guidance and the long discussions we had during and after the experimental campaign. He is truly a great mentor, an excellent researcher and yet a humble human being. It was an honour for me to be able to work under his guidance.

I would also like to thank all the people at the aerodynamics department and my colleagues for their constant support and motivation. Last but not the least, I am specially thankful to all my friends in Delft for making the past two year so memorable and wonderful.

Summary

The aerodynamic noise generated by trailing edge of aircraft wings at take-off and approach configuration continues to be a critical factor in the future development of aviation. Trailing edge noise is also a serious concern for wind turbines, marine propellers, helicopter rotors, axial and centrifugal turbines and compressors. A fundamental understanding of how the energy contained in turbulent motions around trailing edges is converted to sound will be beneficial for designing silent airfoils and control surfaces. Current research aims at applying new tools of flow field interrogation i.e. high-speed planar and tomographic PIV to the canonical problem of trailing edge noise.

In analytical models, the far field noise can be described using turbulent quantities like the spanwise coherence. The use of high-speed tomographic PIV creates a link between the phenomenological description of the flow and acoustic field in terms of coherence of structures and noise. The geometric configuration used involves an airfoil with an elliptic leading edge and an asymmetric beveled trailing edge with 25 deg tip angle (θ) and three different radii of curvature (R). The measurements are taken at four different Reynolds numbers.

The typical flow structure for the class of geometry under consideration involves separation, a recirculation region and a wake. The boundary layer on the suction side separates upstream of the trailing edge, while the boundary layer on the pressure side separates at the sharp edge. The separation point at the suction side moves downstream with increasing Reynolds number and radius of curvature. Instantaneous flow visualization suggests a dominant frequency representing oscillatory vortical motions in the upper shear layer. Spatial distribution of source terms in Ffowcs-Williams and Hall's acoustic analogy are estimated. Tomographic PIV results are compared to planar PIV and a good agreement is observed. For the visualization of vortical structures in the flow, the Q-criterion is used and applied to the 4D velocity data. Large coherent structures appearing with high level of spanwise vorticity are identified. Most of these structures show a relatively large spanwise coherence and are associated with the Kelvin Helmholtz instability. Spatial correlation and coherence in spanwise direction is analysed along the core of the shear layer on the suction side and the corresponding length scales are evaluated. It is concluded that the acoustic emissions largely depends on flow structure and the flow structure in turn depends on the geometrical parameters (θ, R) and the flow parameters (Re). Hence, an experimental determination of the flow structure allows predicting and assessing the noise reduction potential.

Table of Contents

List of Figures

List of Tables

Nomenclature

0.1 Symbols

Symbol	Unit	Definition
U_∞	m/s	Freestream velocity
U_o	m/s	Velocity magnitude
U	m/s	Mean streamwise velocity
u	m/s	Fluctuating streamwise velocity
δ	mm	Boundary layer thickness based on $0.95U_\infty$
c	mm	Chord length
t	mm	Airfoil thickness
$\bar{\theta}$	deg	Beveled trailing edge angle
R	mm	Beveled edge radius of curvature
f	Hz	Frequency
f_s	Hz	Sampling frequency
λ_a	mm	Acoustic Wavelength
M	–	Mach Number
St	–	Strouhal number
Re_c	–	Reynolds number based on chord length

0.2 Abbreviations

PIV	Particle Image Velocimetry
BTE	Beveled Trailing Edge
TR	Time-Resolved
HS	High-Speed
2C	Two Component
KH	Kelvin Helmholtz

Chapter 1

Introduction

The world is witnessing an increasing demand for transportation of goods and for travelling to far and remote places. Until now, air transport has been successfully addressing this issue. This has also lead to a tremendous increase in the number of flights being operated annually. Along with this trend comes the need for expansion of global transportation hubs, large airports located in the vicinity of or even close to the center of large metropolitan areas, which have to increase their capacity in terms of take-off and landings.

The aerodynamic noise of airplanes at take-off and in the approach configuration continues to be a critical factor in the future development of aviation. An aircraft reach a peak of noise emittance during these two phases of flight where high-lift devices are used and the landing gear is deployed as shown in Figure 1.1. Furthermore, the aircraft's trajectory passes unavoidably through the vicinity of urban areas at moderate height. Additionally, the exposure to noise audible in the cabin of an airliner during cruise flight is a well-known nuisance to every passenger.

In order to tackle the challenge of noise reduction, it is important to identify the noise sources present on an aircraft. The prominent sources of airframe noise on the present aircraft configuration has been shown in Figure 1.2. In addition to noise from the jet engine, airframe noise (noise from the landing gear, slats, and flaps etc) has also become a significant component of overall noise, especially during landing and take-off.

Aviation is not the only industry that is affected by trailing edge noise. Several other branches of engineering suffer from noise emitted by trailing edge including wind energy, marine vehicles, turbomachinery components, cooling fans, and propellers. Sound emissions from wind turbine have been one of the most studied environmental impact areas in wind energy engineering. In the past, different devices and modifications of trailing-edges have been investigated with the aim to reduce noise emissions. A fundamental understanding of how the energy contained in turbulent motions is converted to sound is important to the design of quiet trailing edges.

Figure 1.1: Aircraft approaching an airport with flaps deployed

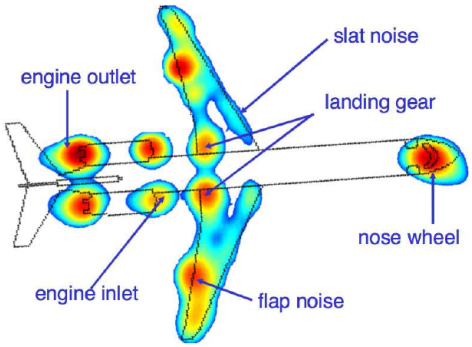

Figure 1.2: Sources of airframe noise. Source: Oerlemans (2009)

The objective of the present research is to experimentally measure flow field and then obtain the acoustic variables in order to develop an understanding of the mechanisms that generate trailing edge noise in incompressible, high Reynolds number flows. This includes the measurement of the time resolved local velocity field using the Tomographic Particle Image Velocimetry and the estimation of sound sources using Aeroacoustic Theory.

1.1 Research Objective

Aeroacoustics is a branch of acoustics that studies noise generation via either turbulent fluid motion or aerodynamic forces interacting with surfaces. The mechanisms of sound generation by fluid motion have been studied intensively since the celebrated work of Lighthill (1952). Microphones are the conventional tools for acoustic measurements. However, the use of a single microphone only provides information about the spectral composition of the sound field. The conventional approach relies on beamforming algorithms and the simultaneous use of arrays of microphones which allow for both the quantification and the spatial localization of the acoustic sources (Lorenzoni, 2008).

An alternative approach to aeroacoustic problems is the use of analytical solutions to predict trailing edge noise from the knowledge of the characteristics of the flow (Amiet (1976), Ffowcs Williams and Hall (1970), Howe (1999)). The most difficult challenge in this regard is modeling the turbulence in the flow. Although this methodology is apparently less immediate than the direct measurement of the radiated acoustic field, it provides a deeper insight into the physical processes responsible for the sound generation. This makes the characterization of the sources of noise, one of the crucial issues in aeroacoustic feasible. The unsteady nature of acoustic propagation requires the knowledge of the time evolution of the aeroacoustic noise sources. This is usually achieved by implementation of high resolution CFD techniques. Large eddy simulation (LES) is becoming increasingly popular for modelling airfoil trailing edge turbulent flow and noise Wang and Moin (2000) and Wang (2005). While this technique

is able to provide accurate descriptions of the turbulent field, computational costs are still high and for many engineering design situations where multiple iterations and calculations are needed, it is prohibitive (Lorenzoni (2008)).

The innovative aspect of the present analysis is the prediction of noise by use of high-speed PIV for the characterization of the unsteady velocity field. PIV based aeroacoustic predictions have been carried out by some authors in the past (work done by Koschatzky et al. (2010) on rectangular cavity).

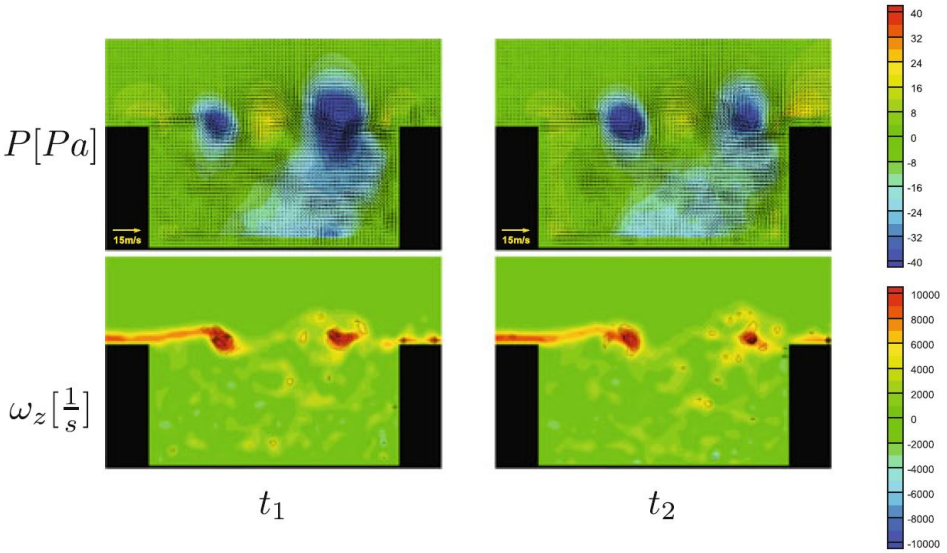

Figure 1.3: Instantaneous pressure and out of plane vorticity. Source: Koschatzky et al. (2010)

To the knowledge of the author, tomographic PIV technique for aeroacoustic prediction on a beveled trailing edge airfoil configuration have not previously been employed. The scope of the present work , within the technical limits of this specific experiment, is to make a qualitative and quantitative description of the fluid dynamics and potential aeroacoustic sources. The research objectives of the current work can be listed as:

- Study of flow field around an airfoil using high-speed planar PIV, effect of trailing edge curvatures and Reynolds number on the flow field.
- Study the effect of flow field on acoustic activity based on planar PIV.
- Study of 4D flow structure using high-speed tomographic PIV.
- Estimation of source activity based on spanwise correlation and coherence of velocity fluctuations using high-speed tomographic PIV .

1.2 Thesis Outline

The first chapter provides a general introduction and motivation for research on trailing edge acoustics. Chapter 2 gives an overview of the current literature that was relevant in understanding the physics observed. In addition, results and conclusions from other works regarding trailing noise edges are presented. Chapter 3 includes a general description of the measurement techniques selected and a thorough description of the facilities and the experimental arrangement and configuration. Chapter 4 presents the results obtained from the planar PIV measurements. Each result is discussed with respect to the literature and the current understanding of the matter. The results of the implementation of the aeroacoustic analogies are presented and a comparison with the work of Wang and Moin (2000) has been discussed. Chapter 5 discusses the results of high-speed tomographic PIV with the focus on flow visualization and estimation of spanwise correlation and coherence. Finally in Chapter 7, the general conclusions of the investigation with recommendations for further investigations are drawn.

Chapter 2

Beveled Trailing Edges

The phenomenon of flow induced noise radiation for trailing edges has been a matter of numerous investigations in the past. The geometric configuration used by most of the previous researchers (Blake, 1975, 1984; Shannon and Morris, 2006; Wang and Moin, 2000; Wang, 2005) involves a flat strut with an elliptic leading edge and an asymmetric beveled trailing edge with varying tip angle. While the geometric configuration is rather simple, many experimental and numerical observations have shown a flow phenomenon rich in unsteady fluid dynamics. This complex flow is often accompanied by an intense acoustic radiation that produces both discrete and broadband noise. The emphasis of earlier experimental investigations (Blake, 1975) was mainly on the trailing edge vortex shedding. In this chapter, an attempt has been made by the author to describe the physics of the flow around beveled trailing edges and the acoustic emission by beveled trailing edges based on previous theoretical, numerical and experimental work.

This chapter starts with an overview of relevant aeroacoustic theories. This is followed by some of the flow properties of beveled trailing edges. This is followed by a discussion where we outline some of the analytical relationships between the flow over a trailing edge and the far field sound this process generates.

2.1 Aeroacoustics

The landmark paper by Sir Michael James Lighthil in 1952 showed that sound is generated whenever the fluid motion is unsteady. In the low Mach number regime, unsteady flow in a free space is a relatively inefficient noise source of quadrupole nature as discussed in Lighthill (1952). The presence of a solid object like an airfoil increase the generated sound by vortex shedding, unsteady separation and imposing boundary inhomogeneity which promotes efficient conversion of flow energy to acoustic energy (Wang, 2005). The problem of trailing edge noise at low Mach numbers was first examined by Powell (1960). Similarity arguments

were advanced to estimate the strength of postulated aerodynamic dipole sources located on the plate near the trailing edge. It was deduced from this model that the edge noise sound power varies approximately as $U_c^{4.6}$, U_c being the characteristic flow velocity, and that the power spectral density decays inversely as the cube of the frequency at high frequencies. Powell's treatment was not sufficiently detailed to predict the field shape of the radiation. The subsequent theoretical discussions of edge noise have been principally in terms of a prototype configuration in which the wing and trailing edge are modelled by a semi-infinite rigid plate, and the validity of the conclusions is consequently limited to cases in which the the chord of the airfoil is acoustically non compact while the thickness is acoustically compact. In general, a body is said to be acoustically compact when its characteristic dimension is small compared to the wavelengths of the sound waves it is producing or with which it interacts (Howe, 2003).

Crighton and Leppington (1971) and Howe (2000) demonstrates analytically that in the acoustically thin foil limit, the specific trailing-edge shape does not affect the fundamental scattering properties such as the directivity and the velocity scaling of the predicted noise spectra. When the acoustic wavelength is much longer than the thickness of the strut but much shorter than the chord ($t \ll \lambda_a \ll C$), which covers an important range of frequencies, an airfoil can be reasonably approximated by a semi infinite plane with zero thickness.

The various published theories differ mainly in the way in which the fluctuating flow is assumed to interact with the edge of the plate to produce sound, and fall roughly into the following three categories (Howe, 1978):

1. Theories based on the Lighthill's acoustic analogy: for example those developed by Ffowcs Williams and Hall (1970) and Crighton and Leppington (1971)

2. Theories based on the solution of special problems approximated by the linearized hydroacoustic equations: for example Amiet's Diffraction Theory (Amiet, 1976)

3. Ad hoc models: these involve postulated source distributions whose strengths and mulitpole types are generally determined empirically, and have been proposed by Hayden et al. (1976) and Tam and Reddy (1996).

Howe (1978) showed that when suitably viewed, all relevant theoretical models lead to the same U scaling law for the velocity dependence of the radiated sound, exhibit the same static directional characteristics and the same dependencies on the length scales of the turbulent edge flow. None of the theories gives an overall picture of the edge noise mechanism, however, in that those listed in category (i) determine the radiation in terms of an assumed turbulent velocity field, while those in categories (ii) and (iii) are confined to particular flow models or relate the sound field to pressure fluctuations on or near the edge of the plate.

In general, the fluctuating velocities, unsteady surface pressure, and far field pressure produced by the flow over a trailing edge can be related to one another (Shannon, 2007). Figure 2.1 shows a sketch of these relationships. The generation of sound is directly related to the local turbulent velocity field through Lighthill's equation. The hydrodynamic surface pressures generated by these turbulent motions can be related through Poisson's equation. Similarly,

the unsteady surface pressures can be directly related to the far field sound through Curle's equation (Curle, 1955).

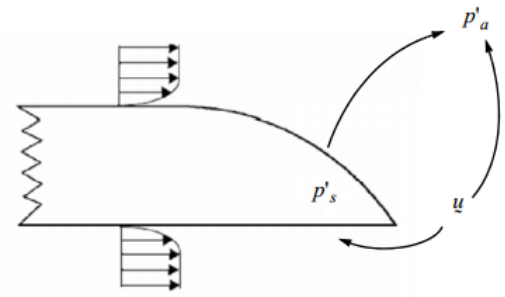

Figure 2.1: Illustration of relationships between unsteady surface pressure, turbulence and far field acoustics in trailing edge flows. Source: Shannon (2007)

The focal point of discussion here is the first category of aeroacoustic theories based on Lighthill's acoustic analogy. Lighthill (1952) rearranged the Navier-Stokes equation of a compressible viscous fluid into an inhomogeneous wave equation hence making a connection between fluid mechanics and acoustics. The Lightill equation is written as

$$\frac{\partial^2 \rho}{\partial t^2} - c_o^2 \nabla^2 \rho = \frac{\partial^2 T_{ij}}{\partial y_i \partial y_j} \tag{2.1}$$

where $\tau_{ij} = \rho u_i u_j + (p - c_o^2 \rho)\delta_{ij} + \tau'_{ij}$ is the Lighthill stress tensor, c_o is the speed of sound in the fluid, $u_i u_j$ is the Reynolds stress tensor, τ'_{ij} is the viscous part of the Stokes stress tensor. The equation 2.1 is an inhomogeneous wave equation with a source term on the right hand side. It is important to realize that Lighthill's equation is exact in the sense that no approximations have been made in its derivation from Navier-Stokes equation. The equation is often called "Lighthill Analogy" because it represents an acoustic model not based on flow generated noise but rather on the analogy of how the flow generated noise might be represented through the governing equations of a compressible fluid. If the Reynolds stress is the largest component of the Lighthill stress tensor, the equation simplifies to

$$\frac{\partial^2 \rho}{\partial t^2} - c_o^2 \nabla^2 \rho = \frac{\partial^2 (\rho u_i u_j)}{\partial y_i \partial y_j} \tag{2.2}$$

The above equation is often used to represent acoustic behaviour of open flows such as jets. The right-hand side is an acoustic source which is non-zero near the jet. The fluid is assumed to be at rest outside the jet and satisfies the homogeneous wave equation for acoustic pressure or density. For the flow with a surface present, Curle (1955) provided a derivation to account for the effect of surface pressure. A useful result is (Morris, 2011)

$$\nabla^2 \rho - \frac{1}{c_o^2} \frac{\partial^2 \rho}{\partial t^2} = -\frac{\partial q}{\partial t} + \frac{\partial F_i}{\partial y_i} - \frac{\partial^2 T_{ij}}{\partial y_i \partial y_j} \tag{2.3}$$

where q is the rate of mass injection per unit volume, and F_i is the i^{th} component of the force vector per unit volume. The three terms on the RHS of the above equation appear as

monopole, dipole and quadrapole sources respectively. For the flow over an airfoil, the net unsteady force created on the object by the unsteady pressure field can be considered as an acoustic source. For the low mach number regime, the contribution of the stress tensor term to the net radiated sound will be small compared to the unsteady forces (Morris, 2011).

Ffowcs Williams and Hall (1970) derived a solution using the equation 2.2 for a rigid, vanishingly thin half plane immersed in an otherwise unbounded fluid. The presence of a rigid half plane gives the boundary condition that the velocity vanishes at the surface. The Fourier transform of the Equation 2.2 was taken to obtain an inhomogeneous Helmholtz equation and than the boundary condition was applied. The solution of equation 2.2 with this boundary condition can be written down at once in terms of a Green's function, G, whose normal derivative vanishes on the half-plane. The analysis was restricted to field points which are many wavelengths away both from the turbulent region and from the edge of the half plane, i.e. $kr \gg 1$ and $r \gg r_o$ where k is the acoustic wave number. The nomenclature has been described in figure 2.2 where r_o represents the position of turbulent region in radial coordinates, r represents the far field region and k is the acoustic wavelength.

Two cases were considered separately, the first case assumes the turbulence to be well within a typical acoustic wavelength of the edge ($2kr_o \ll 1$). Under these conditions, Ffowcs-Williams and Hall showed that the far field pressure perturbation in the frequency domain can be written in the form of equation 2.4.

$$\begin{aligned} \widehat{p}(\mathbf{x},\omega) &= \frac{2e^{-i(\pi/4)}}{\pi^{0.5}} k^2 sin(\frac{\theta}{2}) \int_V \frac{e^{ikR}(sin\phi)^{0.5}}{4\pi R(2kr_o)^{\frac{3}{2}}} \\ &\quad \times \left\{ \rho_\infty(\widehat{u_\theta^2} - \widehat{u_r^2}) sin(\frac{\theta_o}{2}) - 2\rho_\infty \widehat{u_r u_\theta} cos(\frac{\theta_o}{2}) \right\} d^3y \end{aligned} \tag{2.4}$$

where the caret denotes temporal Fourier transform, ω is the circular frequency, and $k = \omega/c_\infty$ is the acoustic wave number. The velocity components u_r and u_θ are defined in a cylindrical-polar coordinate system shown in Figure 2.2. Position vectors $\mathbf{x}(r,\theta,z)$ and $\mathbf{y}(r_o,\theta_o,z_o)$ represent far field and source field points, respectively, with $sin\phi = r/[r^2 + (z-z_o)^2]^{\frac{1}{2}}$.

The first point to notice is that the integrand of equation 2.4 contains the large factor $(2kr_o)^{\frac{-3}{2}}$. This has the consequence that the far field acoustic pressure levels when there is an edge in the turbulent region may be considerably greater than when there is none. Such eddies were found to have the sound output of the quadrupoles (Wang and Moin, 2000). The far field sound intensity induced by these sources depends upon the fifth power of a typical fluid velocity. The second condition assumes the turbulence to be many wavelengths away from the edge, i.e. the effect of the half plane on the noise from those eddies which are far enough from the edge for the inequality $(kr_o)^{\frac{1}{2}} \gg 1$ to hold is considered, r_o is again the distance of the centre of the eddy from the edge. It was found that the far field sound has the same features as would be predicted by geometrical acoustics.

Powell(1960) and Howe(1998) provided another simplified model for the acoustic behaviour of fluid flow in which the unsteady distribution of vorticity was considered as the sound source.

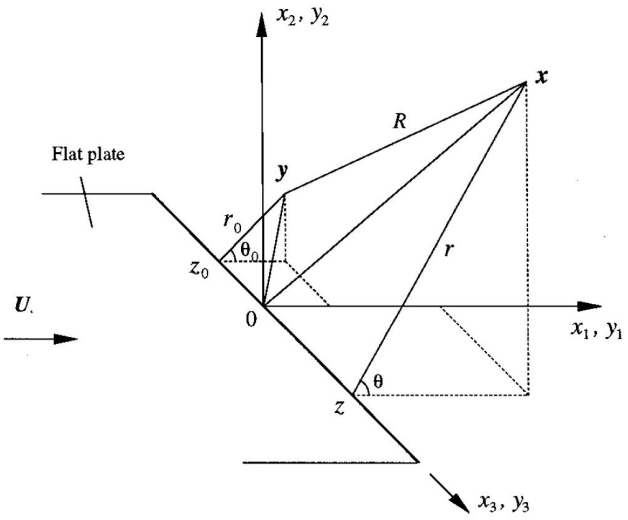

Figure 2.2: Coordinate system for calculating the radiated noise of flow past the trailing edge of a semi-infinite thin plate. Source:Wang and Moin (2000)

Several authors (Amiet, 1976; Howe, 1999) have discussed diffraction theory in the framework of trailing edge noise, relating the power spectral density and the spanwise coherence length of hydrodynamic pressure fluctuations to an estimation of the acoustic far field spectrum.

2.2 Flow Structure around Beveled Trailing Edges

From an experimental perspective, the approach to the prediction of trailing edge noise has typically been based on the measurement of surface pressure fluctuations. Amiet (1976) developed a more complete theoretical model for calculating the noise radiated from an airfoil trailing edge using spectral characteristics of the wall pressure. To complement trailing edge noise theory, the majority of experimental studies on trailing edge noise have involved measuring airfoil surface pressure fluctuations and far-field noise spectra at high Reynolds numbers. Blake (1975, 1984) and Tam and Reddy (1996) analyzed the trailing edge noise mechanism by measuring fluctuating surface pressure at high Reynolds numbers. Brooks and Hodgson (1981) measured the radiated trailing edge noise and wall pressure fluctuations for a NACA0012 airfoil with varying trailing edge bluntness at high Reynolds numbers. Good agreement was found between the measured noise spectra and that predicted using measured surface pressure fluctuations and the theory developed by Howe.

The prediction of trailing edge noise utilizing hot-wire anemometry has been attempted several times. Thompson and Whitelaw (1985) used flying-hot-wire anemometry to determine the velocity characteristics of a flow designed to simulate the trailing-edge region of an airfoil at high angle of attack. Devenport et al. (2001) measured two-point correlations functions in the near wake of a trailing edge using hot-wire anemometry and related these functions to the sound produced by the edge. Although these data provide valuable information regarding the

spatial and temporal scales of a flow, they do not facilitate a detailed understanding of the mechanisms of sound production. Moreover, hot-wires are not well suited for blunt trailing edge flows where the near wake flow is separated and recirculating (Shannon and Morris, 2006).

In general, the typical flow structure for the class of geometry under consideration involves separation points, a recirculation region and a wake. The boundary layer from upper surface may or may not separates prior to the trailing edge on the curved surface. The lower boundary layer separates at the sharp edge. The flow features have been demonstrated in Figure 2.3. Figure 2.4 outlines the characteristic features of the flow as observed by Shannon and Morris (2006).

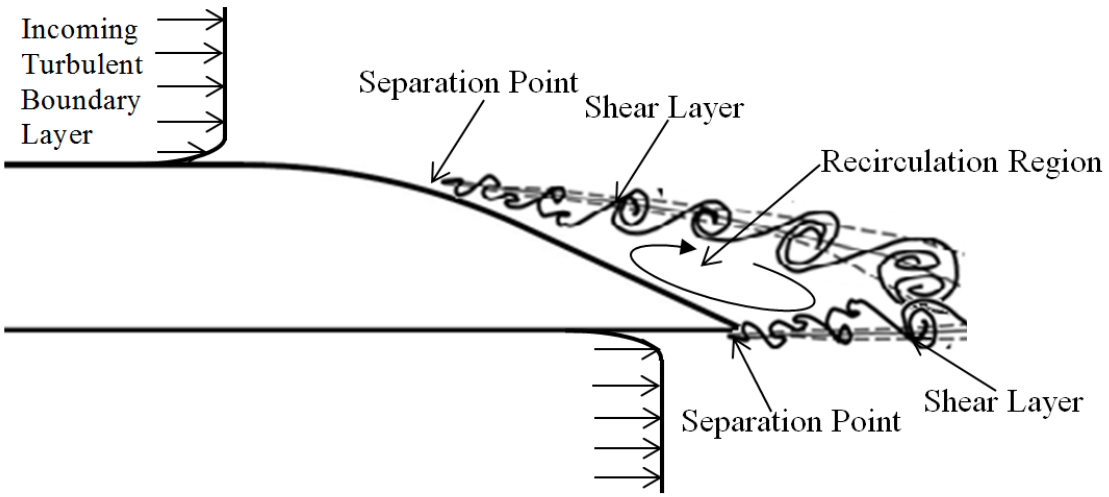

Figure 2.3: Characteristic flow features around beveled trailing edges

The resulting flow field exhibits a number of phenomena that makes it an interesting candidate for trailing edge noise research. The flow is particularly interesting due to the fact that the asymmetric edge shape generally produces a separated flow on the low pressure side and an attached boundary layer on the high-pressure side, thus creating complex shear layer interactions in the vicinity of the trailing edge. Blake (1975) did a comprehensive study on different trailing edge geometries attached to a flat plate with a circular leading edge. Later in 1984, the same author published another report for the same geometrical configuration with emphasis on aerodynamic sound and related properties (Blake, 1984). Trailing edge vortex shedding and, in particular, a tonal phenomenon called singing was observed for some airfoils. Consequently, the trailing edge geometries were classified into two categories, namely the "singing" and "non-singing" airfoils as shown in figure 2.5. The first category of airfoils exhibits large scale vortex shedding linked to tonal noise. The asymmetrical beveled trailing edge with a tip angle of atleast 30 deg at least were likely to produce tonal excitations. However, a continuous spectrum was observed when the edge is sharpened or asymmetrically beveled to include angles 30 deg or less.

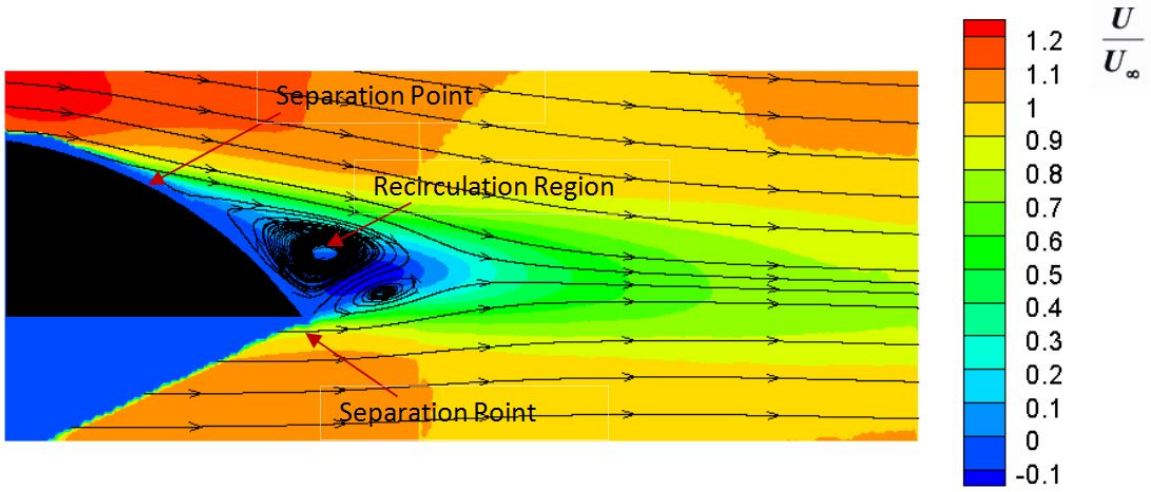

Figure 2.4: Time averaged streamwise velocity contours with streamlines. Source: Shannon and Morris (2006)

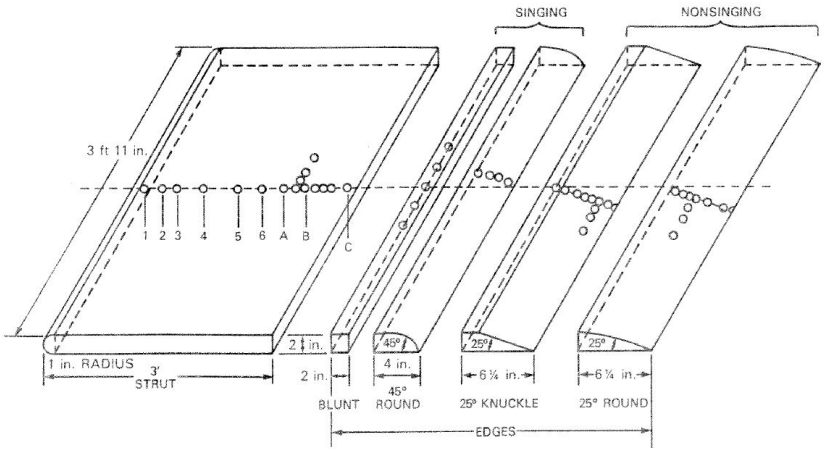

Figure 2.5: Trailing edges classification by Blake (1984)

Blake (1984) observed that when the vortex growth does not occur(non-singing airfoils), the surface pressure fluctuations are distributed over a broad frequency range centred on a characteristic frequency that scale on the same variable as the tonal pressure as shown in Figure 2.6. The 25 deg knuckle edge, which was not rounded, has boundary layer separation over the wedge region with an extensive zone of large scale motion. The 25 deg rounded edge has a more gradually induced separation that permits extensive region of boundary layer flow with adverse pressure gradient. For the 25 deg knuckle edge, the boundary layer first experiences a favourable pressure gradient followed by an adverse pressure gradient as shown in figure 2.7. The pressure recovery appeared to be more apparent at higher speeds since the pressure coefficients are less negative at higher speeds. Blake (1984) determined the separation using oil streak experiment to be around point E in figure 2.7. The region of separation between point E and the tip was not just a zone of constant flow reversal, rather

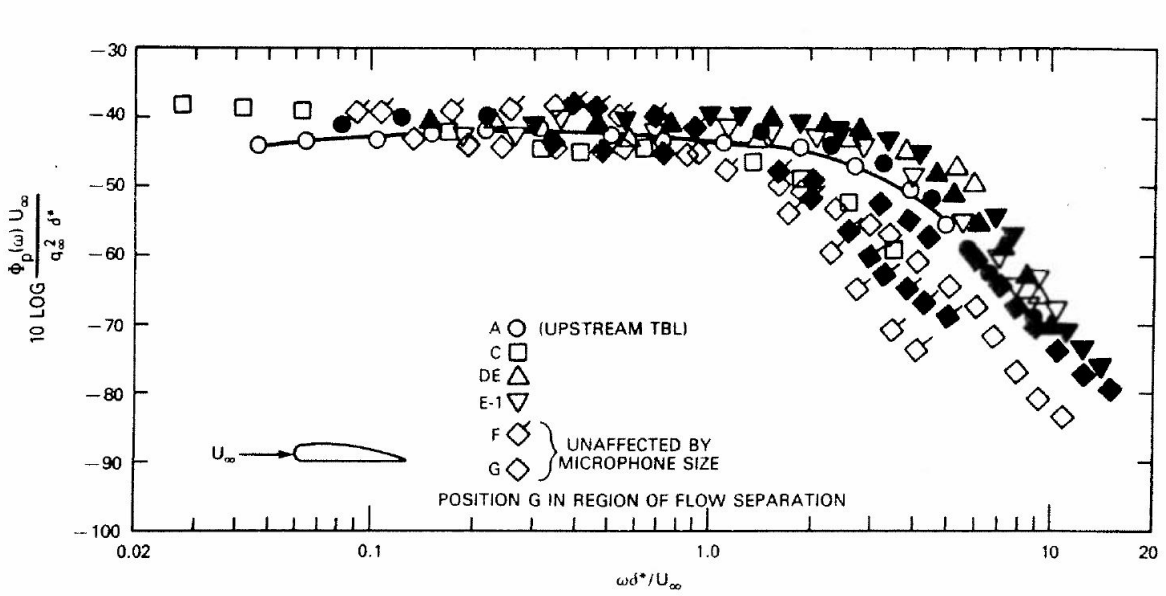

Figure 2.6: Dimensionless pressure spectra for $25\,\mathrm{deg}$ rounded edge (open points represent free stream velocity of 100ft/s while close points represents free stream velocity of 60ft/s. Source:Blake (1984)

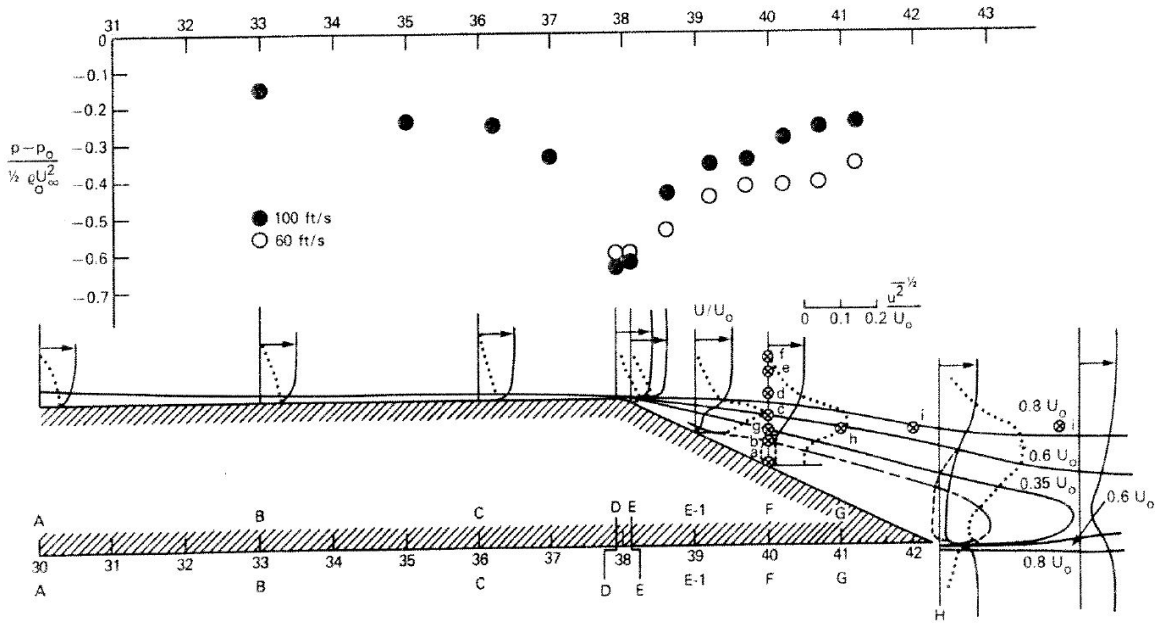

Figure 2.7: Flow pattern and pressure distribution for $25\,\mathrm{deg}$ knuckled trailing edge. Source:Blake (1984)

it was a zone of oscillatory motion with equal tendency of of flow upstream and downstream.

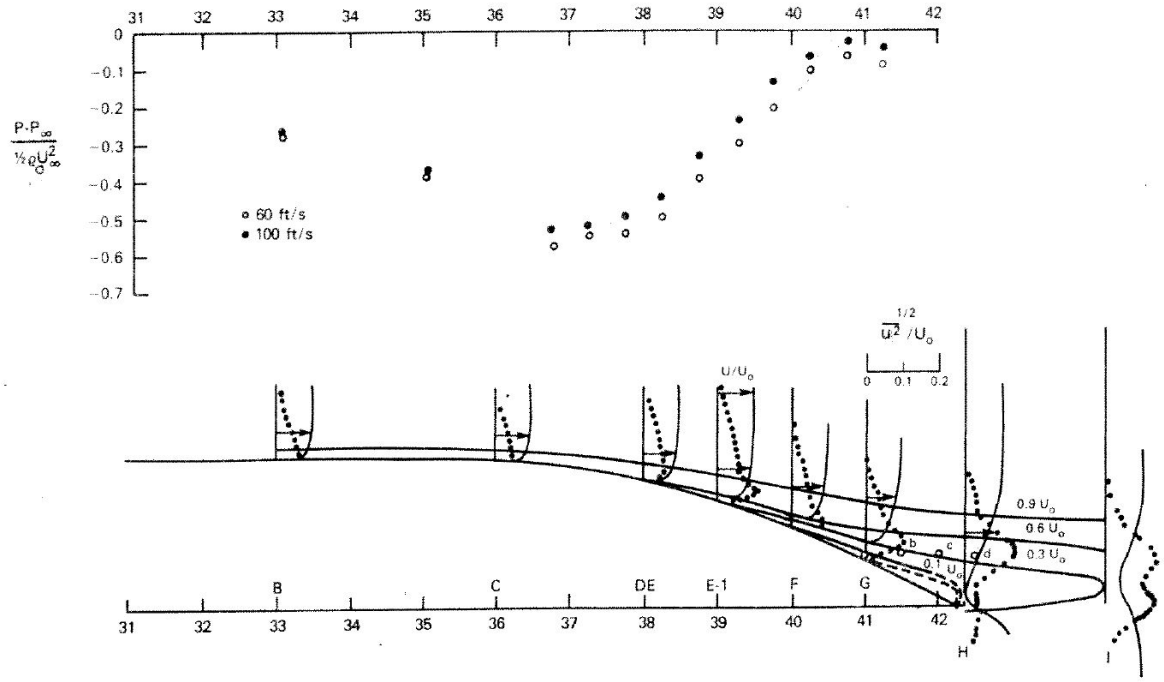

Figure 2.8: Flow pattern and pressure distribution for 25 deg rounded edge. Source:Blake (1984)

For a probe pair separated in the streamwise direction and placed outside the separation zone, a convection velocity of the same order as a local mean velocity was measured. When the probe was situated within the separation zone, there was not time delay between the probes and, therefore, no mean streamwise convection velocity. The locus of $U = 0.6U_o$ gave the locus of turbulence maxima in the shear flow.

For the 25 deg rounded edge, adverse pressure gradient was observed for points downstream of 37 in. (x/t=0.8757) from the leading edge. The mean velocity decreases downstream from this point while the fluctuating velocities increase with an apparent maxima in the vicinity of H and I. The balance of mean momentum measured from the boundary layer on the edge (Blake, 1975) and the oil flow visualization shows that the separation occurs somewhere near F at 100ft/s (30.48 m/s). It was observed that the turbulence dynamics for the separation zone of both the trailing edges seemed qualitatively quite similar; the rounded trailing edge, however, generates a much smaller scale separation zone.

The low momentum fluid contained in the separated region was bound by high momentum fluid on either side, generating two regions of shear in the near wake. The interaction of the separated vorticity in these shear layers resulted in a large scale wake instability. Wang and Moin (2000) performed LES for the 25 deg beveled trailing edge Their numerically simulated fields exhibits realistic turbulence structures and a small separated zone near the trailing edge (2.9). The two shear layers, arising from the separated boundary layer on the upper side and the attached boundary layer on the lower side, interact to produce a turbulent wake in the downstream direction as shown in Figure 2.9. No coherent vortex shedding is observed, in

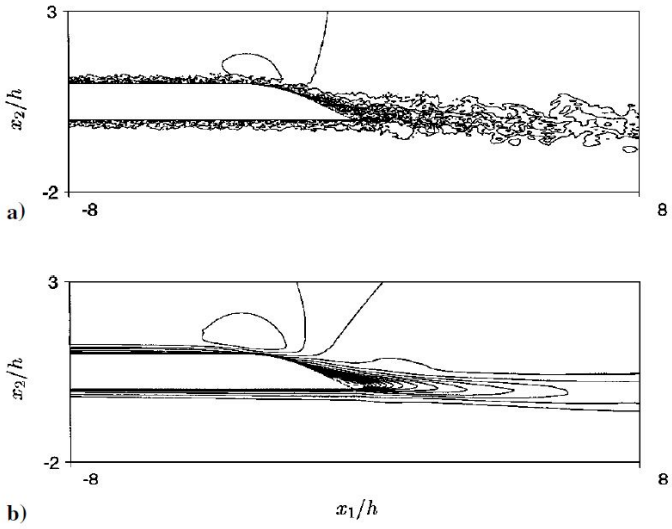

Figure 2.9: Velocity fields computed from LES: a) instantaneous streamwise velocity at a given spanwise cut (contour levels from 0.236 to 1.274, with increment 0.116) and b) mean streamwise velocity(contour levels from 0.081 to 1.207, with increment 0.068).Source:Wang and Moin (2000)

agreement with Blake's experimental data, which show vortex shedding from a 45-deg trailing edge but not the 25-deg one (Blake, 1975, 1984). The velocity profiles at stations mentioned in Figure 2.10 were also compared with the Blake's data as shown by velocity profiles in Figure 2.11. A comparison of the velocity profile obtained by planar PIV experiment as

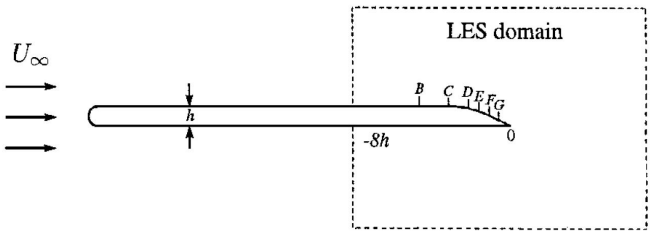

Figure 2.10: Flow configuration and computational domain; measurement stations B to G are located at x_1/h =-4.625, -3.125, -2.125, -1.625, -1.125, 0.625, respectively. Source:Wang and Moin (2000)

a part of this thesis with the data obtained by Blake (1984) and Wang and Moin (2000) at station B has been shown in Figure 2.12. The profiles matches indicating similar incoming boundary layer for all the three analyses.

Wang and Moin (2000) also made an estimate of coherence based on the fluctuating surface pressure in the vicinity of the trailing edge, under the premise that it is representative of the overall coherence of the volume distribution of source terms in Equation 2.4. Figure 2.13 shows the spanwise pressure coherence on the upper surface, one-half grid spacing from the trailing edge. The upper plot shows the is coherence contours as a function of frequency and spanwise separation. The coherence is seen to drop rapidly with spanwise separation, except

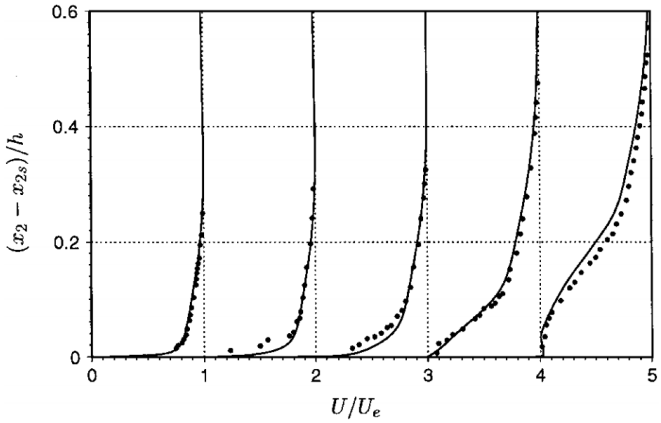

Figure 2.11: Profiles of the normalized mean velocity magnitude. Source:Wang and Moin (2000)

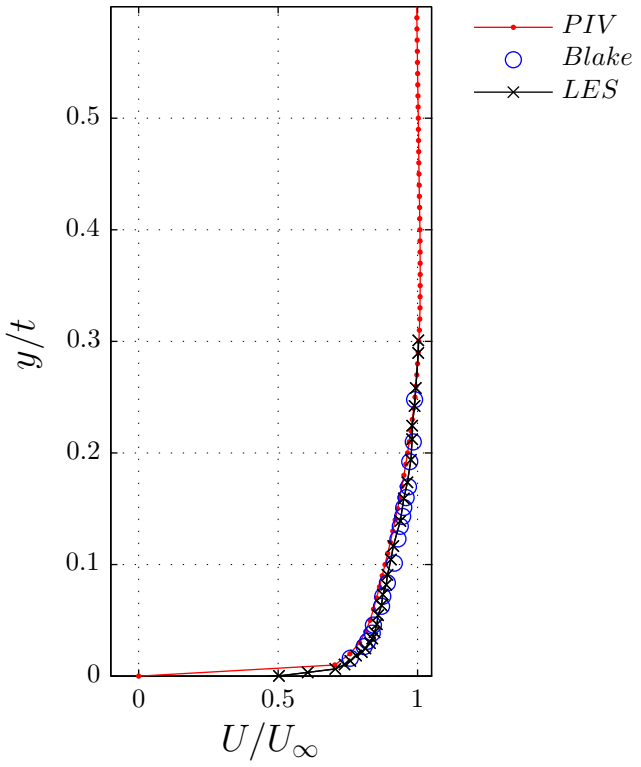

Figure 2.12: Velocity profile for 25 deg rounded bevel trailing edge at x/t=-3.125

at the low-frequency end. The coherence at selected low frequencies is depicted in the lower plot as a function of spanwise separation. It is observed that for $\omega t/U_\infty \geq 5.26$, the coherence exhibits sufficient drop within small spanwise separation.

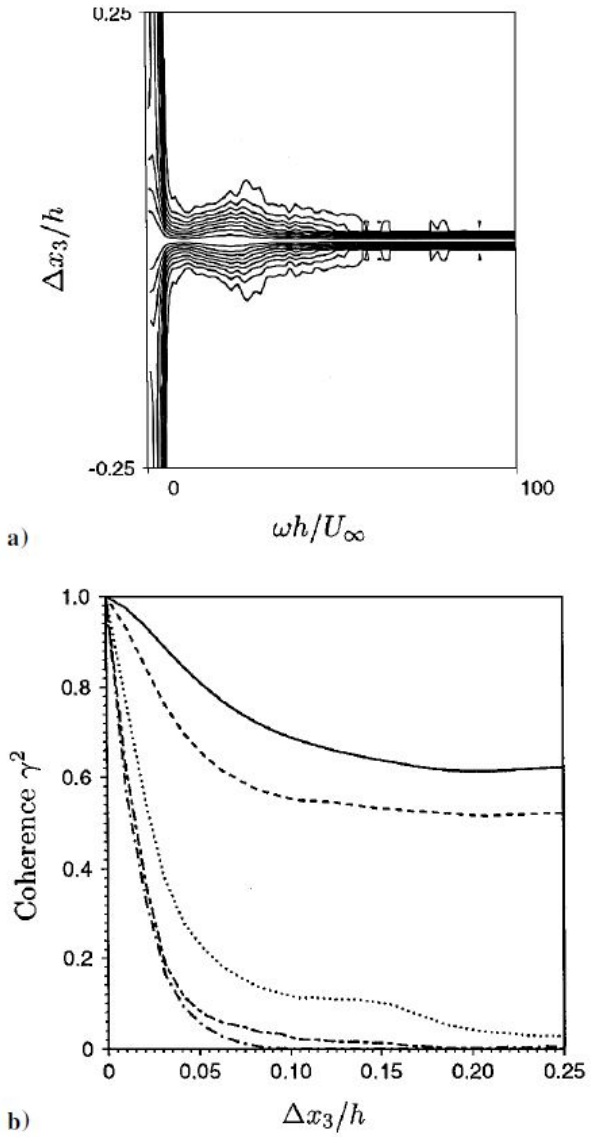

Figure 2.13: Spanwise coherence of the fluctuating surface pressure on the upper surface near the trailing edge: a) contour plot (contour levels from 0:1 to 0:9, with increment 0:10) and b) coherence at frequencies $\omega t/U_\infty$=1:75 , 3:51 , 5:26, 7:01 and 8:76(curves from top to bottom). Source:Wang and Moin (2000)

For the 45 deg beveled trailing edge, Blake (1984) observed that the separation point becomes less distinct and takes place downstream of point 13 (Figure 2.14). Flow characteristics of such a configuration has been shown in Figure 2.14. The figure shows a favorable pressure gradient upstream of point 11, followed by an adverse pressure gradient downstream of this point and constant pressure downstream from point 13. The velocity spectral density have been shown in Figure 2.15 shows existence of a dominating frequency which was interpreted to occur due to a vortex sheet. The investigation by Shannon and Morris (2006) have shown how details of the wake structure determine vortex shedding and how the geometry of the trailing edge influences the interaction of the separated shear layers. If the shear layers are decouples,

vortex formation appears to be disordered. An interesting aspect of the vortex shedding for this trailing edge is that the asymmetry in the model caused a noticeable irregularity in the von Karman vortex street (Shannon and Morris, 2006). The lower boundary layer remained relatively undisturbed before separating suddenly at the sharp edge. The vorticity shed into the wake from the lower edge formed relatively large concentrations of positive circulation which rolled up near the lower, sharp edge of the model and accelerated into the wake at periodic intervals. The spanwise coherence and power spectral density of pressure

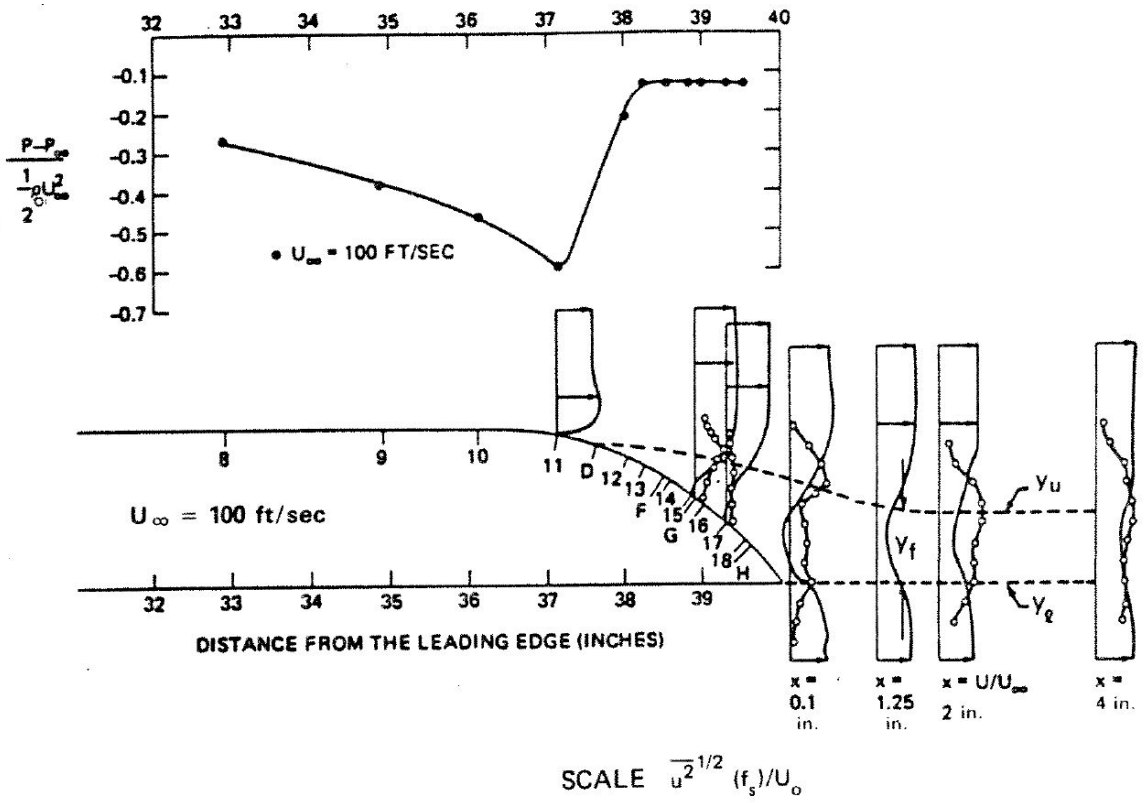

Figure 2.14: Flow Patterns and Pressure Distribution for 45 deg rounded bevel trailing edge.Source: Blake (1984)

fluctuations is of great importance in aeroacoustics. The magnitude and frequency of the radiated sound will be determined by both the intensity and the spatial correlation of the convected turbulence. For example, the amplitude of the tonal noise due to vortex shedding is typically quite large due to the large magnitude of the fluctuations, as well as the relatively long spanwise correlation length scale created by the vortex motions. In contrast, the smaller scale turbulent motions related to the boundary layer flow are both smaller in magnitude, and have a corresponding smaller spatial length scale. This results in a high frequency broadband acoustic signature that is typically more than 10dB less in magnitude than the vortex shedding noise.

Wang (2005) employed large eddy simulations to compute the source field and Lighthill's theory to compute the acoustic far field for an asymmetric 45 deg beveled trailing edge. The

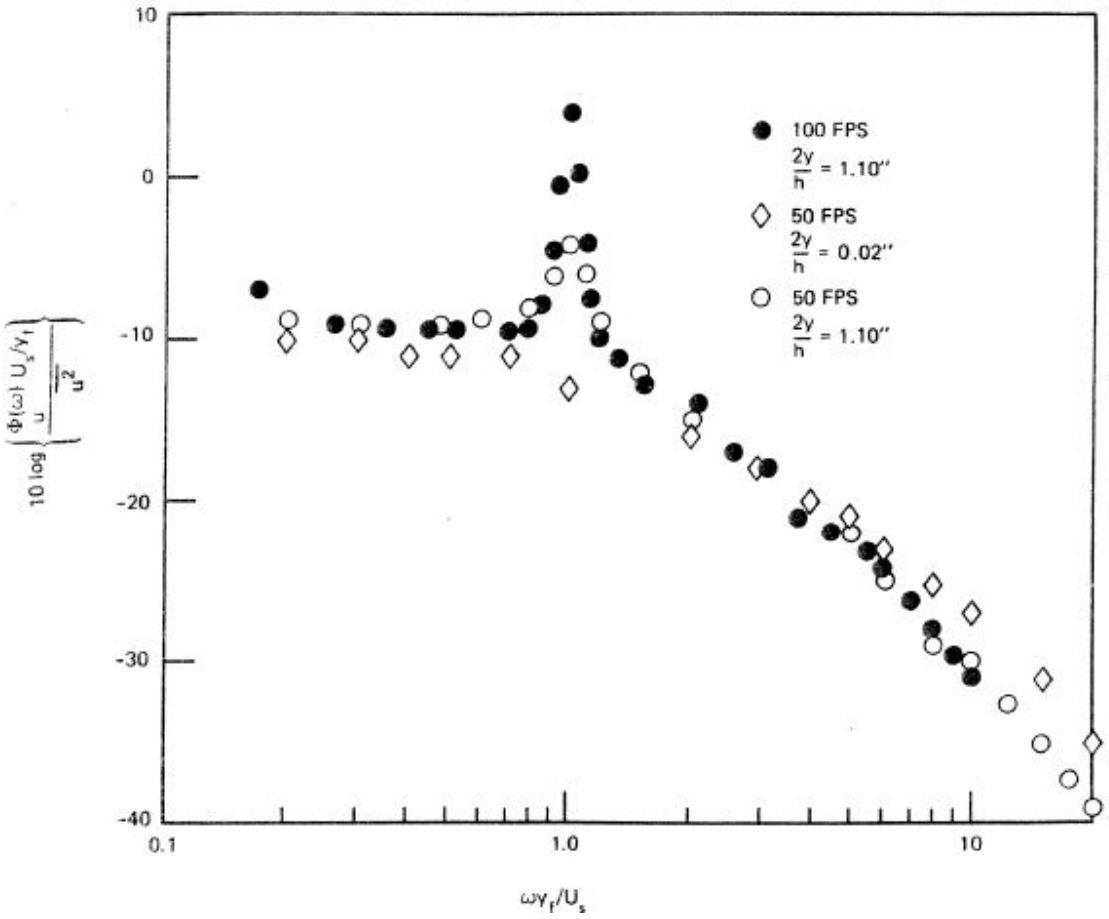

Figure 2.15: Spectral Density for longitudinal velocity fluctuation for 45deg beveled trailing edge angle. Source:Blake (1984)

results were compared and validated against the experimental results obtained by Shannon and Morris (2006).

The comparison of u_{rms} for different spanwise length suggested that the wake is dominated by two dimensional vortices. The simulation showed the existence of large coherent structures in the wake as a result of vortex shedding and realistic small scale turbulence. The shedding frequency was determined using the energy spectra of the streamwise and normal velocity components. The Strouhal number of vortex shedding frequency based on airfoil thickness and mean velocity was 0.44 which was consistent with the experimental values of 0.4. An additional peak at twice the shedding frequency was also observed in the spectra. The U_{rms} contours exhibits two high intensity regions associated with the boundary layers from the upper and lower surface of the airfoil. The fluctuations arising from the lower shear layer are more intense highlighting its role in sound generation.

According to Ffowcs Williams and Hall (1970), velocity fluctuations in the direction normal

to the trailing edge V_{rms} provide predominant acoustic source. Concentration of high level of U_{rms} was observed in a single region near the lower edge of the surface. Despite some remaining issues with velocity boundary conditions, LES predicts the correct overall features of the vortex-shedding trailing-edge flow. A direct comparison was made between the computed and measured sound pressure spectra, and good agreement was achieved in the intermediate frequency range of approximately one decade. A large discrepancy was observed at frequency below 300Hz. Below 300Hz, the measurement plane is within one acoustic length from the trailing edge and the spacing between the microphone arrays is also smaller than the wavelength. Consequently, the measured spectrum may contain large near field effects. There are also some issues with the numerical solution at low frequency range as the approximations about the acoustic far field and half-plane Green's function are formally invalid. The assumption that the aeroacoustic sources outside the computational domain in spanwise direction are statistically independent is also invalid.

The sources of trailing edge noise production for a flat plate airfoil were investigated by Kunze (2004). They investigated geometry in the study was a flat airfoil with an asymmetric 45 deg rounded trailing edge. For the leading edge, an elliptical shape was chosen to prevent flow separation near the leading edge. The flow around and inside a defined control volume was investigated using hot-wire probes and pressure measurements. Far field acoustic measurements and correlation measurements between wire probes and the microphones were made to investigate the possible correlation between the flow physics and the far field acoustics. The control volume boundary results show that the incoming flow is of low turbulent intensity and that the wake behind the trailing edge shows an asymmetric development.

2.3 Aeroacoustic Effects of Beveled Trailing Edges

Flow past the trailing edges of a lifting surface can be the source of both tonal and broadband spectrum noise occurring either separately or simultaneously. The relationship between the near field turbulence and the radiated sound for non compact lifting surfaces at low Mach number can be derived from a number of approaches. The boundary layer from the lower surface separates next to the sharp edge resulting in significant broadband sound level. Perhaps the most important theoretical contribution to the field of trailing edge noise was made by M. S. Howe (Howe (1978), Howe (1988), Howe (1999) and Howe (2000)) In his review paper on trailing edge noise in 1978, Howe (1978) reviewed contemporary theories and divided them into three group as discussed in section 2.1. He has shown that, when appropriately interpreted, all relevant theories produce essentially identical TE noise predictions for vanishingly small Mach numbers. Significantly, Howe has reproduced and generalized the primary conclusions of the diverse theories by using a relatively uniform theoretical approach. The solutions for the noise field include the effect of forward flight and require knowledge of either the turbulent velocity field near the edge or the pressure fluctuations near the edge. However, due to an absence of information as to the precise conditions to apply at the edge, dual solutions are given corresponding to the Kutta condition and no-Kutta condition cases.

In the paper Howe (1988), a theoretical investigation of the influence of asymmetric beveling

on the broadband component of the edge noise produced by turbulent boundary layer flow over the trailing edge region was made. The analysis was performed for included angles in the range $0 \leq \bar{\theta} \leq 90\,\text{deg}$. He discussed that an edge of blunted or rounded profile cannot always be used to reduce trailing edge noise because of the tendency of the flow to separate and produce increased turbulence levels. In addition, separation is often accompanied by the quasi-periodic shedding of large spanwise vortices, which are coherent over distances equal to several edge thicknesses, and can induce harmful, large amplitude structural vibrations together with a strong tonal component of the radiated sound.

If the mean flow separation from the suction surface does not occur,it can be shown that the formulae obtained by use of a Green function for an airfoil of compact chord remain valid for turbulence convecting past the edge on the suction side of the airfoil. When separation occurs, turbulent eddies in the suction surface boundary layer which are convected into the trailing edge region from upstream are displaced from the proximity of the edge. It follows that, except when $\omega t/U \ll 1$, their near field pressure fluctuations are exponentially small at the edge. Only the very low frequency, incident boundary layer disturbances can then interact effectively with the trailing edge, and produce sound essentially as for an airfoil of zero thickness. Turbulence fluctuations within the separated region will, of course, produce high frequency sound by interacting with the edge. The modifications of the results when the airfoil has non-compact chord were also estimated. The chief difference is that the overall intensity of the trailing edge noise is proportional to $\rho_o U^3 M^2$ for a non-compact airfoil, as opposed to $\rho_o U^3 M^3$ for the compact airfoil.

The diffraction theory of Howe (1999) for estimating the sound generated by low Mach number flow past the trailing edge of an airfoil of compact, but finite thickness was applied to investigate the noise produced by turbulent flow over an edge whose upper surface (the suction side) is rounded by Howe (2000). The sound is expressed in terms of the upwash velocity fluctuations that the same boundary layer turbulence would generate if the airfoil were absent. The solid curve in Figure 2.16 is a non-dimensional plot of the acoustic pressure spectrum for the particular case $h = \delta$, when the thickness of the turbulent boundary layer over the upper surface is just equal to the airfoil thickness h. At very low frequencies the radiation must be similar to that from the edge of a thin rigid half-plane. Separated flow over a curved trailing edge profile (Figure 2.17) can be modeled by assuming that after separation boundary layer eddies are convected along a path parallel to the undisturbed mean stream, so that their distance of closest approach to the sharp trailing edge is just equal to the airfoil thickness at the separation point. Here the length l represent the extension of the rounded edge region in the streamwise direction, i.e. the length from the start of curvature till the trailing edge. The strength of the unsteady interaction responsible for sound generation then decreases exponentially with increasing frequency, and predicted levels of edge noise are significantly smaller than estimates made by modelling the interaction in terms of a rigid half-plane. This conclusion ignores possible contributions to sound generation from turbulence in the recirculating zone between the separation streamline and the curved section of the upper surface between the separation point and the edge, which are probably significant only at much lower frequencies

When the mean flow remains attached right up to the trailing edge, boundary layer turbulence on the suction side of the airfoil always interacts strongly with the edge (Figure 2.18) . How-

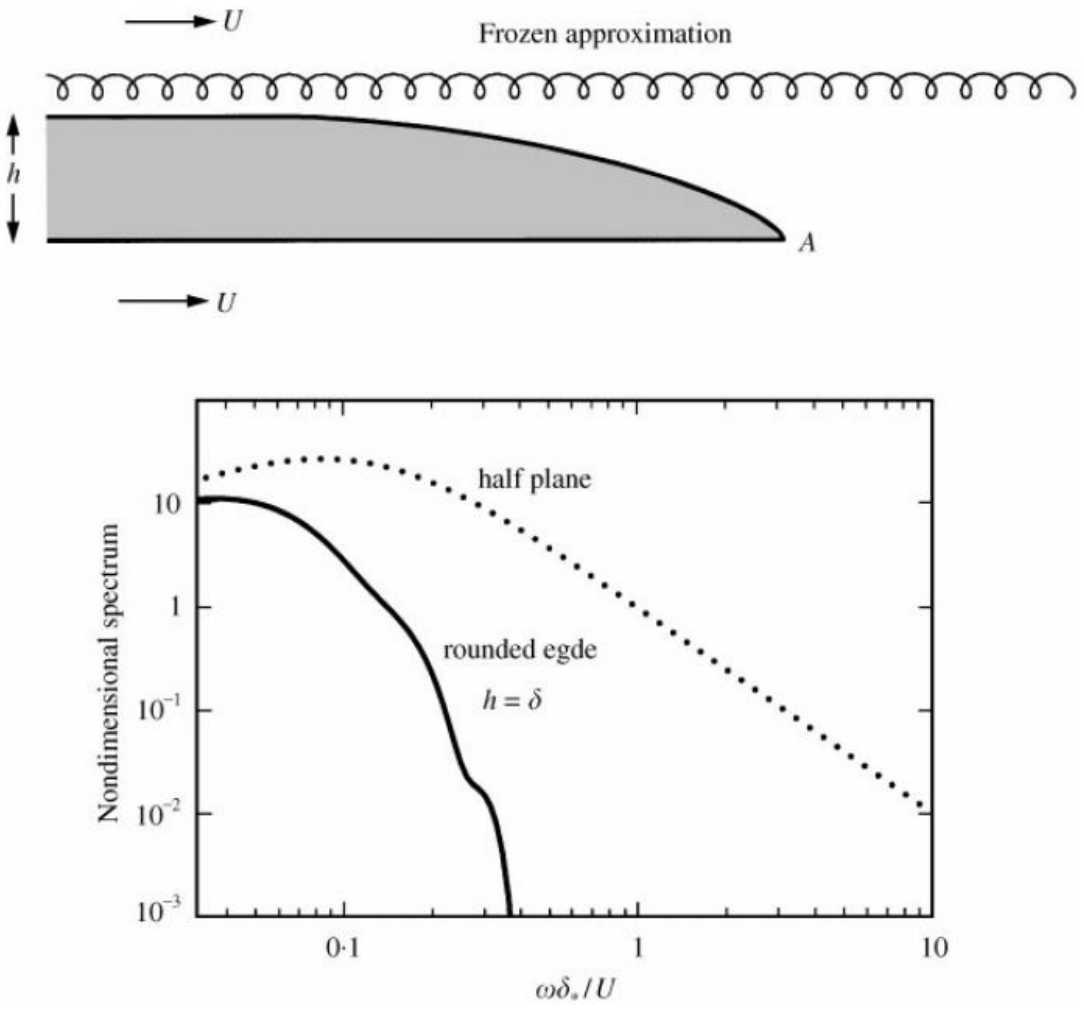

Figure 2.16: Frozen approximation to the edge-noise spectrum for the rounded edge of thickness $h = \delta$ when l=4h, and for the rigid half-plane (h=0) Source:Howe (2000)

ever, because of the finite thickness of the airfoil, the influence of the (turbulence free) lower surface on the radiated intensity continues to decrease exponentially fast at high frequencies. In consequence, most of the high-frequency radiation is associated with the flow interacting with the upper surface. The sound levels are smaller than for the half-plane model, but the differences at higher frequencies are more modest, typically being of the order 5-10 dB, the precise values being dependent on the ratio of the boundary layer thickness to the mean airfoil thickness.

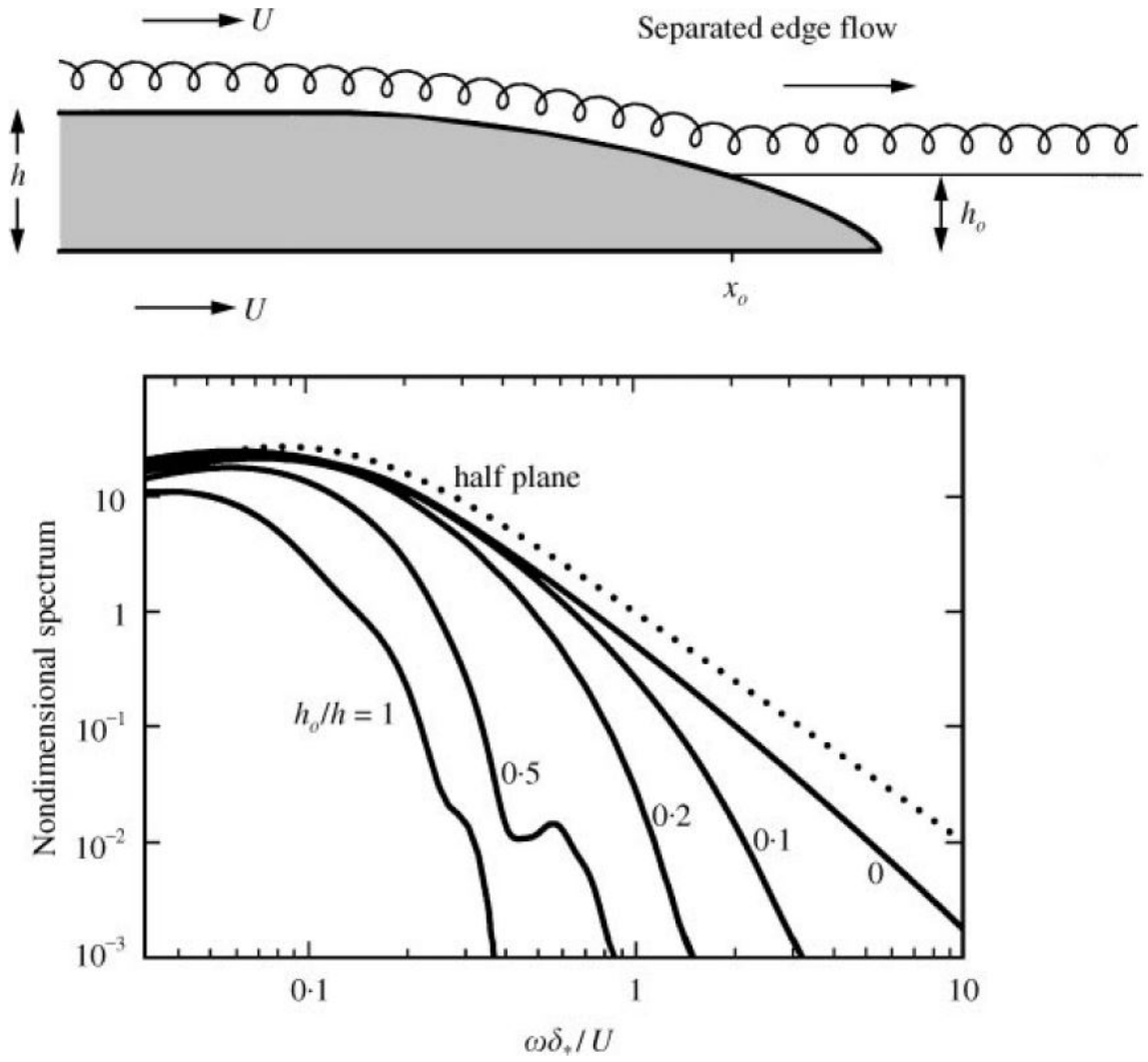

Figure 2.17: Predicted edge-noise spectrum for the rounded edge of thickness $h = \delta$, l=4h, and for the separated edge. Source:Howe (2000)

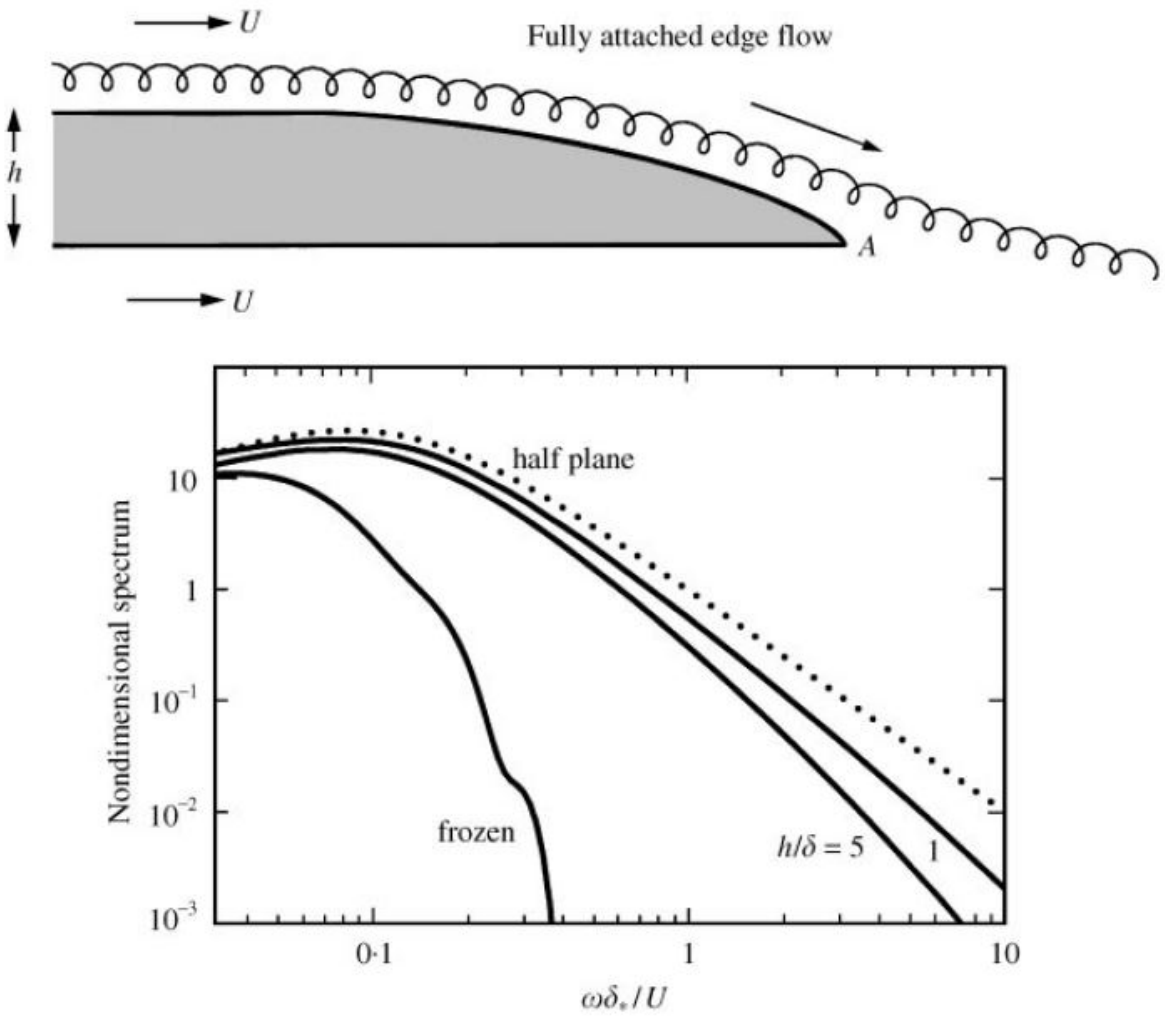

Figure 2.18: Predicted edge-noise spectrum for the rounded edge of thickness when l=4h. Also shown for comparison are the frozen and half-plane spectra. Source:Howe (2000)

Chapter 3

Experimental Techniques and Setup

In the past, different devices and modifications of trailing-edges have been investigated with the aim to reduce noise emissions. Current research aims at applying new tools of flow field interrogation i.e. high-speed planar and tomographic PIV to the problem of trailing-edge noise and at creating links between the phenomenological description of the flow field in terms of coherent structures and noise in order to improve understanding of the noise generating mechanisms. This chapter aims at describing the experimental set-up in detail while giving a brief overview of the experimental techniques. A more detailed description of the experimental technique can be found in the appendix as well as in the literature mentioned in section 3.3.

3.1 Wind Tunnel Facility

The experiments were conducted at the W-tunnel, an open-section low-speed wind tunnel facility at the High-Speed Laboratory of Delft University of Technology. The tunnel starts with a plenum after which the flow goes to the diffuser and than enters the settling chamber. The settling chamber consists of two gauzes to diminish the turbulence intensity. This is followed by a contraction chamber, a small nozzle and the wind tunnel exit. The W-tunnel is an open-jet wind tunnel with a cross-section $0.4m \times 0.4m$ at the exit with a uniform flow within the $0.32m \times 0.32m$ inner region (Bossuyt 2004). The tunnel can operate at a maximum velocity of $35ms^{-1}$. Laser Doppler Velocimetry measurements by Tummers et. al in 1999 confirmed rms of the fluctuating stream-wise velocity component to be less than 0.2% of the free stream velocity. The tunnel is driven by a centrifugal fan which is powered by a 16.5kW electrical motor. In case particles are added to the flow, an external ventilation system can be used to filter the added particles out of the air. A schematic of the W-tunnel has been shown in figure 3.1.

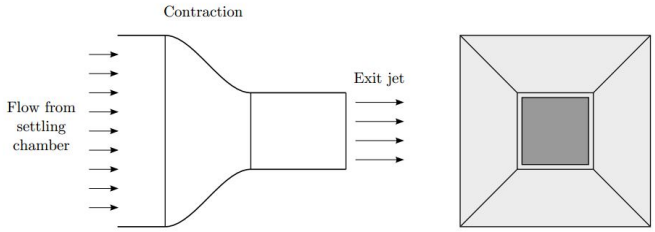

Figure 3.1: Schematic of the W-Tunnel Facility Michelis (2012)

3.2 Trailing Edge Models and Experimental Arrangements

A high surface quality and manufacturing precision is desired for the models used during PIV measurements since slight inaccuracies can alter the boundary layer characteristics and organization of the flow. Therefore the models were made from Aluminium using CNC machining. The model airfoil is designed such that the trailing-edge part is modular and can be exchanged easily. A slot in the leading edge (main part) of the airfoil allows for the attachment of different trailing-edge sections. The models under investigation have a thickness of 20mm, a chord length of 360mm and asymmetric 25 deg beveled trailing edge. The asymmetry results in a net camber and, hence, the upper and lower surfaces will be referred to as the suction and pressure sides, respectively. Three different models with beveled radius of curvatures at the trailing equal to 0, $4 \times t$ and $10 \times t$ were analysed. Consequently, they are named as R0, R4 and R10 respectively. Figure 3.2 shows a schematic of trailing-edge models geometry in isometric view.

The leading edge is an ellipse and the boundary layer was tripped at a distance of 0.23 times the chord length downstream of the leading edge on both surfaces of the airfoil using three dimensional roughness elements. The roughness elements were carborundum grains with a nominal height of 0.841 mm. The trips were 1.0 cm wide and covers the entire span.

The model was installed at the exit of the tunnel at 0deg angle of attack as shown in figure 3.3 using two side plates. For structural reasons and convenient positioning of laser and camera, the airfoil model is placed vertically at the center of test section with its leading edge at a distance of about 5mm from the exit nozzle of the wind tunnel. Geometrical blockage based on the maximum thickness of the airfoil (20mm) and the nozzle exit area of $400 \times 400mm^2$ is 5%. The purpose of the side plates was to support the airfoil structurally and to maintain two dimensionality of the flow. Detailed drawings of the leading edge section of the model and the various trailing edges as well as the calculations for the roughness elements positioning can be found in the Appendix.

There were two coordinates systems used throughout this project and this thesis. The first coordinate system was the main coordinate system used for planar PIV measurements. The streamwise axis is denoted by the x-axis, the direction normal to the streamwise direction by y-axis and the spanwise direction by the z-axis , constituting a left-handed coordinate system.. The origin was placed at the trailing edge. The second coordinate system was used

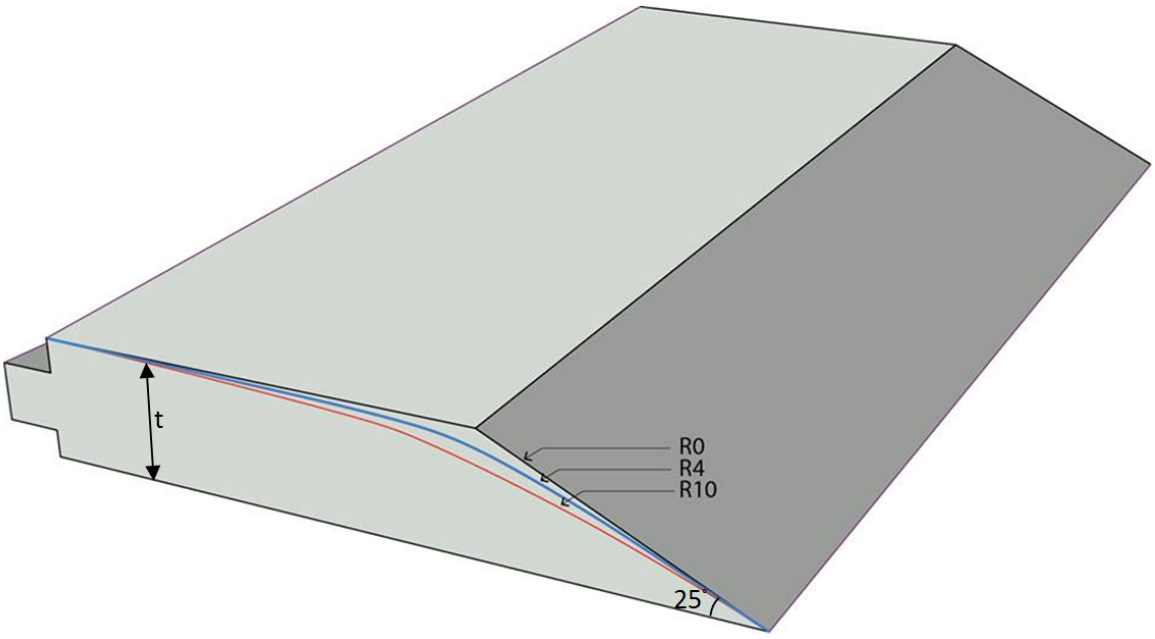

Figure 3.2: Schematic of trailing edge geometry

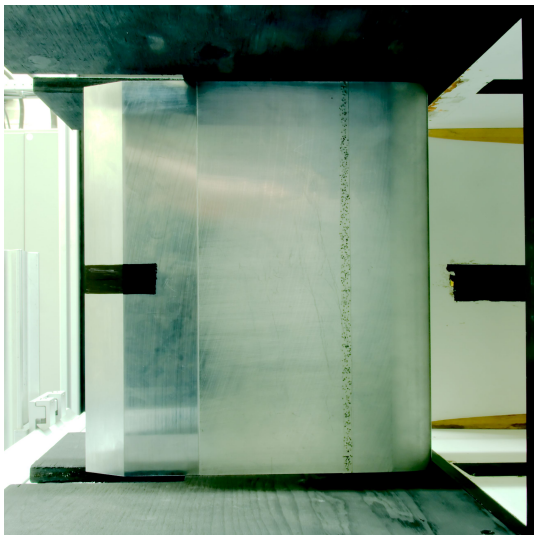

Figure 3.3: Photograph of trailing edge geometry[R0]

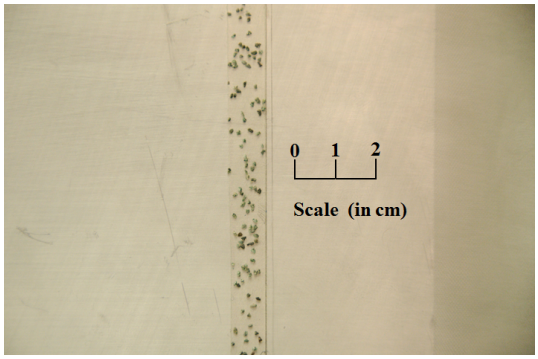

Figure 3.4: Boundary layer tripping using 3D roughness element

for the tomographic measurements with wall tangential axis denoted by X_T and the wall-normal by the X_N-axis and its origin was located again at the trailing edge of the model. Both coordinate systems with respect to model geometry are shown in Figure 3.5.

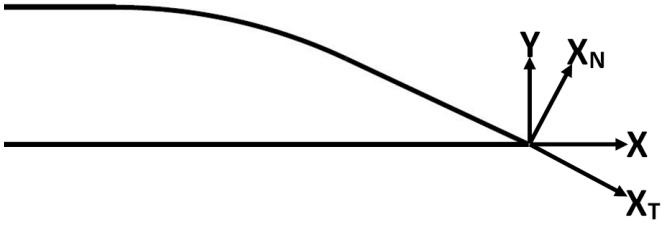

Figure 3.5: Coordinate System

Tests were conducted at free-stream velocities of 5m/s, 10m/s 15m/s and 20m/s for which the experimental parameters are listed in table 3.1. The velocities were adjusted using a pitot tube which was located at the exit of the wind tunnel.

Table 3.1: Experimental Parameters

$U(m/s)$	M_∞	Re_c
5	0.015	1.34×10^5
10	0.03	2.68×10^5
15	0.045	4.02×10^5
20	0.06	5.36×10^5

3.3 High-Speed Particle Image Velocimetry

Particle Image Velocimetry (PIV) is a non intrusive flow measurement technique. The technique has been in use since almost three decades now and has been intensively discussed in a number of books and review articles like Scarano (2013) and Morris (2011). A summary of the various laser velocimetry techniques has been give in Figure 3.6.

High-Speed Particle Image Velocimetry (HS-PIV) is a recently developed to improve our understanding of turbulent flows. Sound propagation is an intrinsically unsteady phenomenon and if one aims at describing the hydrodynamic causes of noise generation, the knowledge of the time evolution of the flow field is an indispensable requirement. Using HS PIV, it is possible to obtain a sequence of velocity vectors close enough in space and time to describe the dynamics of the flow. The time resolution of the velocity field allows for calculating the flow acceleration directly linked to the pressure gradient through the basic conservation equations of fluid mechanics. Pressure (and velocity) variations in time are responsible for the noise generation. A high time resolution of the velocity field would allow a reliable evaluation of the high frequency components of the computed noise spectrum (Lorenzoni, 2008). The use of velocimetry in aeroacoustic predictions was not possible until now because of the relatively low acquisition rate of the laser-camera systems. The state of the art in modern PIV allows for image acquisitions at a rate of over 20,000 images per second with relatively high spatial resolution.

In contrast, numerical flow simulation techniques such as direct numerical simulation (DNS)

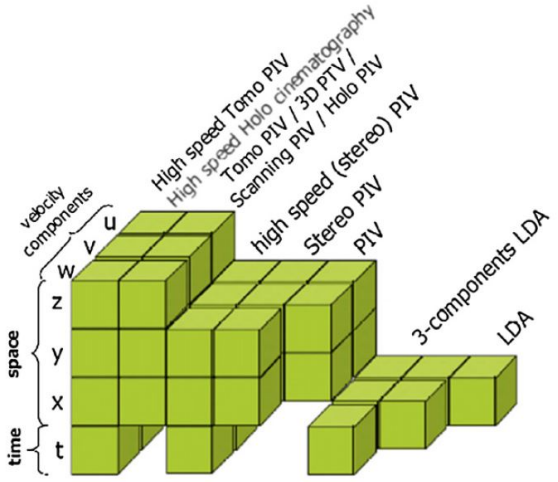

Figure 3.6: Measurement domain and measured components of laser velocimetry techniques. Scarano (2013)

or large eddy simulations (LES) yield nowadays a complete description of the flow structure in the turbulent regime limited by the complexity of the problem and the Reynolds number.

3.3.1 Planar PIV

A schematic underlining the basic working principle of a planar PIV technique has been shown in figure 3.7. The whole set up, in general consists of a seeding system which intersperses tracer particles in the flow, an illumination system consisting of a laser along with the light sheet optics and the imaging and recording system consisting the cameras and the imaging optics.

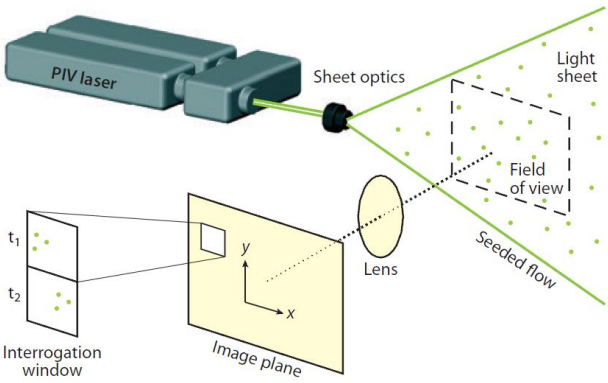

Figure 3.7: PIV working priciple. Morris (2011)

The flow is seeded with small particles used to reflect the laser light. The diameter of the

particles varies depending on the application, but generally is of the order of $1\mu m$. Smaller particles provide better tracking of the true fluid velocity (through Stokes drag) but will provide lower light intensity to the camera. The particles are typically illuminated with a pulsed laser system. Planar PIV generally requires a cylindrical lens to form a light sheet that can be imaged with one or more cameras. Postprocessing is used to divide the field of view into square interrogation windows. The displacement of the particles is then estimated using various types of image correlation algorithms. The displacement is then divided by the time elapsed between the two laser pulses to arrive at a single velocity vector for each interrogation window (Morris, 2011; Probsting, 2011). The results provided by the standard, planar PIV system are realizations of two components of the velocity vector in the plane of the laser sheet [e.g., u(x,y), v(x,y), where the x-y plane is defined by the sheet of the laser]

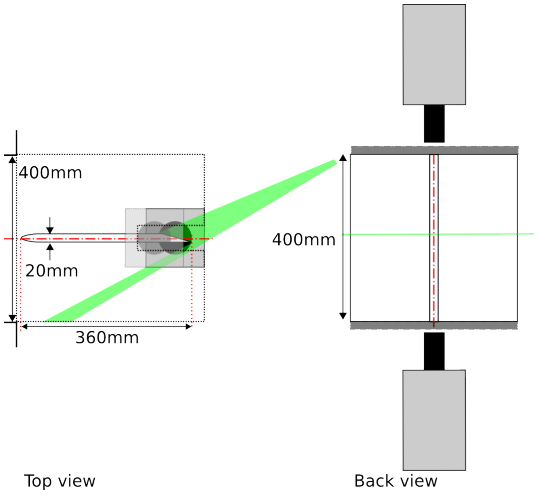

Figure 3.8: Schematic of the set- up for Planar PIV measurements

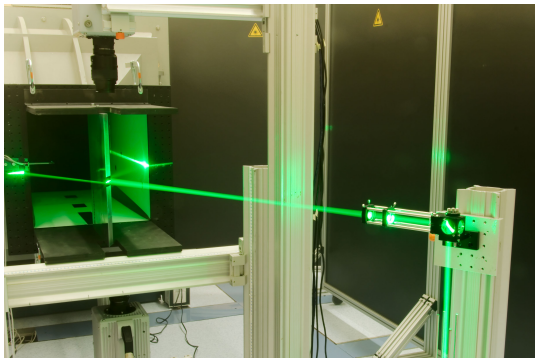

Figure 3.9: Photograph of the set- up for Planar PIV measurements

Figure 3.10: Raw image obtained by upstream camera

Figure 3.11: Raw image obtained by downstream camera

The rapid advancement in high-speed digital cameras and Laser technology has made TR-PIV system capable of acquiring planar PIV image frame pairs at very high frequencies at high spatial resolution. FASTCAM SA1 cameras are capable of over 5400 frames per second(fps) of mega pixels format.

Two Photron FASTCAM SA1 CMOS cameras (1024x1024 pixels, 12-bit, 20μm pixel pitch) were used for the image acquisition. The cameras can operate at full frame at a maximum frame rate of 5.4 KHz and have a storage capacity of 8 GB, allowing the acquisition of a maximum of 5400 images in a single measurement (Probsting, 2011). In order to have a high acquisition frequency, we cropped the cameras to capture 1024×512pixels allowing the measurements at upto 10.8kHz in continuous single frame mode. Two cameras were deployed to increase the spatial resolution. Figure 3.10 and 3.11 shows the raw images for each camera. Each camera was equipped with a Nikon objective with a focal length of 105 mm in order to capture the required field of view. The numerical aperture was set to $f_{\#} = 2.8$.

A dual-cavity pulsed Nd:YLF laser(Darwin Duo) was used for illumination. The laser sheet thickness was estimated by projection onto a millimetric scale and appeared to be approximately 1 mm thick, a dimension comparable to our final interrogation window size. The flow was seeded by means of a stage smoke generator (Safex) that produces particles of approximately 1μm in diameter. The synchronization between laser and camera was performed by means of a LaVision High-Speed controller and by the DAVIS 8.1.3 software package. In order to avoid peaklocking, the particle images are slightly defocussed to yield larger particle image diameters and Gaussian smoothing was used on a kernel of 5×5.

For statistical measurements, PIV image pairs were acquired at a frequency of 125 Hz with a time delay between the first and second frame of 66μs for the 10 m/s free-stream velocity flow. The time delays where chosen as an optimum trade-off allowing enough particles displacement between the two frames (in the order of 2-3 pixels) in the slower regions of our flow while keeping it within reasonable values in the faster regions (typically 16 pixels in the free-stream area).

The pulse frequency was set to 10 kHz in single-frame mode. The laser pulses have a wavelength of 527 nm (visible green light). Optical and PIV parameters for both modes of acquisition have been listed in table 3.2 and 3.3.

Data were processed using a multi-pass algorithm, with the interrogation window sizes tailored to the local flow regime. This approach was chosen to deal with the large dynamic range of the flow. The final passes in all domains were done with interrogation windows of 16×16 pixels with a 75% overlap, giving a vector spacing of 0.16 mm and a spatial resolution of 6.125 vectors/mm.

Table 3.2: Planar PIV parameters for statistical measurements (Double frame mode)

Parameters	Symbol	Value.
Field of View	FOV	42mm $\times 21mm$.
Magnification	M	.0.49
Focal Length of Lens	f	105mm .
Numerical Aperture	$f_{\#}$	5.6 .
Maximum particle displacement	dx	20 pixels.
Sampling frequency	f_s	125 Hz.
Number of Samples	N	800.

Table 3.3: Planar PIV parameters for high-speed measurements (Single frame mode at U_∞ = 10 m/s)

Parameters	Symbol	Value.
Field of View	FOV	42mm $\times 21mm.$
Magnification	M	.0.49
Focal Length of Lens	f	105mm .
Numerical Aperture	$f_\#$	2.8 .
Sampling frequency	f_s	10,000 Hz.
Number of Samples	N	10,000.

3.3.2 Tomographic PIV

Tomographic PIV is a recently developed technique which gives all three velocity components in a volume of fluid. The technique is based on the illumination, recording, reconstruction and analysis of tracer-particle motion within a three-dimensional measurement volume (Elsinga et al., 2008). The recently developed technique makes use of typically 4 simultaneous views of the illuminated particles and their three-dimensional reconstruction as a light-intensity distribution by means of optical tomography. The reconstruction is performed with the MART algorithm (multiplicative algebraic reconstruction technique), yielding a 3D distribution of light intensity discretized over an array of voxels(equivalent to pixels in 2D). The reconstructed pair is then analyzed by means of 3D cross-correlation returning the three-component velocity vector distribution over the measurement volume. The implementation of the tomographic technique in time-resolved mode by means of high repetition rate PIV hardware has the capability to yield 4D velocity information. The working principle of tomographic PIV has been schematically represented in figure 3.12. For a more detailed discussion on the measurement technique, the reader can refer to Elsinga et al. (2006) and Scarano (2013).

For tomographic measurements the positioning of the model is not changed compared to the experiments described in the previous sections. Figure 3.14 shows the schematic diagram of the experimental set-up including cameras and light-sheet optics, while figure 3.13 shows photographs of the implementation. The imaging system is typically composed of four cameras aligned in cross-like or linear imaging configurations as shown in Figure 3.15. The choice of a one- or two-dimensional array of cameras is often dictated by constraints on optical access or complexity of camera installation. For the present analysis, the cameras were positioned at angles of about $-40\,\text{deg}$, $-15\,\text{deg}$, $15\,\text{deg}$, $40\,\text{deg}$, in the spanwise-wall-normal plane with $0\,\text{deg}$, defined by the the wall-normal with respect to the local airfoil surface at the trailing-edge.

Light is emitted by a laser head positioned on the ground below the model. The multi-pass light amplification system was used. The system is based on the principle that the circular light beam is sent with a small angle into a region bounded by two highly reflective mirrors (reflectivity higher than 99%). The beam is reflected several times (typically 20) before exiting in such a way that the entire measurement volume is illuminated. Figure 3.16 depicts the method showing illumination of the measurement volume (Ghaemi and Scarano, 2010). Due to the presence of a reflecting surface and in order to remove flow energy fringes at the

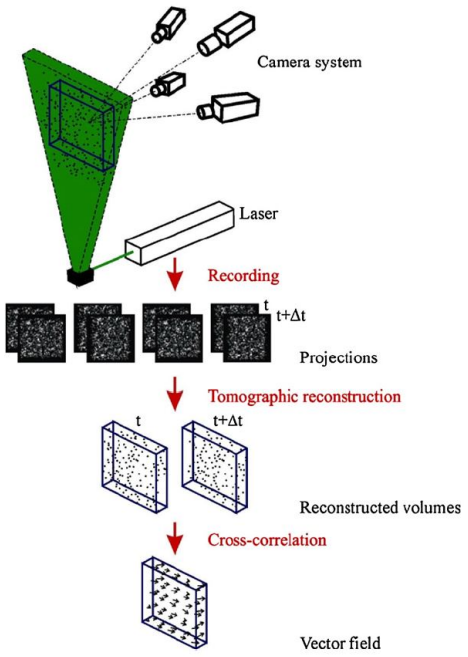

Figure 3.12: Working Principle of tomographic PIV. Source: Elsinga et al. (2006)

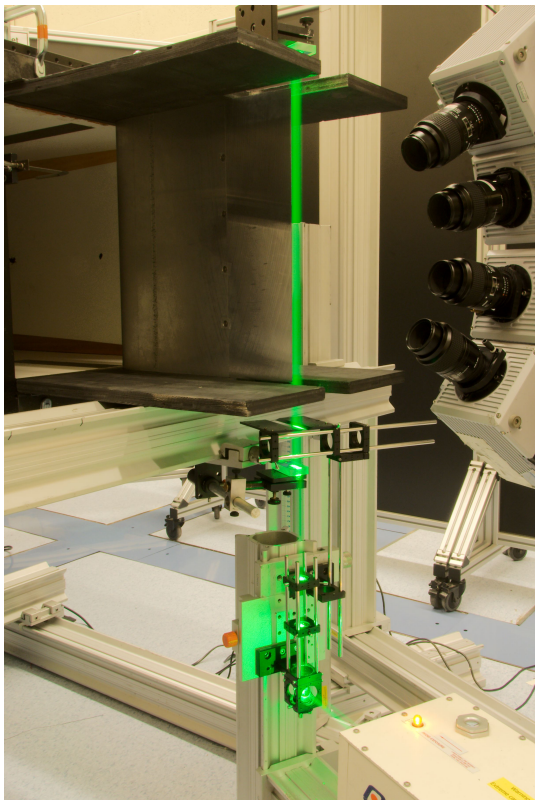

Figure 3.13: Photograph of the set-up for tomographic measurements

outer regions of the circular beam knife-edge slit filters with a width of about 7mm in front of the mirrors were applied. The detailed functioning principles and design optimization are explained by Ghaemi and Scarano (2010), who measured the light intensity gain and reported a factor of 7 and 5 with respect to the corresponding single and double-pass configurations, respectively.

Size of the measurement volume is limited by the available laser power and desired resolution, leading to a compromise of $50 \times 25 \times 7mm^3$. The measurement volumes have been described in chapter 5 which discusses the result of tomographic PIV. Statistical measurements are recorded at a frequency of 125Hz and high-speed image sequences at a frequency of 10kHz. For the synchronisation between cameras, laser and the image acquisition system a LaVision programmable timing unit is used, which is controlled by the LaVision Davis 8.1.3 software.

Four Photron Fastcam SA1 cameras are used for imaging. All cameras are equipped with Nikon lenses having a focal length of 105mm. Due to the increased scattering efficiency for the cameras at 40 deg caused by forward and backward scattering as predicted by Mie's scattering theory, and more stringent requirements concerning the depth of field, the numerical aperture for the cameras at the extreme angles are set to $f\# = 16$ while for the cameras in side scattering position it is set to $f\# = 11$. Additionally, Scheimpflug(lens tilt) adapters

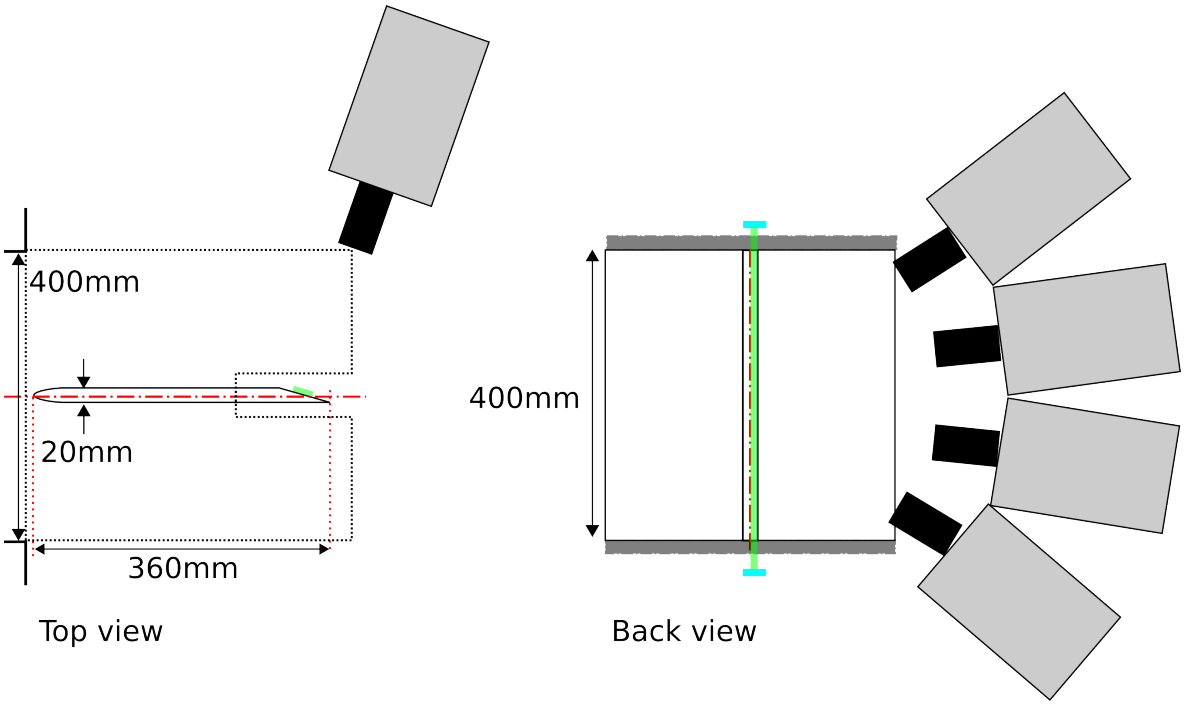

Figure 3.14: Schematic of the set-up for tomographic measurements

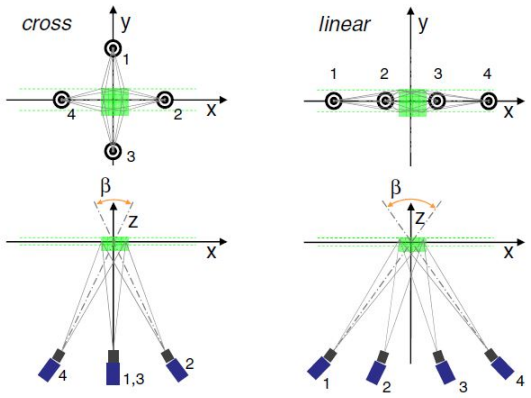

Figure 3.15: Imaging Configurations for tomographic PIV: Scarano (2013)

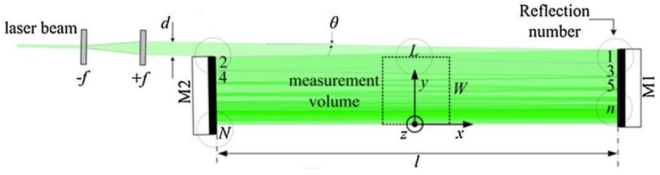

Figure 3.16: Mutipass light amplification system for tomographic PIV.Source: Ghaemi and Scarano (2010)

were used to align the focal with the object plane.

Self-calibration, reconstruction and correlation of the data is accomplished using the LaVision Davis 8 software package. Self-calibration is applied to reduce the residual of the calibration to less than 0.1px, therefore increasing the quality of the reconstruction. The parameters characterizing the tomographic PIV system used here are summarized in table 3.4 and 3.5.

Table 3.4: Tomographic PIV parameters for statistical measurements (Double frame mode)

Parameters	Symbol	Value.
Measurement Volume	V	50mm $\times 25mm \times 7mm$.
Magnification	M	.0.4096
Focal Length of Lens	f	105mm .
Numerical Aperture	$f_{\#}$	16-11-11-16 .
Maximum particle displacement	dx	20 pixels.
Sampling frequency	f_s	125 Hz.
Number of Samples	N	800.

Table 3.5: Tomographic PIV parameters for high-speed measurements (Single frame mode at $U_\infty = 10$ m/s)

Parameters	Symbol	Value.
Field of View	FOV	50mm $\times 25mm \times 7mm$.
Magnification	M	.0.49
Focal Length of Lens	f	105mm .
Numerical Aperture	$f_{\#}$	16-11-11-16 .
Sampling frequency	f_s	10,000 Hz.
Number of Samples	N	5,000.

3.4 Data Reduction

The following sections gives a general overview of the procedure followed for the determination of the flow and acoustic properties. First, some of the advanced image interrogation techniques which were used in the present study are presented. Then follows the description of the vortex identification method. Finally, a brief overview of the power spectral density estimation method, correlation and coherence of the fluctuating velocities have been presented.

3.4.1 Image interrogation techniques

In order to increase the temporal resolution of the flow field using high-speed PIV, high-speed digital cameras with CMOS sensors and high repetition rate lasers have to be employed. Modern CMOS cameras can acquire images at comparable frame size to CCD cameras and much higher frames per second; though the larger pixel size, higher noise and lower sensitivity yield inferior image quality with respect to CCD cameras. Furthermore, the pulse energy of

diode pumped Nd:YLF lasers operating in the kilohertz range typically does not exceed 20 mJ and drops well below 10 mJ at 10 kHz (Sciacchitano et al., 2012). The combination of lower image quality of CMOS cameras and weaker illumination of high repetition rate lasers are the principal causes of the reduced accuracy and precision of high-speed PIV systems, as also documented in the results of the most recent PIV challenge Stanislas et al. (2008). In order to overcome these challenges to a certain extent, two advanced images interrogation methods, namely the sliding sum of correlation and fluid trajectory correlation were used for used for planar and tomographic PIV respectively.

The sliding averaged correlation (SAC) or the sliding sum of correlation (SOC) technique aims at reducing random error through combining multiple correlations over a set of adjacent image pairs. The technique has been demonstrated to increase the robustness of velocity estimates (Meinhart et al., 2000) and is currently widely practised. For high-speed PIV measurements where the acquisition rate is sufficiently high, correlation map averaging over a sliding kernel can be applied. A preliminary analysis of the method on experimental data was performed by Violato and Scarano (2011), where a reduction of random noise was observed. The SAC technique increases accuracy by reducing the random error through the summation of multiple correlations. The average correlation function has a much higher signal to noise ratio than the instantaneous correlation functions as demonstrated in Figure 3.17.

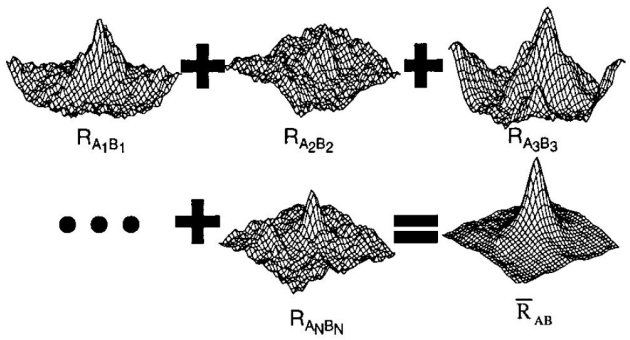

Figure 3.17: Instantaneous cross correlation functions that are averaged together to produce an average correlation function. Source: Meinhart et al. (2000)

However, the amount of reduction available is limited in flows with large curvature or acceleration due to the lower number of images which can be used. For the present analysis, a set of two adjacent image pairs was used for correlation of planar PIV data.

The fluid trajectory correlation (FTC) technique is a novel method to improve accuracy of high-speed PIV image analysis by adapting correlation-based algorithms to explicitly account for the effects of curvature and accelerations through an image sequence (Lynch and Scarano, 2012). The method is intended as a corrector for velocity fields obtained using traditional PIV algorithms. The algorithm has been found more capable than traditional PIV algorithms for tracking nonlinear motion in time due to the unique trajectory finding procedure and least-squares fitting. Additionally, the algorithm is able to use a larger number of images compared to other correlation averaging approaches since a linear predictor is not assumed across the

sequence. The achievable reductions in random errors are shown to be highly dependent on the choice of fitting function applied to the determined trajectory Lynch and Scarano (2012). The present analysis was done using a set of 7 images with a polynomial of second order as a fitting function on the tomographic PIV data.

3.4.2 Vortex identification techniques

The main advantage of a high-speed tomographic PIV measurements compared to the other experimental techniques is the simultaneous evaluation of all components of the velocity velocity vector within a volume. This makes the use of vortex detection methods to understand organization of turbulent motions possible. The criterion which is used in the present study, namely, the Q-criterion for vortex identification shares some properties with both the vorticity and the pressure criterion. The Q-criterion was named after the second invariant of velocity gradient tensor ∇u by J. C. R. Hunt (1988). Hunt et al. defined the so called eddy zones as strong swirling zones with vorticity. The second invariant Q is:

$$Q = \frac{1}{2}(\Omega_{ij}\Omega_{ij} - S_{ij}S_{ij}) \tag{3.1}$$

where Ω_{ij} and S_{ij} are respectively the antisymmetric and the symmetric components of ∇u. In other words, Q is the balance between the rotation rate and the strain rate . The implication of the latter observation is fairly straightforward: positive Q isosurfaces isolate areas where the strength of rotation overcomes the strain, thus making those surfaces eligible as vortex envelopes. Further support can be found by recasting (3) in a form which relates to the vorticity modulus

$$Q = \frac{1}{4}(\Omega_{ij}^2 - 2S_{ij}S_{ij}) \tag{3.2}$$

Since vorticity should increase as the centre of the vortex is approached, Q can be expected to remain positive in the core of the vortex. In its original formulation the criterion bears the additional condition that the pressure should attain a minimum in a vortex core. In velocity field measurement techniques such as particle image velocimetry the pressure field is not available and thus only the part of the definition based on the invariant is taken into account.

3.4.3 Power spectral density

The autocorrelation of a single variable u(t) at two times t_1 and t_2 is defined as

$$R(t_1, t_2) = \overline{u(t_1)u(t_2)} \tag{3.3}$$

where overline average indicates an average over time. For a stationary process, the statistics are independent of the origin of time so that we can shift the origin of time by any amount. We can therefore define auto-correlation function of a stationary process by a

$$R(t) = \overline{u(t)u(t+\tau)} \tag{3.4}$$

The Fourier transform of $R(\tau)$ is called the Power Spectral Density (PSD).

$$S(\omega) = \frac{1}{2\pi} \int_{-\infty}^{+\infty} R(\tau) e^{-i\omega\tau} \, d\tau \tag{3.5}$$

Substitution of $\tau = 0$ in equation and taking the inverse fourier transform gives

$$\overline{u^2} = \int_{-\infty}^{+\infty} S(\omega) \, d\omega \tag{3.6}$$

This shows that $S(\omega)d\omega$ is the energy (more precisely, variance) in a frequency band $d\omega$ centered at ω. Therefore, the function $S(\omega)$ represents the way energy is distributed as a function of frequency ω. We say that $S(\omega)$ is the energy spectrum, and equation shows that it is simply the Fourier transform of the autocorrelation function.

Welch's method, named after P.D. Welch (Welch, 1967), was used for the power spectral density estimation. In this method, the input signal vector is divided into a number of overlapping segments. A each section is windowed with a Hamming windowing function can be applied to each of these segments in order to avoid the effects of windowing for short time series. Consequently the periodograms are computed for each segment independently by means of the FFT and finally averaged to yield an estimation for the PSD of the signal. The obtained power spectral density is normalised using characteristic length and velocity scales of the flow and than the logarithm is taken to display the final results in decibels.

3.4.4 Correlation and coherence

To get an idea of the length scales of the fluctuating motion, we study the correlation between the same fluctuating quantity measured at two different points in space. The correlation coefficient along the spanwise direction is defined as:

$$\rho(x, y, \Delta z) = \frac{\overline{u(x, y, z) u(x, y, z + \Delta z)}}{\overline{u(x, y, z)^2}} \tag{3.7}$$

Physically, the correlation with separation Δz is a measure of the strength of eddies whose length along the z direction is greater than the magnitude of Δz since eddies smaller than this will not contribute to the correlation. When we speak of the length scale of the energy containing eddies we mean a length of order

$$L_\rho = \lim_{L \to \infty} \int_0^L \rho(x, y, \Delta z) \, d\Delta z \tag{3.8}$$

However, this is an imprecise concept in the sense that we ignoring the frequency content corresponding to each length scale. Infact, it is more instructive to look into these length scales in the frequency domain which has been discussed in the remaining of the chapter. The coherence length is defined in terms of the coherence function, which involves the auto-power and cross-power density of the signals, where $\phi(\omega, z_1, z_2)$ denotes the cross-power spectral

density between two points along a given dimension and $\Delta z = z_2 - z_1$ is their spatial separation (Pröbsting et al., 2013).

$$\gamma^2(\omega, \Delta z) = \frac{\mid \phi(\omega, z_1, z_2) \mid^2}{\mid \phi(\omega, z_1, z_1) \mid\mid \phi(\omega, z_2, z_2) \mid} \tag{3.9}$$

Note that this representation applies for the case that the flow statistics are homogeneously distributed along the spatial dimension, stationary in time and for an infinite observation period. For a at plate boundary layer the first condition is fulfilled when considering the spanwise dimension and, with restriction to short separations, for the streamwise direction (Pröbsting et al., 2013).

By definition, the coherence length is related to the integral of the coherence function $\gamma^2(\omega; \Delta z)$ over the spatial separation and therefore reduces to a function of frequency only.

$$l_z(\omega) = \lim_{L \to \infty} \int_0^L \gamma(\omega, \Delta z)\, d\Delta z \tag{3.10}$$

Numerator term of the coherence function was calculated using cross power spectral density function in Matlab which estimates the coherence of the discrete-time signals using the Welch's averaged, modified periodogram method of spectral estimation.

Chapter 4

Flow Structure and Aeroacoustic Sources

In this chapter, the results of the planar PIV experiments conducted on the beveled trailing edges will be discussed. The chapter makes an attempt to describe the flow field around a beveled trailing edge with the emphasis on understanding the flow features that affect aeroacoustic emission from the trailing edge. Section 4.1 presents the time averaged flow properties identifying some common flow features around trailing edges. Section 4.2 deals with the instantaneous organisation of velocity and vorticity and the spectral analysis. Next, the aeroacoustic analysis of the flow is presented in Section 4.3. Ffowcs-Williams and Hall's analogy will be implemented to compute potential sound sources around the trailing edge.

4.1 Velocity Field Statistics

The time averaged flow properties presented in this section were obtained from an ensemble of 800 velocity fields. The acquisition frequency of 125Hz makes the time separation between consecutive samples $\Delta T = 8ms$, corresponding to a path length of 80mm(4t). The samples are therefore considered uncorrelated. The freestream velocity U_∞ varies from 5 to 20 m/s and the corresponding Reynolds number based on the chord length c varies from $Re_c = 1.34 \times 10^5$ to $Re_c = 5.36 \times 10^5$.

An online analysis of the results obtained from the planar PIV suggested that the transition occurs around $Re_c = 1.82 \times 10^5$. It should be noted that transition is a very sensitive flow phenomenon and, as such, can be strongly affected by the experimental conditions. To ensure that the flow being analysed is always turbulent, the Reynolds Number for the most of the remaining analysis was taken as $Re_c = 2.68 \times 10^5$. Such a value ensured the flow to be always turbulent, while allowing the high-speed PIV system to operate in single frame continuous mode at a rate of 10kHz. At higher flow velocity, the time separation of $100\mu s$ would be inadequate (too large) for a reliable cross correlation analysis. Figure 4.1 shows the streamwise velocity contours for the laminar flow conditions at $Re_c = 1.34 \times 10^5$. Based on the

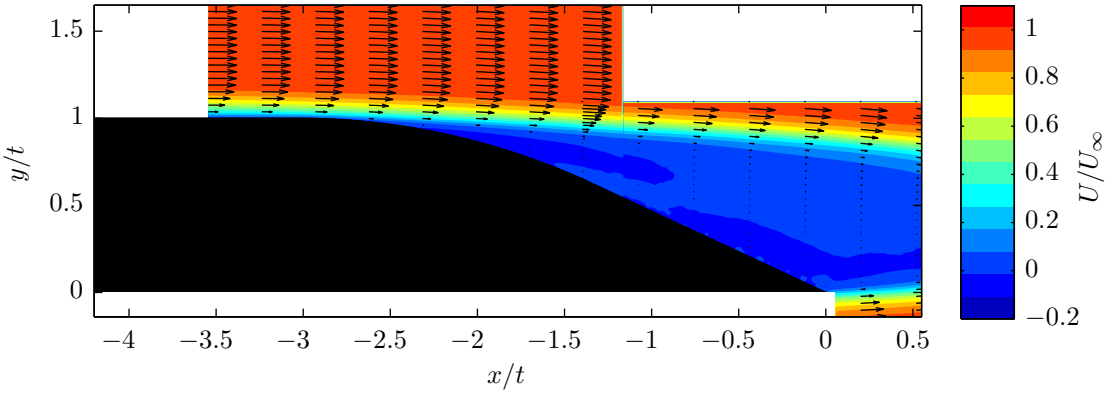

Figure 4.1: Contours of Streamwise Velocity for R4 at $Re_c = 1.34 \times 10^5$

important flow features studied by previous researchers (Blake, 1984; Wang and Moin, 2000; Shannon and Morris, 2006) in a planar BTE geometry, the flow with turbulent incoming boundary layer can be distinguished into four main regions namely, the upper shear layer region, separation bubble or recirculation zone, the lower shear layer and the wake. These regions have been visualized by contour plots of streamwise velocity and Reynolds stress in Figure 4.2 and 4.4 for R4. The general characteristics of a BTE flow begin with an upstream turbulent boundary layer on the suction side separating due to the adverse pressure gradient that develops into a shear layer. The lower boundary layer remained relatively undisturbed before separating suddenly at the sharp edge. The low momentum fluid contained in the separated region was bound by high momentum fluid on either side, generating two regions of shear in the near wake.

Figure 4.4 shows the contours of RMS velocities at $Re_c = 2.68 \times 10^5$ for R4. The contours show the existence of two local regions of relatively high turbulence, the upper and the lower shear layer. It can also be observed that the shear layer grows in size as the flow progresses downstream. This point has been further illustrated in the consecutive section.

The velocity profile for R4 at $Re_c = 2.68 \times 10^5 (\approx 10 m/s)$ were plotted at the streamwise stations x/t=-3.125, -2.125, -1.625, -1.125 and -0.625 in a coordinate system originating from the trailing edge. These points correspond to the measurement stations of Blake's experiment Blake (1975, 1984). The boundary layer thickness δ_{99} the displacement thickness and momentum thickness at x/t=-3.125 were estimated to be 5mm, 0.6142mm and 0.5075mm respectively. These values matches closely to those obtained by Moin and Wang by LES simulations on a similar profile as discussed in Chapter 2. The turbulent boundary layer develops under an adverse pressure gradient and velocity profiles shows that the separation occurs slightly upstream of x/t=-1.125.

It can also be observed from Figure 4.2 that the flow profile changes as the bevel radius of curvature increases because the corresponding adverse pressure gradient also decreases. Figure 4.6 shows the contours of streamwise velocity for R4 at a higher Reynolds number of $Re_c = 5.36 \times 10^5$. It can be inferred from the plot that separation occurs downstream as compared to the smaller Reynolds number discussed before. This might be due the fact that

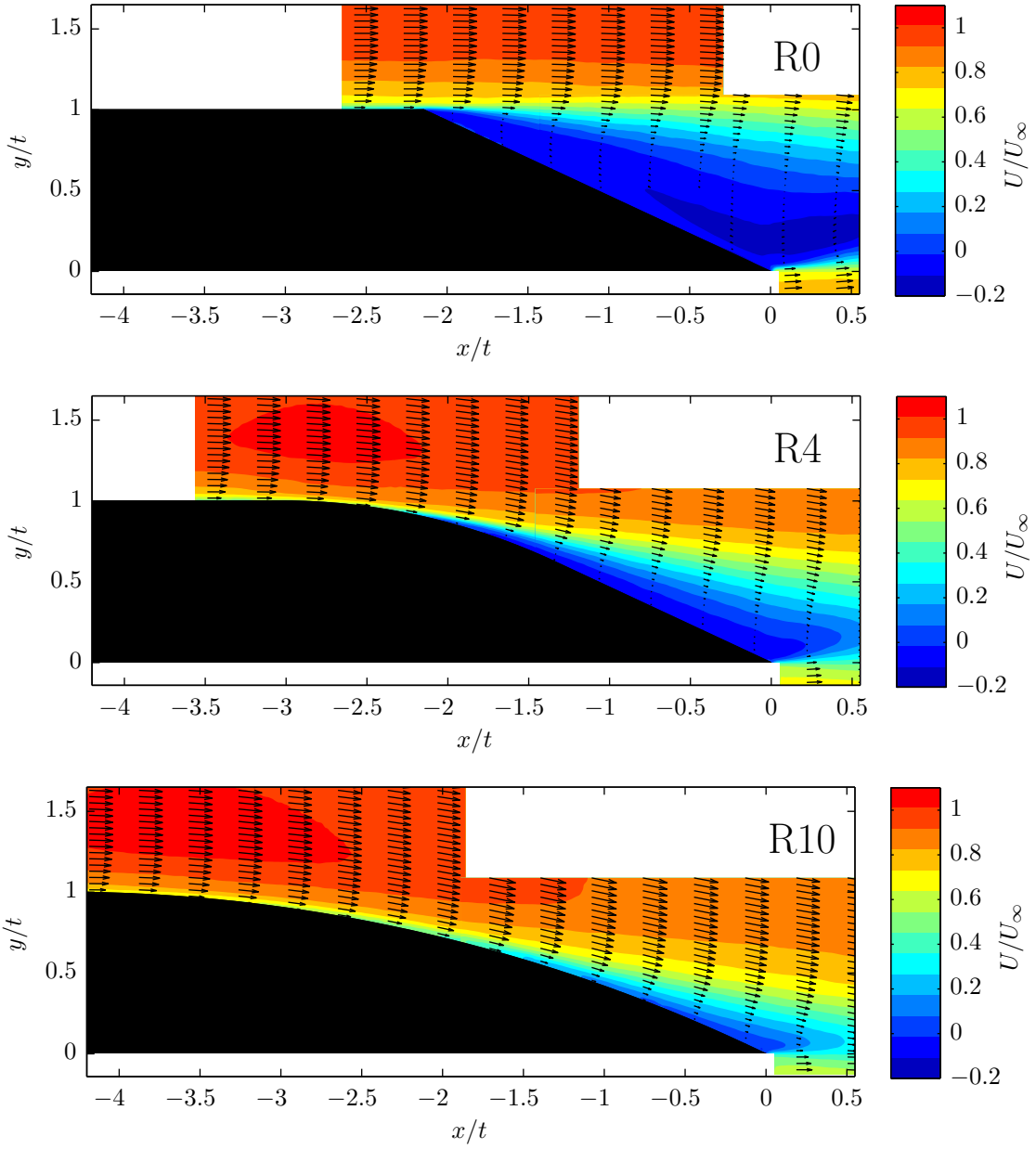

Figure 4.2: Contours of Streamwise Velocity for all Profiles at $Re_c = 2.68 \times 10^5$

the separation resistance of a turbulent boundary layer increases with increasing Reynolds number. This is most likely the reason that we observed late separation for the LES results obtained by Moin and Wang though they used an almost similar geometry.

The four regions described in this section in a whole comprise the important features of a BTE flow that can be altered or controlled to achieve desirable outcome such as, reduced drag, noise and vibrations. Hence, it is essential to understand these flow features to control the flow dynamics.

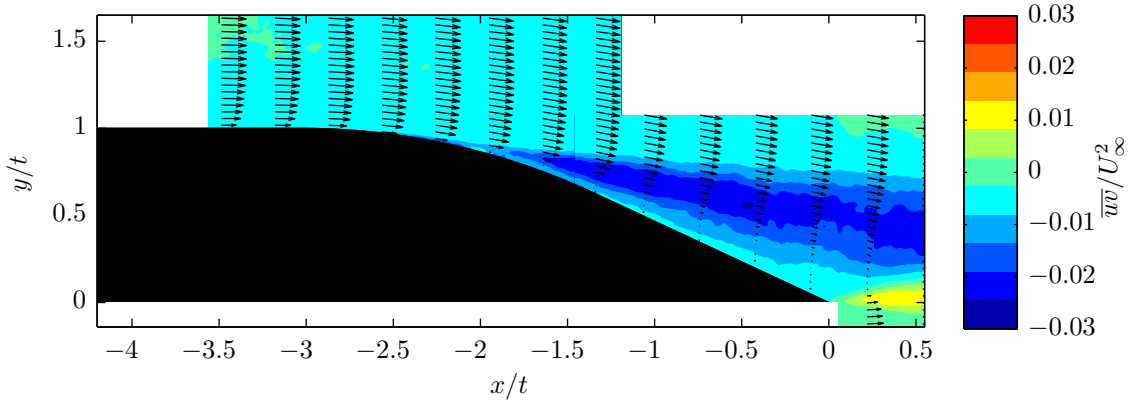

Figure 4.3: Contours of Reynolds Shear Stress for R4 at $Re_c = 2.68 \times 10^5$

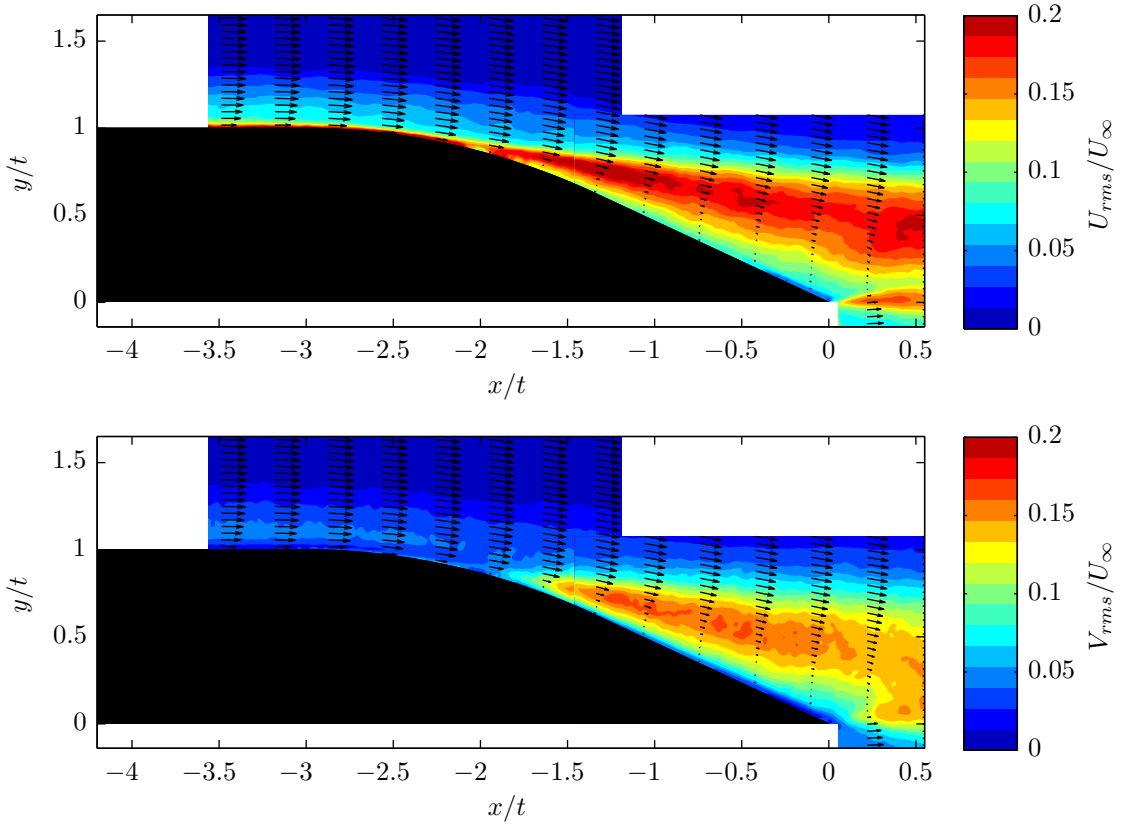

Figure 4.4: Contours of RMS velocity for R4 at $Re_c = 2.68 \times 10^5$

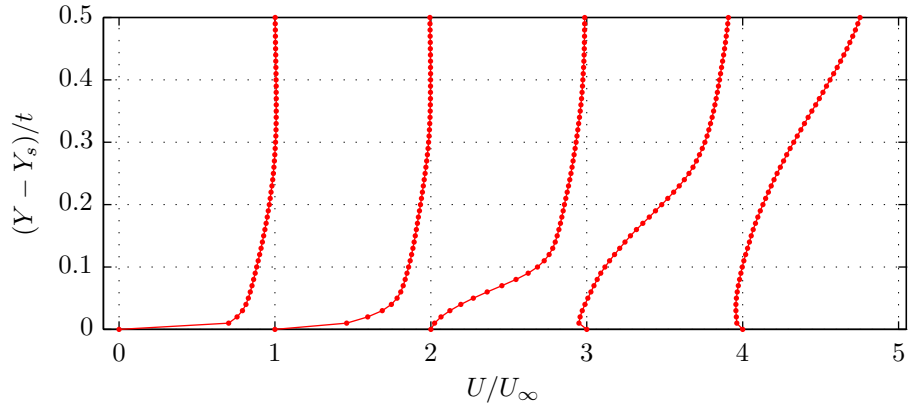

Figure 4.5: Profiles of the normalized mean streamwise velocity (R4 at $Re_c = 2.68 \times 10^5$) as a function of vertical distance from the upper surface, individual profiles are separated by a horizontal offset of 1 with the corresponding zero lines located at 0, 1,..,4.

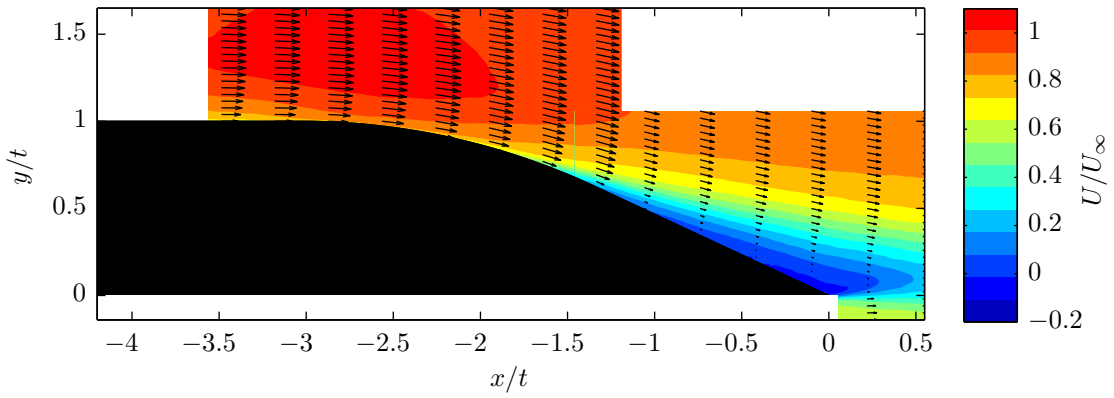

Figure 4.6: Contours of Streamwise Velocity for R4 at $Re_c = 5.36 \times 10^5$

4.2 Instantaneous Velocity and Vorticity Organisation

The instantaneous flow properties presented in this section were obtained from the time resolved Planar PIV measurements at the acquisition frequency of 10kHz. Figure 4.7 depicts contours of the instantaneous streamwise velocity normalised with the freestream velocity. The flow features discussed in the previous section can also be observed in this plot using the velocity vectors. The reversal in the direction of velocity vectors clearly demonstrates the separated flow region and the large variation shows the region of high shear identified as the shear layer. The variations in the instantaneous and averaged velocity fields supports the argument of Blake (1984) that the region of separation was not just a zone of constant flow reversal, rather it was a zone of oscillatory motion with equal tendency of of flow upstream and downstream.

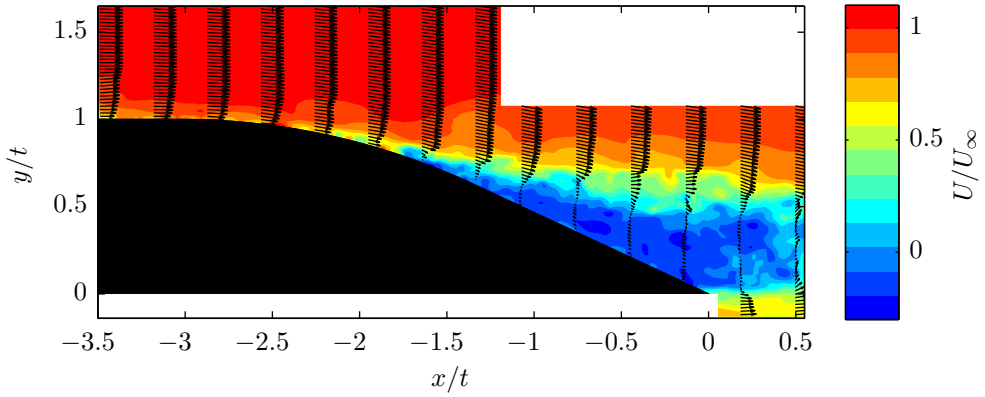

Figure 4.7: Contours of instantaneous streamwise velocity for R4 at $Re_c = 2.68 \times 10^5$

Figure 4.8 shows the instantaneous streamwise velocity for R0 and R10. R0 has boundary layer separation over the wedge region with an extensive zone of recirculating motion. For the R10 profile, flow separation does not occur. This can attributed to the less intense adverse pressure gradient due to larger surface curvature.

A sample of three snapshots is shown in Figure 4.9, where $\Delta T = 1.5ms$ between consecutive snapshots and the color levels represent the spanwise vorticity normalised with free stream velocity(U_∞) and thickness parameter t.

This instability mechanism involving vortical motions observed in the shear layer can be related to the Kelvin-Helmholtz Instability. The instability does not form symmetrical vortex pairs due to the asymmetry in the trailing edge geometry. The turbulent structures in the shear layer entrain irrotational fluid from the non-turbulent region outside the shear layer. This flow entrainment causes the formation of a low velocity recirculation in the region, which is located between the shear layer and the adjacent surface. The vorticity shed into the wake from the pressure side formed relatively higher concentrations of positive vorticity which rolls near the trailing edge. The suction side is subjected to an adverse pressure gradient which causes the (negative) vorticity to diffuse after separation. Consequently, vorticity convected

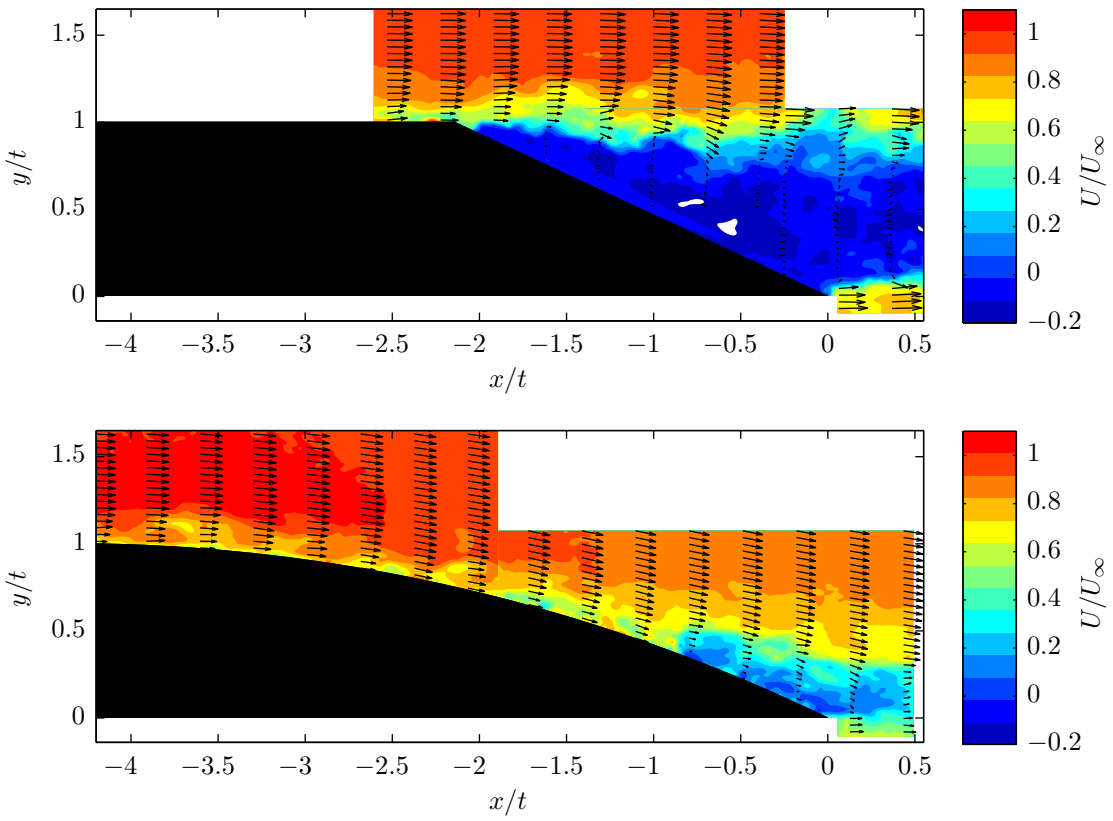

Figure 4.8: Contours of instantaneous streamwise velocity for R0 and R10 at $Re_c = 2.68 \times 10^5$

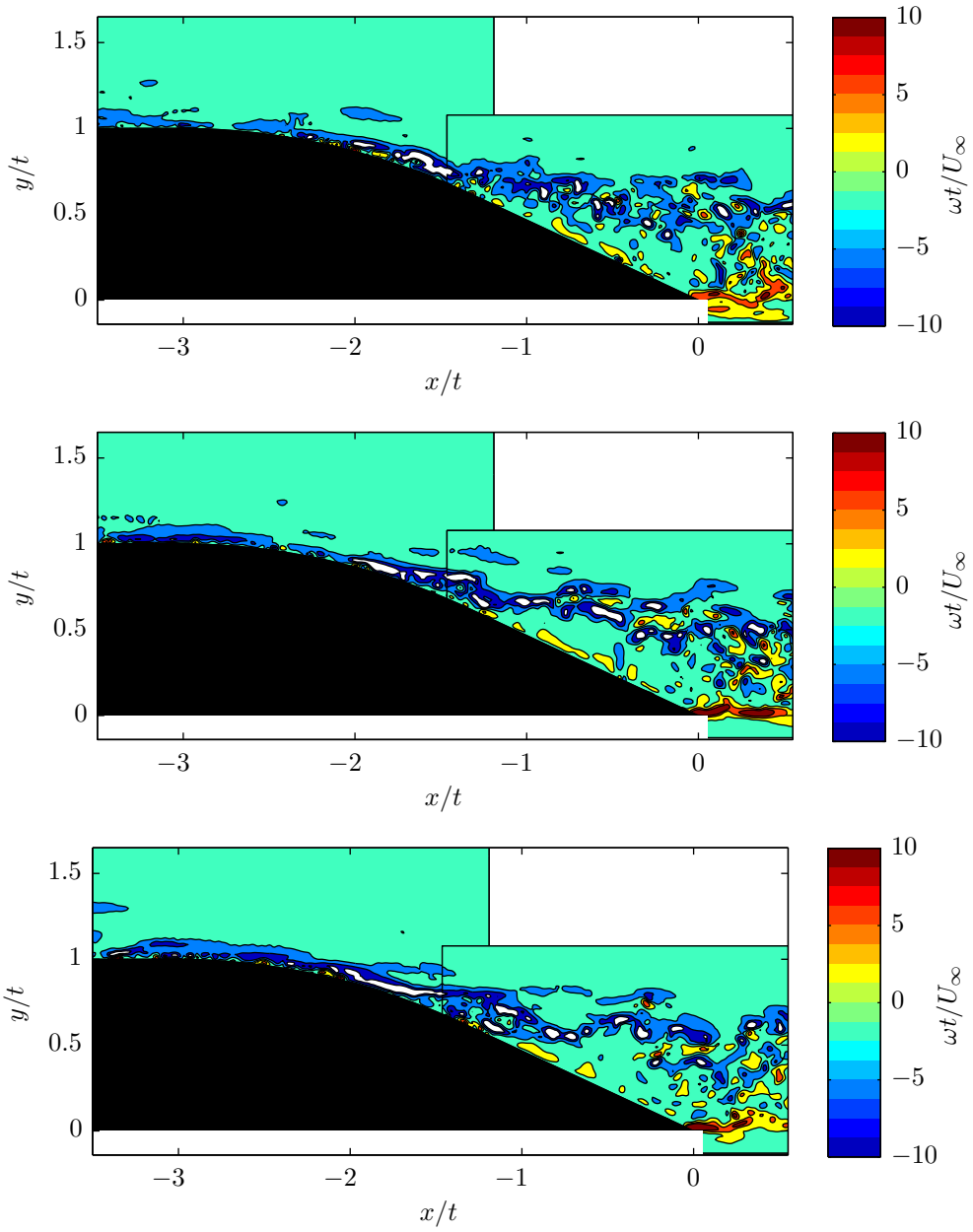

Figure 4.9: Contours of Spanwise Vortictiy ω for R4 at $Re_c = 2.68 \times 10^5$

from the upper surface does not roll up into compact motions and forms a more diffuse region of shear that included groupings of smaller scale motions. Similar observations has also been made by Shannon and Morris (2006) in their work on the beveled trailing edges.

The vortex core convecting in the shear layer can also be visualized from the closely spaced patches of positive and negative vertical velocities (v/U_∞) in Figure 4.10(b). Here also the consecutive snapshots are separated by a $\Delta T = 1.5ms$. The realization in Figure 4.10 shows two relatively compact structures of opposite fluctuations (denoted by red and blue contours)

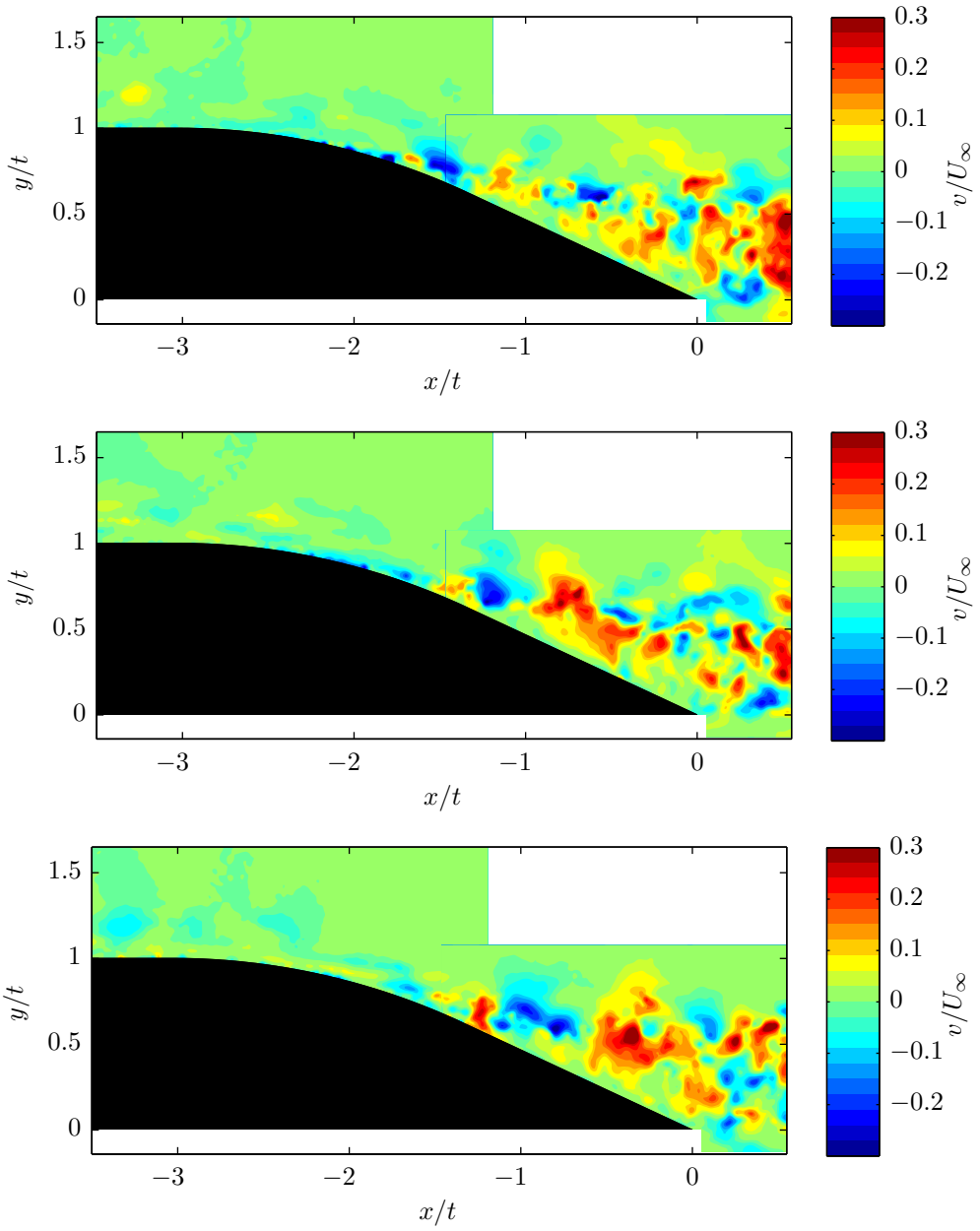

Figure 4.10: Contours of the fluctuating vertical velocity v for R4 at $Re_c = 2.68 \times 10^5$

separated by a length of approximately $\lambda_s = 0.75t$ slightly downstream of the beveled corner. An analysis shows that the convecting velocities of these structures is approximately $U_c = 0.5U_\infty$. This gives a $\Delta T = 3ms$ and f=333Hz and represents the frequency of the oscillatory vortical motions in the upper shear layer.

A peculiar feature of the vorticity plots in 4.9 is the streamwise elongated structures with large values of spanwise vorticity at the height almost equal to edge of the the boundary layer. To the knowledge of the author, such structures have not been reported previously

in the literature. This makes their observation more intriguing and demanding in terms of understanding the physical mechanism behind their birth. It is proposed that these structures might result from the combined effect of the local region of high velocity at the point of minimum pressure and due to the curvature effect of the trailing edge.

We will consider an illustrative model to demonstrate the effect of curvature on pressure profile in the wall normal direction (Figure 4.11).

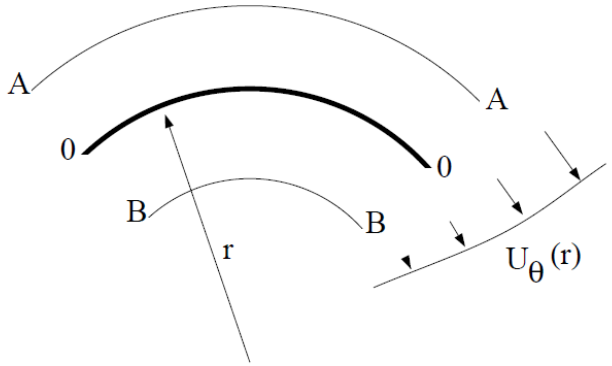

Figure 4.11: Curved boundary layer flow along r=constant,$U_r = 0$ (Davidson et al., 2003)

A polar coordinate system $r - \theta$ with θ locally aligned with the streamline is introduced. As $U_\theta = U_\theta(r)$ (with $\partial U_\theta / \partial U_r > 0$ and $U_r = 0$), the radial inviscid momentum equation degenerates to

$$\frac{\rho U_\theta^2}{r} - \frac{\partial p}{\partial r} = 0 \tag{4.1}$$

Therefore, in presence of a surface(convex), the maxima in the wall normal pressure profile will shift away from the surface. This will induce an additional region of spanwise vorticity caused by the streamwise fluctuations due to gradient in the pressure profile. These vortical structures gets further elongated as it approaches a region of larger local velocity. In order to make a comparison, the vorticity contours for R10 have been illustrated in Figure 4.12. The elongated structures seems to be more dominating for R10 supporting the hypothesis to some extent.

As already emphasized above, the shear layer on the suction side plays a major role in governing the dynamics of flow around beveled trailing edges. Therefore, the data was sampled along the core of the shear layer for the power spectral density estimation as shown by the red line in 4.13. In the figure, X_o represents the origin of the shear layer and X_s represents the line along which the data was sampled.

Figure 4.14 and 4.15 shows the power spectral density estimate of the streamwise and vertical velocity fluctuations respectively. The spectra were calculated using average periodogram method with a window size of 256 and an overlap of 50% where the coordinates X_s and X_o have been defined in Figure 4.13. The data set consisting of 5000 time steps was obtained

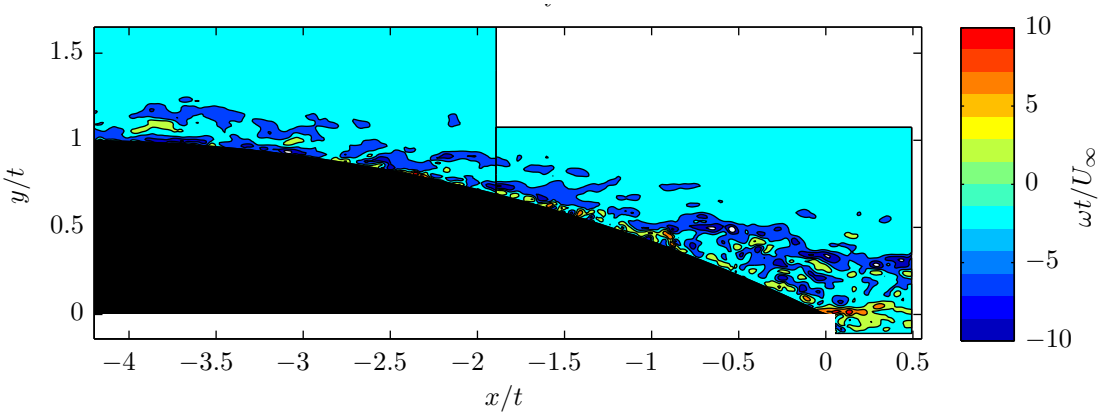

Figure 4.12: Contours of Spanwise Vortictiy ω for R10 at $Re_c = 2.68 \times 10^5$

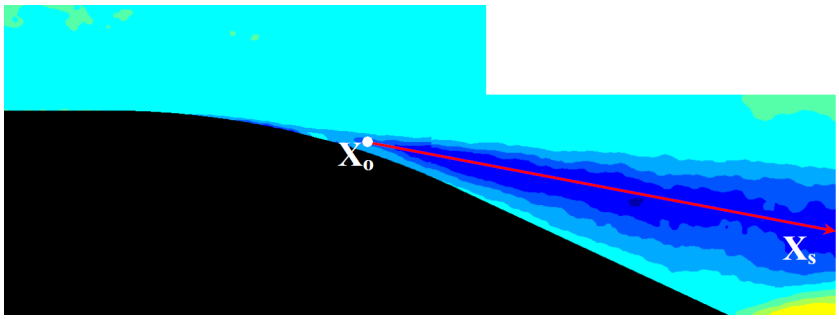

Figure 4.13: Sampling Points along shear layer for PSD estimate

using the time resolved PIV. The variables used for normalization are the freestream velocity U_∞ and the thickness t.

A broadband spectrum is observed without any dominant peaks. This is consistent with the observation of Blake (1984) and Wang and Moin (2000) where they observed broadband noise spectrum for turbulent boundary layers in combination with sharp or beveled trailing edges. A close observation of the Figure 4.14 and 4.15 shows that energy content of the small turbulent eddies decreases as we move downstream in the shear layer since the power spectral density estimate is lower in the middle frequency regime for a downstream point.

The streamwise velocity fluctuations show a higher energy content at lower frequency, likely caused by streamwise coherent regions of low speed fluid protruding from the boundary layer. On the other hand, wall-normal velocity fluctuations are associated with ejection and sweep events of smaller extent.

For wall normal velocity fluctuations, the spectra converge to approximately -18 dB for lower frequencies. The values smaller than -50 dB can be neglected for the analysis since the order of experimental error below -50 dB will be larger than the velocity fluctuations.

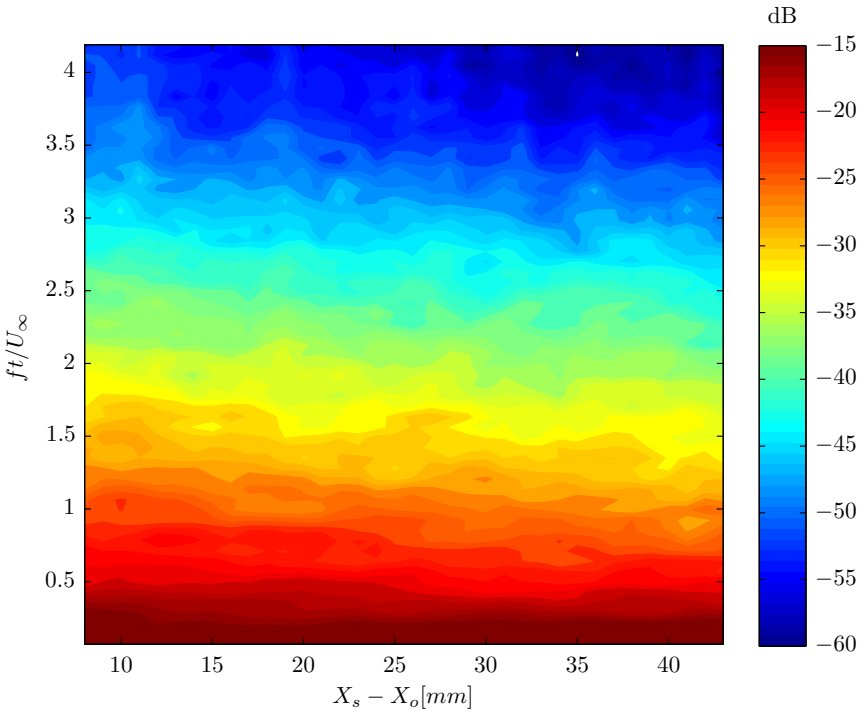

Figure 4.14: Power spectral density contours of streamwise velocity fluctuations for R4 at $Re_c = 2.68 \times 10^5$

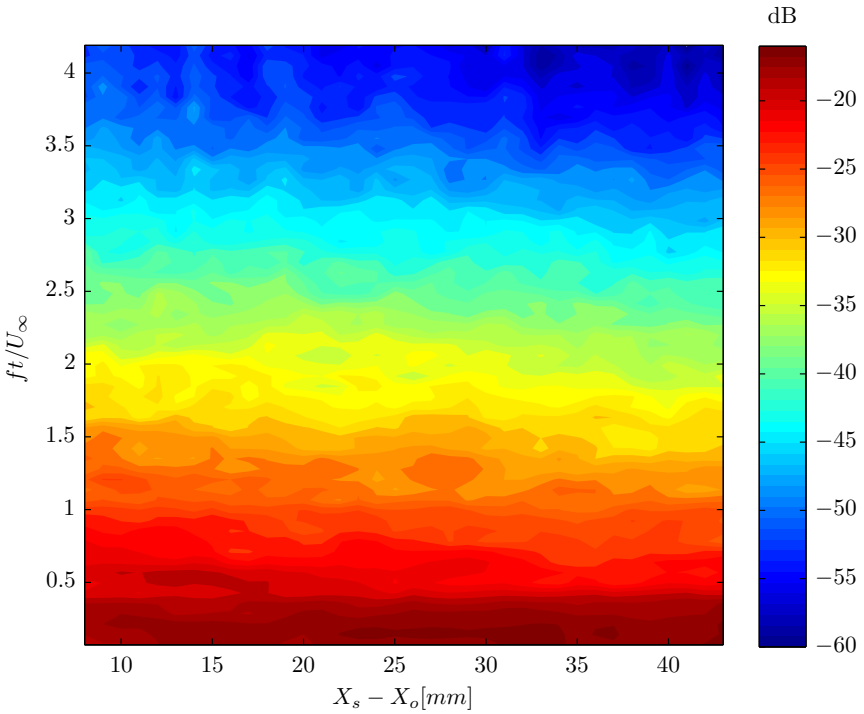

Figure 4.15: Power spectral density contours of wall normal velocity fluctuations for R4 at $Re_c = 2.68 \times 10^5$

The Power Spectral Density for specific stations has again been illustrated in 4.16 in the conventional format. The shape and spectral content corresponds to the previous studies by Blake (1984) and Wang and Moin (2000).

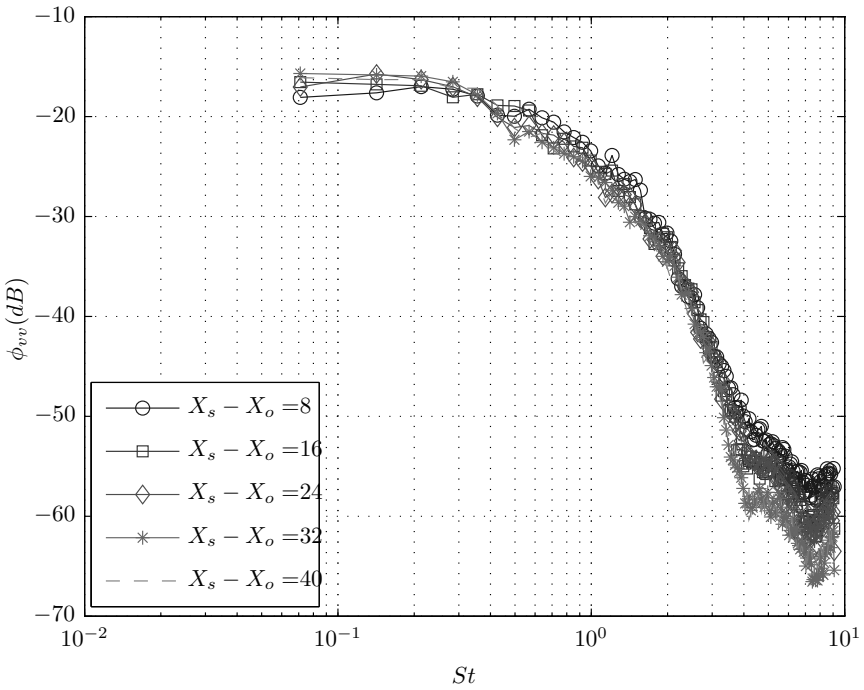

Figure 4.16: Power Spectral Density of wall normal fluctuations at 5 stations along the core of shear layer for R4 at $Re_c = 2.68 \times 10^5$

The frequency of oscillatory motions determined in the previous section can also be related to small bumps observed in the spectra around the St=1.

4.3 Aeroacoustic Sources

To compute the source terms in Ffowcs-Williams and Hall equation (Chapter 2), the velocity components U and V on the entire measurement domain were converted to cylindrical coordinate system with trailing edge as origin and sampled at every time step obtained from the time resolved PIV. The sampling resolution was $\Delta T_s = 0.1ms$.

The total record of N =5000 time samples covering a time pe n riod of half second was divided into windows with 128 samples with 50% overlap. For each segment,which contains 128 samples, the source quantities u_r^2, u_θ^2 and $2u_r u_\theta$ were computed. The aperiodic time segments are multiplied by the Hanning window function to make it periodic and than discrete Fourier transforms are performed. The resulting Fourier coefficients are renormalized such that the power spectrum computed from them, when integrated over all positive frequencies, gives the mean-square fluctuations of the original function. The resulting coefficients are than

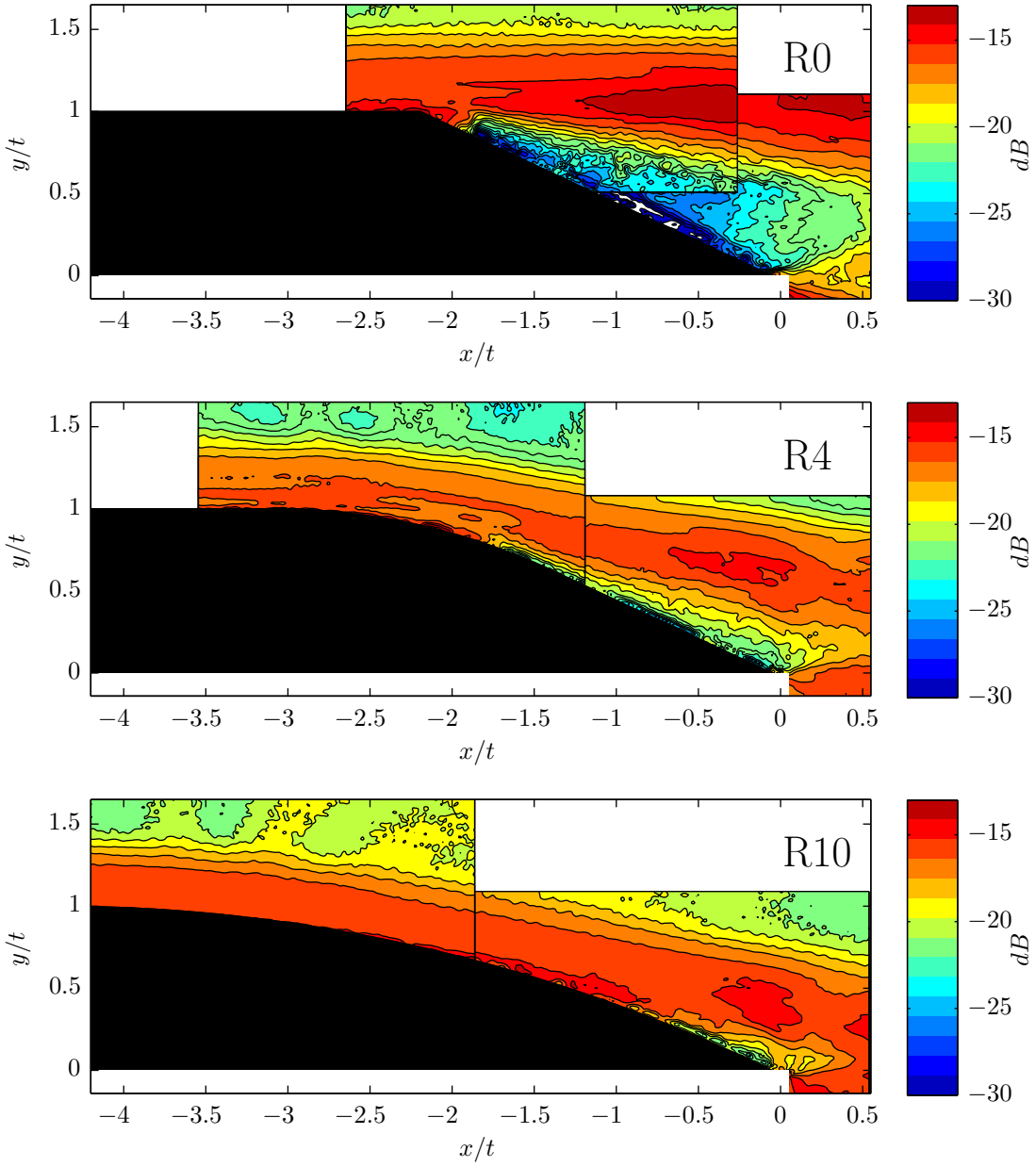

Figure 4.17: Contours for the acoustic source term at St=2 and $Re_c = 2.68 \times 10^5$

normalised with U_∞^2 to make them non dimensional and than converted to the decibel scale.

Figure 4.18 and 4.17 depicts the magnitude of the Reynolds shear-stress source term (in dB) for all three profiles at two different frequencies. The other source term i.e. u_r^2, u_θ^2 representing the normal stress behaves in a qualitatively similar manner. The assumption that acoustic wavelength should be much longer than the thickness of the model but much shorter than the chord ($t \ll \lambda_a \ll C$) puts limitation on the frequencies that can be analysed using this approach. The frequencies corresponding to $\lambda_a = C$ and $\lambda_a = t$ are given by 950Hz

(St=1.875) and 17kHz (St=34), respectively. Outside this range other appropriate Greens functions should be used. The effect of smaller chord relative to acoustic wavelength, which is severe at low frequencies, can be inferred from the analysis of Howe. Hence, the analyses is performed at St=2 and 4 corresponding to the frequency of 1 and 2kHz respectively.

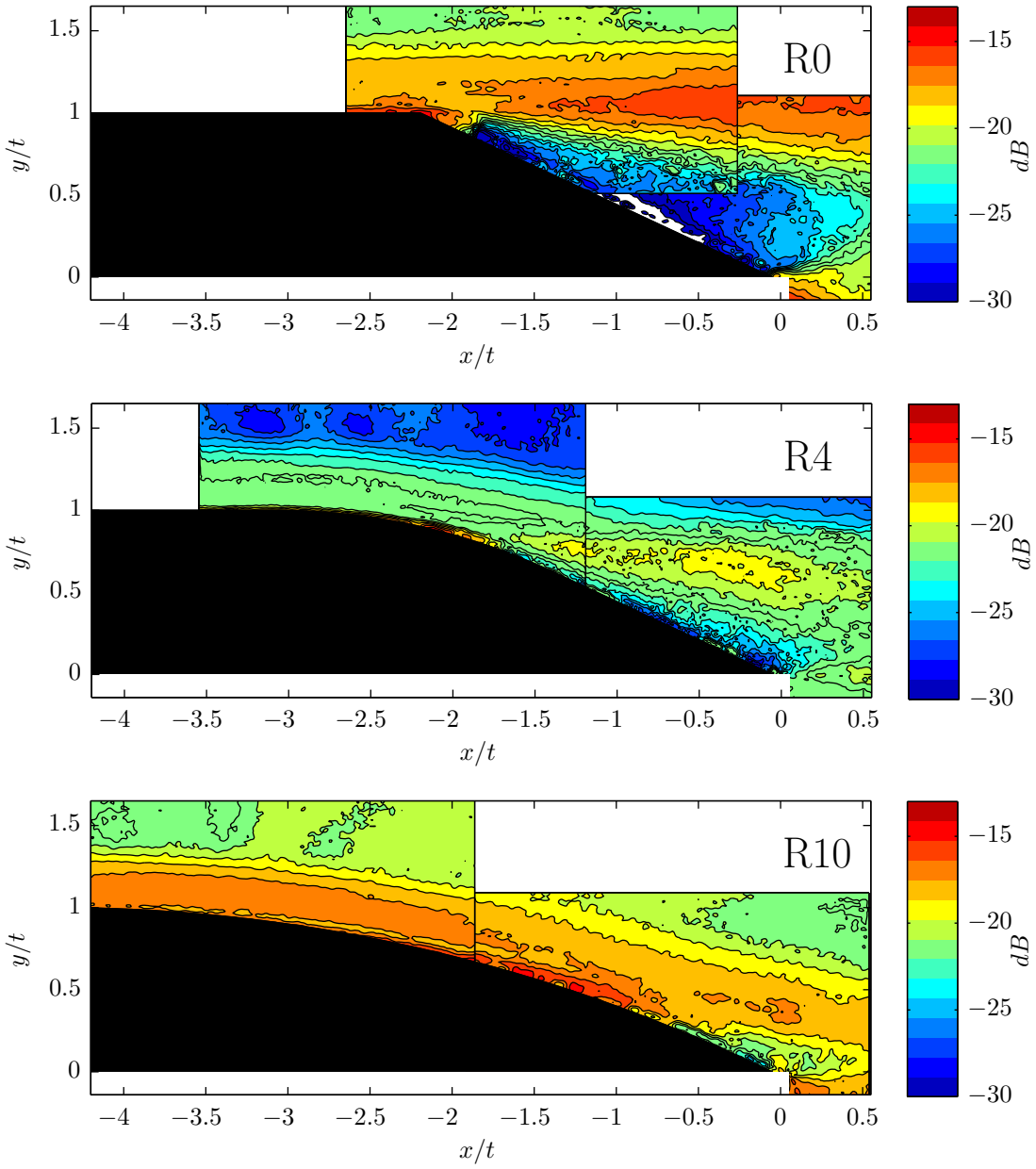

Figure 4.18: Contours for the acoustic source term at St=4 and $Re_c = 2.68 \times 10^5$

The contour lines in Figure 4.17 and 4.18 show that the spatial distribution of the acoustic source varies significantly with frequency. The source term activity decreases as we shift from R0 to R10 with R0 being the one with highest levels at lower frequencies. The low-

frequency source, associated with the large-scale unsteady flow structures, exhibits strength in a large region. The largest values are found in the shear layers emanating from the upper (separated) and lower (attached) boundary layers. As the frequency increases, the source distribution becomes more concentrated, particularly in the two shear layers. The wake region farther from the edge contributes little to the high-frequency source terms due to a lack of the corresponding small-scale flow structures. In the convolution integrals in Ffowcs-Williams and Hall Equation, the source terms shown in Figure 10 are weighted by a factor of $r_o^{-1.5}$, and, thus, the effective noise source is much more concentrated in the trailing edge region. Another interesting observation is the low levels of source term exhibited at higher frequency by R4 which represents the separated flow behaviour. This might be due the reasoning given by Howe (2000) which says that the strength of the unsteady interaction responsible for sound generation decreases exponentially due to separation with increasing frequency, and predicted levels of edge noise are significantly smaller. However, one should be very careful while using this analysis because a high level of source term do not necessarily imply high levels far field radiated sound. The sound radiation capability must be viewed in terms of convolution integral with appropriate Green function.

Chapter 5

Three Dimensional Analysis

In this chapter, the results of high-speed tomographic PIV will be discussed. First, we discuss about the configuration and location of the tomographic volumes. This is followed by a comparison of the mean flow velocity field with that obtained from planar measurements. The instantaneous results are then discussed where we made an attempt to relate the flow dynamics with the vorticity organisation. Finally, we will discuss the spanwise correlation and coherence of streamwise and wall normal velocity fluctuations and the corresponding length scales.

5.1 Measurement Volumes and Statistical Description

In recent years, the development of high-speed tomographic PIV opened new possibilities for the investigation and understanding of complex flows and aeroacoustic sources. However, for a given choice of the field of view, the light intensity is inversely proportional to the required thickness of the tomographic measurement volume (Scarano, 2013). This is a major limiting factor for tomographic measurements being scaled-up to larger volumes. In order to capture the relevant flow phenomenon while working under the limitation on measurement volume, it was decided to take measurements on four different tomographic volumes as shown in Figure 5.1, 5.2 and 5.3.

Figures 5.1 shows measurement volumes IA and IB illustrated using contours of velocity magnitude obtained from the planar PIV measurements. The reason for inclusion of volumes IA and IB was to capture the flow phenomenon around trailing edges and separation point respectively.

Figure 5.2 shows measurement volume IC illustrated using contours of Reynolds shear stresses. This volume was included to capture the flow dynamics in the shear layer.

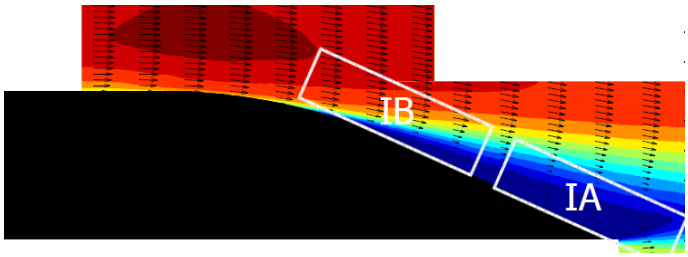

Figure 5.1: Measurement volumes IA and IB illustrated by contours of velocity magnitude at $Re_c = 2.68 \times 10^5$.

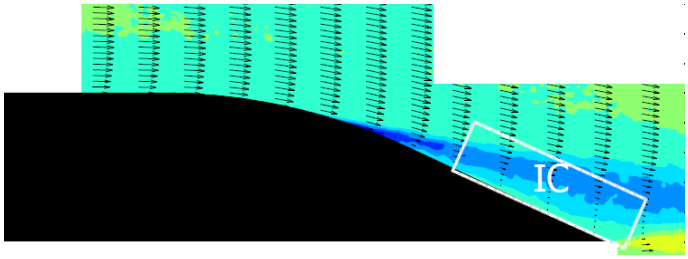

Figure 5.2: Measurement volumes IC illustrated by contours of Reynolds shear stress at $Re_c = 2.68 \times 10^5$.

Finally, Figure 5.3 shows measurement volumes II again illustrated by contours of velocity magnitude. This volume was included for the estimation of pressure field which can be obtained by solving the Poisson equation for incompressible flows.

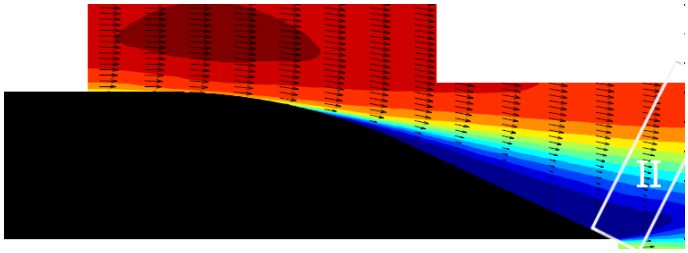

Figure 5.3: Measurement volumes IC illustrated by contours of velocity magnitude at $Re_c = 2.68 \times 10^5$.

Since the tomographic reconstruction and interrogation operations are very time consuming, the only case that was analysed as a part of this thesis was volume 1B at $Re_c = 2.68 \times 10^5$. Hence the following discussion deals only with the volume 1B of R4 configuration at $Re_c = 2.68 \times 10^5$.

The accuracy of the tomographic PIV technique was investigated by comparing the flow statistics with the planar PIV measurements. The mean velocity field obtained by averaging over an ensemble of 500 tomographic velocity fields was then averaged along the span and finally plotted in the coordinates of planar PIV as shown in Figure 5.4.

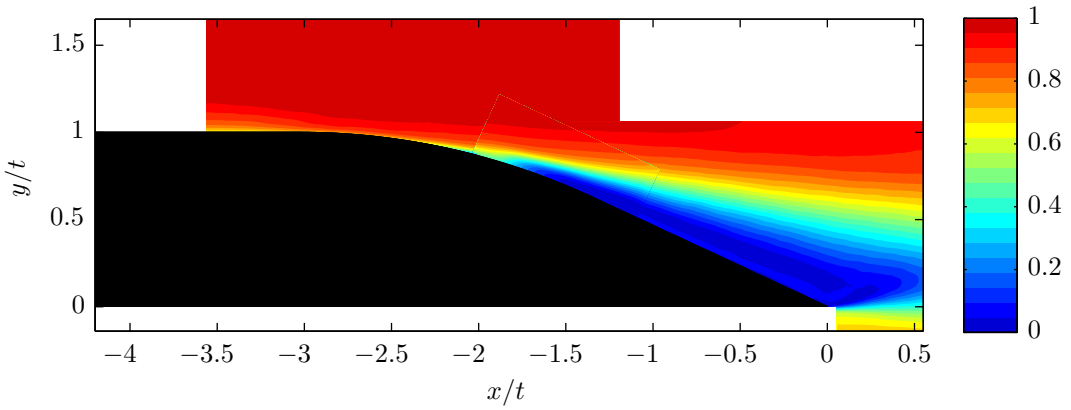

Figure 5.4: Contours of Streamwise Velocity for R4 at $Re_c = 1.34 \times 10^5$

The velocity fields obtained from tomographic and planar PIV measurements were found to be in agreement asserting the reliability of tomographic measurements.

The schematic representing the flow structure has been reproduced in Figure 5.5 along with the volume under consideration. The Figure 5.5 shows that the separation point and the shear layer are captured within the volume. The volume also captures a small region of recirculating flow in between the surface of the trailing edge and the shear layer.

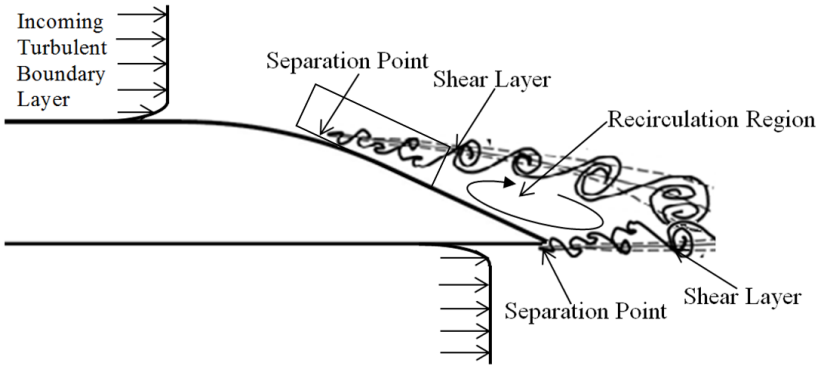

Figure 5.5: Characteristic flow features around beveled trailing edges

The understanding of the flow structure demonstrated in the Figure 5.5 will supplement the discussion on vorticity organisation presented in the next section.

5.2 Vortex Organisation and Flow Dynamics

In a turbulent flow, kinetic energy from the free-stream flow is converted into turbulent fluctuations and then dissipated into internal energy by viscous action. This process is continual, such that the turbulent boundary layer is self-sustaining in the absence of strong stabilizing

effects. For as long as these facts have been known, fluid dynamicists have sought to understand just how boundary-layer turbulence is generated at the expense of the mean motion, and just how it is dissipated.

Since it is apparently the coherent motions or structures that are actually responsible for the maintenance (production and dissipation) of turbulence in a boundary layer, the study of these structure is of fundamental importance to the understanding of flow dynamics.

The definitions of the coherent structures reported in literature always exhibits some sort of ambiguity from each other. For the present discussion, we will will stick to the definition given by Robinson (1991). According to Robinson (1991),

A coherent motion is a three-dimensional region of the flow over which at least one fundamental flow variable (velocity component, density, temperature, etc.) exhibits significant correlation with itself or with another variable over a range of space and/or time that is significantly larger than the smallest local scales of the flow.

The objective of the section is to characterise these coherent structures using high-speed tomographic PIV. The data presented in this section was obtained by the tomographic measurements followed by the correlation using FTC (Fluid trajectory correlation) algorithm. The data obtained from the correlation algorithm was visualized using Tecplot.

The flow topology is illustrated in Figure 5.6 by the contours of spanwise vorticity on 4 different X-Y planes and surfaces of constant Q factor, which show the level of vorticity and the length scales of the turbulent structures in the flow. The iso-surfaces of Q factor are color coded with the spanwise vorticity. The gray surface represents the trailing edge geometry (R4) under consideration. The visualization has been made in the coordinates used for planar PIV with z-axis along the spanwise dimension.

Figure 5.7 illustrates the instantaneous flow Visualization using iso-surfaces of Q, color coded with spanwise vorticity from a side (X-Y) view. The separation essentially creates three different flow regimes within the volume. The first is the flow in left upper region which encapsulates the separated boundary layer. A streamwise elongated and tilted green color structure can be observed in the Figure 5.7 which lies in this region. The green color represents low levels of spanwise vorticity. The second is the recirculation region in the lower left section of the volume. The third and perhaps the most interesting is the region of high spanwise vorticity formed due to the interaction between the first two flow regimes. Several blue coloured structures representing large spanwise vorticity can be identified in this region.

The first type of structures identified above are the incomplete hairpin vortices and the second are the Kelvin Helmholtz billows found along the shear layer. We will discuss both of them one by one in the following discussion.

Theodorsen (1952) proposed the hairpin vortex model for boundary layer turbulence production and dissipation that was developed from the vorticity-transport form of the Navier-Stokes equations. In this model, hairpin shaped vortical structures were predicted to grow outward with heads inclined downstream at 45 deg.

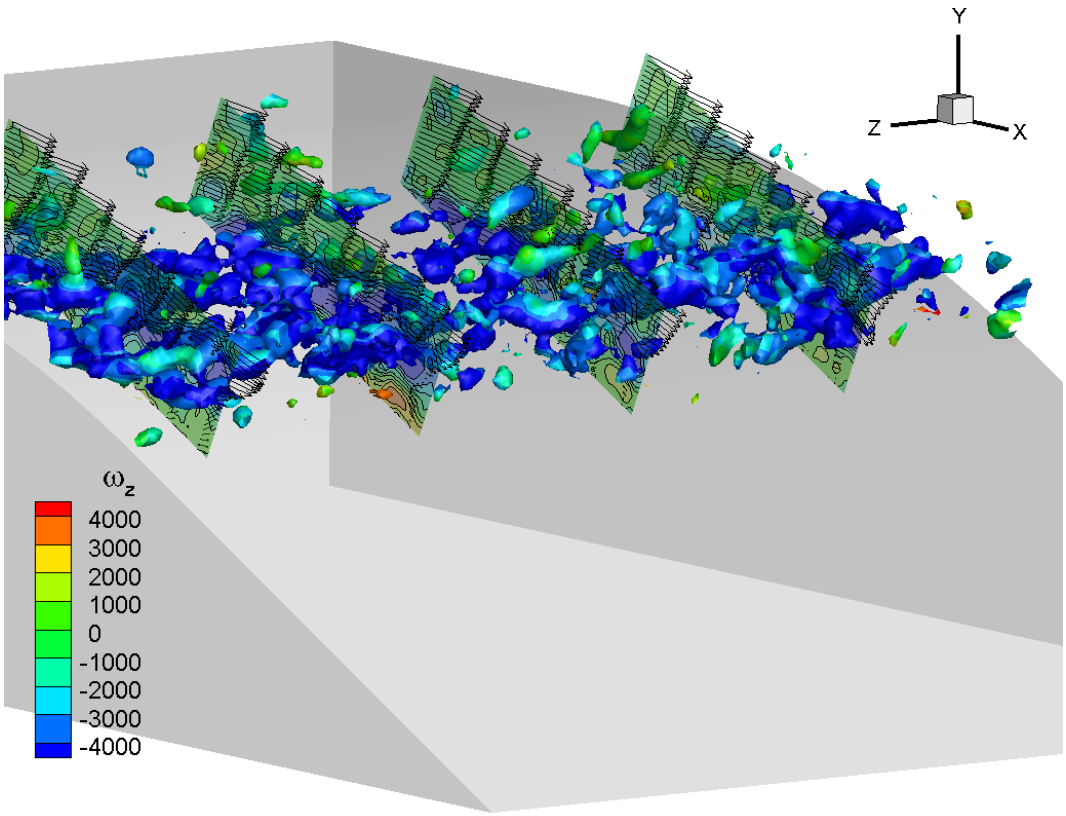

Figure 5.6: Flow topology illustrated by iso-contours of Z voticity and iso-surfaces of Q color coded with Z vorticity

Theodorsen's model was proposed as an instantaneous description of nearwall turbulence dynamics. Figure 5.8 shows a schematic of these hairpin vortices. Hairpin vortices owe their name to the shape which becomes apparent under suitable visualisation methods.

Willmarth and Tu (1967) used space-time correlations between the wall pressure and all three velocity components near the wall to devise a model for the average eddy structure of the near-wall region. They suggested that near-wall hairpin vortices may evolve to a larger scale, producing the intermittent bulges in the outer edge of the boundary layer and thus providing an outward interaction mechanism between the inner and outer regions. Cane vortices are incomplete, broken or asymmetric hairpins with or without head.

Figure 5.9 shows another visualization using iso-surfaces of Q. The structures are again color coded with spanwise vorticity but the voriticity scaling is changes so that the structures with large and small spanwise vorticity are represented by blue and red colors respectively. The Figure 5.9 indicate that vast amount of structures are the cane vortices identified by red color iso-surfaces. The origin of these structures lies in the boundary layer before the separation. The fact that the hairpin vortices cannot be identified in the interrogation volume does not

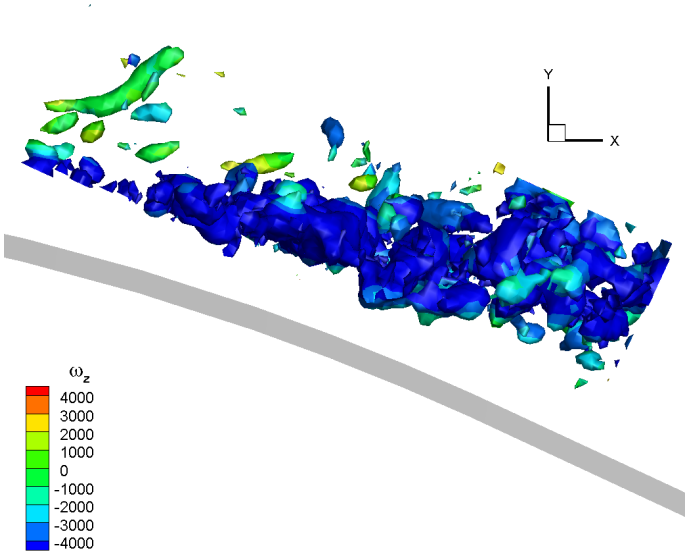

Figure 5.7: Instantaneous flow Visualization using iso-surfaces of Q (Side view)

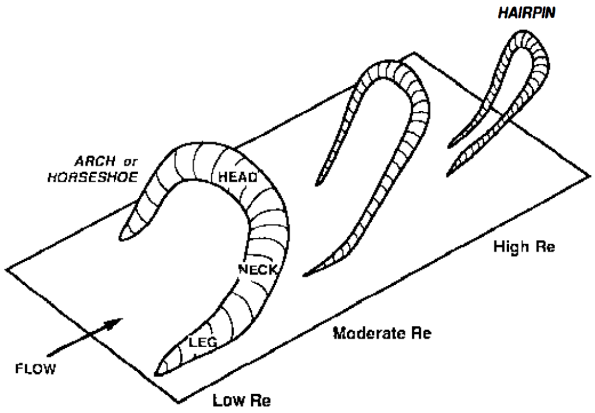

Figure 5.8: Geometry and nomenclature for arch- and hairpin-shaped vortical structures (Theodorsen, 1952)

mean that they do not exist. Generally, the large canes visualised in the figure belong to large hairpin vortices of a scale exceeding the height of the measurement region. Furthermore, hairpins might exist at scales smaller than the ones visible in the reconstruction or closer to the surface.

Parameters of interest describing these structures are their typical dimensions, inclination with respect to the wall. Inclination of the structures with respect to the wall can be observed to be about 45 deg or slightly larger while their length is of the order of 0.3 times the thickness parameter (see Figure 5.9 and 5.7).

As expected from the distribution of Reynolds stresses, the region in between mean flow and separated flow shows higher values of Q and appears to be more populated with struc-

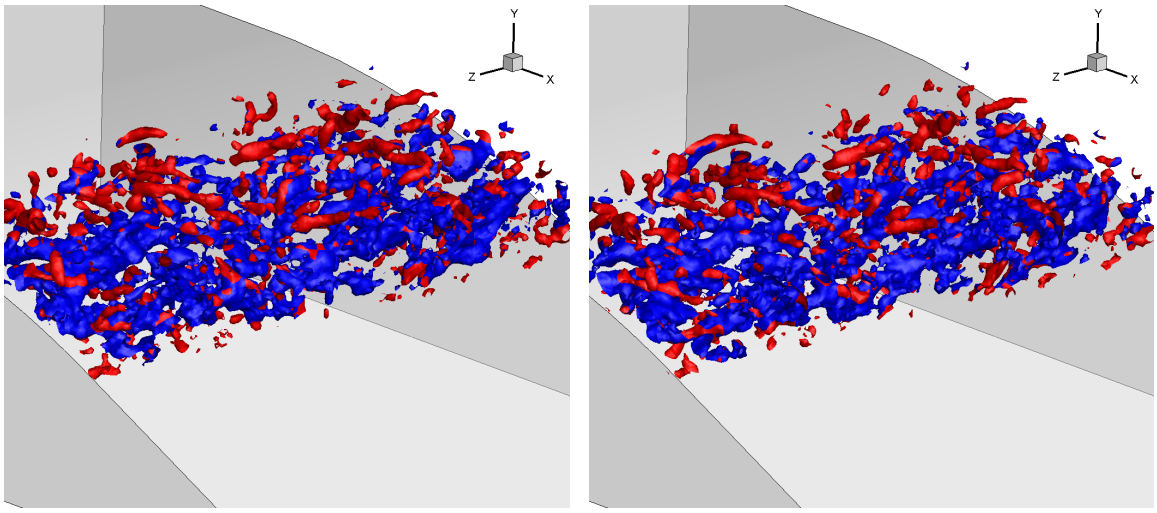

(a) (b)

Figure 5.9: Incomplete hairpin vortices visualised by isosurface of Q at two consecutive time instants.

tures of relatively long spanwise coherence. It is proposed that these coherent vortices are of the Kelvin Helmholtz type existing in the shear layer. These vortices results from a Kelvin Helmholtz instability to which are superimposed 3D perturbations resulting from the turbulent field. Figure 5.10 shows examples for the development of these coherent structures in the interrogation volume over time. The iso-surfaces in Figure 5.10 show the quasi-2D rollers. Deviation from two-dimensionality is evident from the iso-surfaces in several sections along the span. Their average local longitudinal wavelength λ is of the order of 0.4 times the thickness parameter t.

Evolution of the rollers in plane mixing layers has been the subject of many studies. Small spanwise perturbations on the rollers such as translative, bulging, and helical have been shown to be amplified during pairing (Estevadeordal and Kleis, 1999). Local perturbations have been shown to produce vortex phenomena such as bridging, branching, and dislocations (Estevadeordal and Kleis, 1999). Some spanwise areas exhibit a more advanced pairing stage than others, producing branched vortex patterns (Lesieur, 2008). Some branched spanwise vortices can be observed in Figure 5.10. However, it is not possible to follow their evolution due to a larger $\delta T = 100\mu s$ compared to the time scales of the flow.

The source of energy for generating the Kelvin Helmholtz instability is derived from the kinetic energy of the shear flow. The disturbances essentially smear out the gradients until they cannot grow any longer. The vortex sheet made up of the KH billows is always unstable to all wavelengths. It is also seen that the unstable wave moves with a phase velocity equal to the average velocity of the basic flow (Lesieur, 2008). This is consistent with the observation of Blake (1984) where he observed that the convection velocity of disturbances is of the same order as the measured local mean velocity.

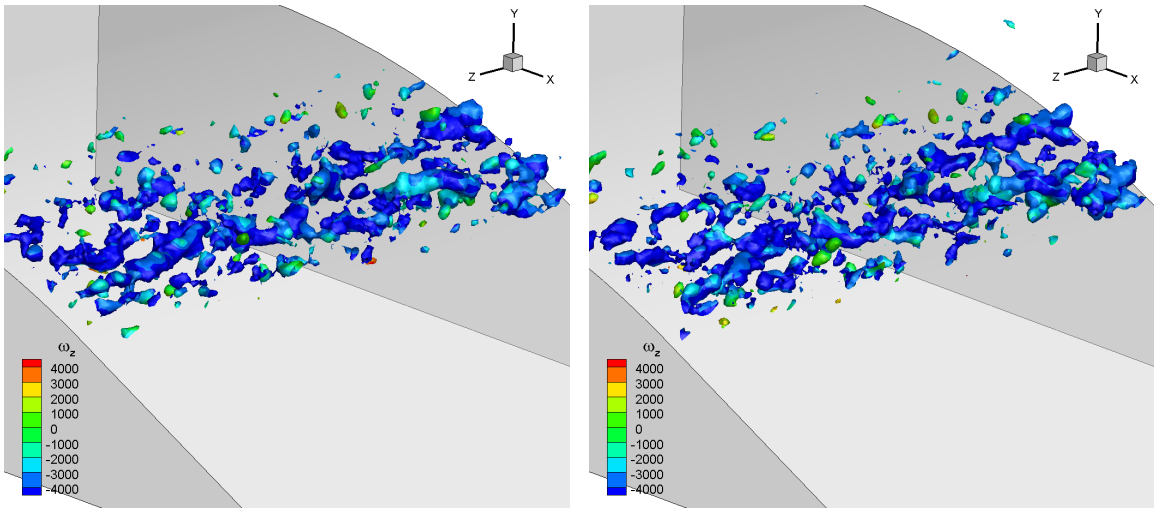

(a) $\delta T = 0$ (b) $\delta T = 100\mu s$

Figure 5.10: Visualization of KH instablity using isosurface of Q.

5.3 Correlation and Coherence

Far field pressure can be related to the fluctuating pressure field on the surface of the airfoil (Amiet, 1976). In analytical models (Howe, 1978), it is usually assumed that the pressure field on the surface can be described using turbulent quantities like the spanwise coherence length scale l_z. An experimental quantification of the l_z would allow predicting and assessing the noise reduction potential. The hydrodynamic surface pressures generated by these turbulent motions can be related through Poisson's equation. Hence, we will work under the premise that spanwise coherence length scale l_z based on velocity fluctuations can be used to describe far field pressure spectrum.

The work focuses on the applicability of tomographic PIV to compute the correlation coherence of velocity fluctuations and acoustic source term, with attention to the estimation of the spanwise coherence.

Data used in this section has been acquired with the experimental set-up described in Chapter 2.2 recording 5000 samples at a rate of 10kHz. The total record of N =5000 time samples covering a time period of half second was divided into windows with 96 samples with 50% overlap. For each segment, which contains 96 samples, the velocity fluctuations and the source quantities were computed. The spectra has been computed using Welch's method described in Section 2.3.

For the rest of the analysis, data is sampled along the centre of shear layer as illustrated in Figure 5.11 where the black rectangle represents the spanwise cross section of measurement volume. As discussed in the previous section, X_o represents the origin of the shear layer and

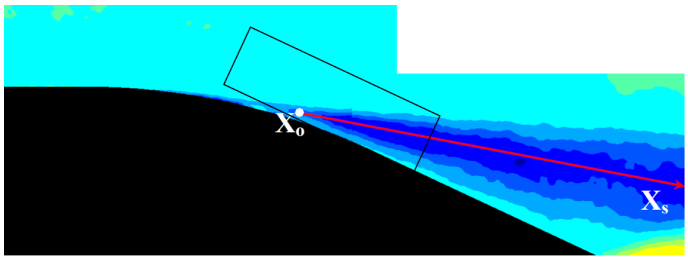

Figure 5.11: Sampling Points along shear layer for PSD estimate

X_S represents the coordinate as we move along the core of the shear layer. In the subsequent discussion, streamwise refers to the wall tangential coordinate X_T and wall normal refers to X_N as discussed in Section 3.2 .

5.3.1 Correlation

Physically, the correlation with separation Δz is a measure of the similarity for eddies whose length along the z direction is greater than the magnitude of Δz since eddies smaller than this will not contribute to the correlation. When we speak of the length scale of the energy containing eddies we mean a length of order equal to the correlation length. However, this is an imprecise concept in the sense that we are ignoring the frequency content corresponding to each length scale. Infact, it is more instructive to look into these length scales in the frequency domain which has been discussed in the next subsection.

Figure 5.12 and 5.13 shows the results for the correlation coefficient for wall normal and streamwise fluctuations respectively as a function of shift in spanwise direction. The general trend is an increase in correlation coefficient in downstream direction. This can be due to the pairing of the spanwise rollers.

For wall normal velocity fluctuations, the change in correlation coefficient increases as we move downstream while it decreases for streamwise velocity fluctuations. The coherence length corresponding to streamwise velocity fluctuations shows larger values as compared to the coherence length for wall normal fluctuations.

The spanwise integral length scale can be determined by means of the correlation coefficient of the velocity fluctuation along a line in spanwise direction. The results of the correlation length has been tabulated in Table 5.1 and 5.2.

The correlation coefficient becomes zero for a shift equal to half of the thickness of the model and the values of correlation length are of the order of 2mm.

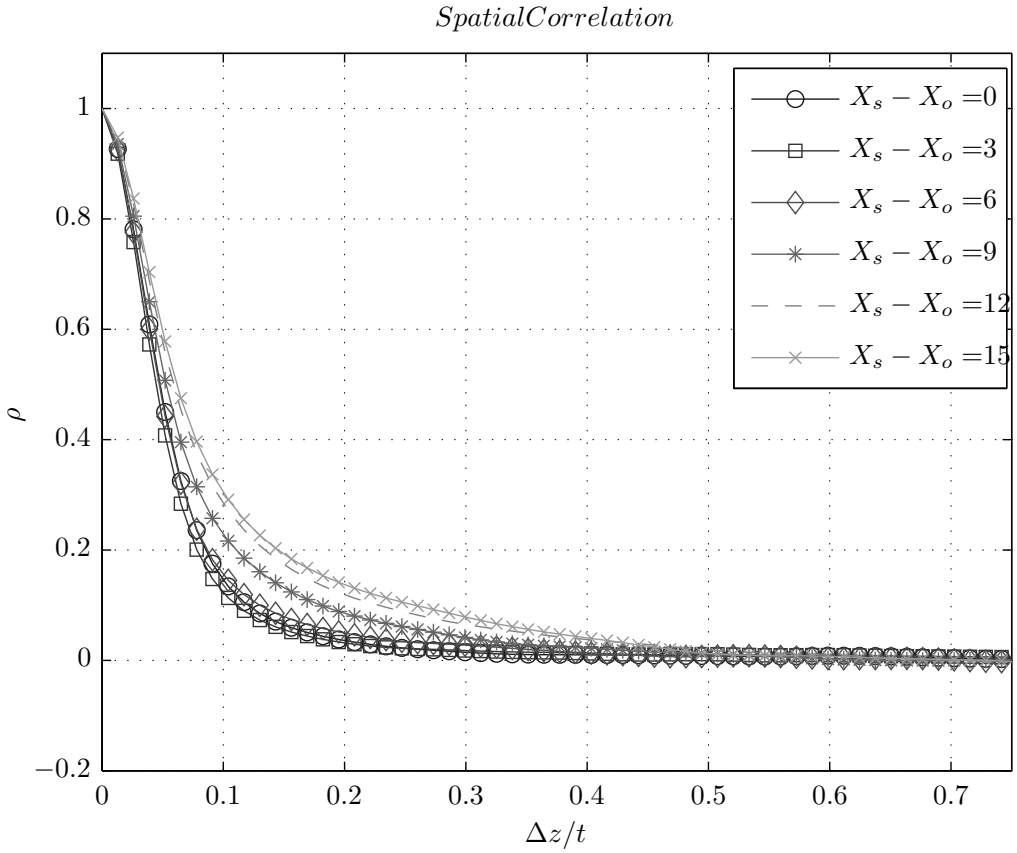

Figure 5.12: Spanwise spatial correlation coefficient for wall normal velocity fluctuations

5.3.2 Coherence

The analysis of the correlation coefficient gives an overall frequency independent view of the trailing edge physics. A more detailed analysis can be made by computing the coherence function γ^2 as a function of frequency and spanwise separation. The present section analyses the results for spanwise coherence of wall normal velocity fluctuations, streamwise velocity fluctuations and the source terms. The white horizontal line in the plots corresponds to the smallest window size used during the image processing below which the length scales are not resolved properly.

Figure 5.14 and 5.15 shows the spanwise coherence of streamwise and wall normal velocity fluctuations respectively as we move downstream along the core of the shear layer. In general, three ranges for Strouhal number can be identified:

1. $0 < St < 0.5$ - low frequency range: highly coherent structures with large coherence length. The coherence decays slowly with increasing separation and frequency,

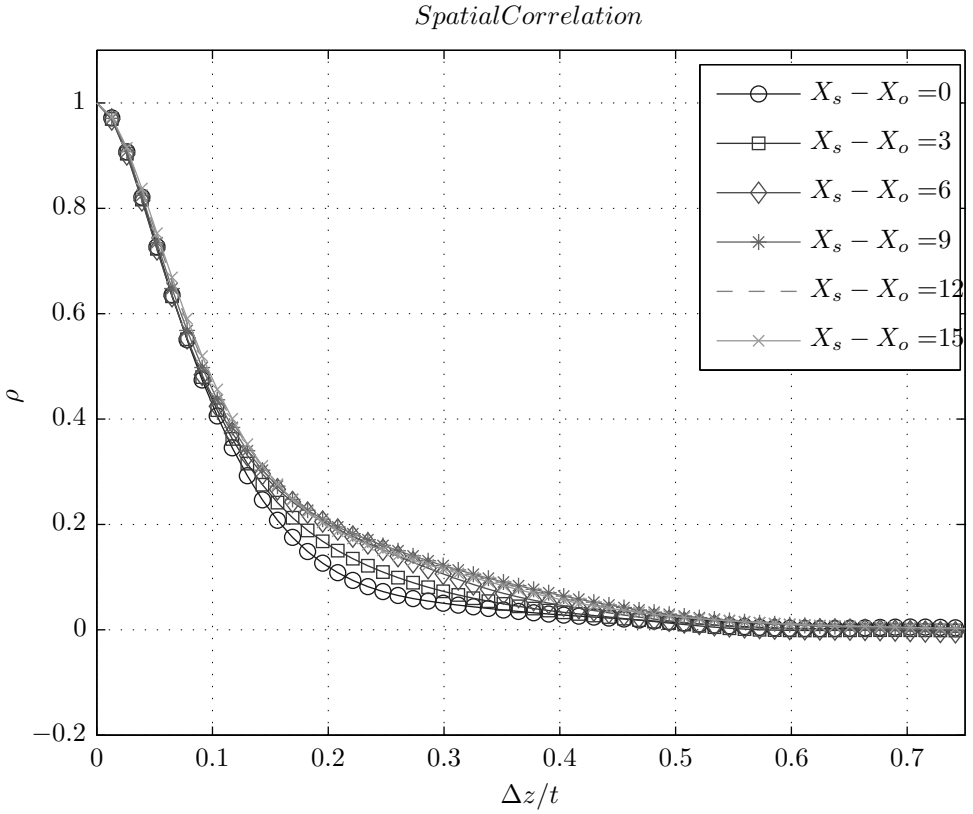

Figure 5.13: Spanwise spatial correlation coefficient for streamwise velocity fluctuations

2. $0.5 < St < 2$ - mid frequency range: the structures are less coherent, large values for wall normal fluctuations in downstream direction,

3. $St > 2$ - high frequency range: The coherence is almost frequency independent, but the coherence decreases rapidly with the spanwise separation.

Figure 5.14 shows large coherence at lower frequencies for all positions. For a Strouhal number of upto 0.2, the spatial coherence does not drops to zero even for a length scale of 0.25 times the thickness t. This is also evident in the contours of coherence length in Figure 5.16. As we move downstream, the coherence at larger frequencies decreases. A wavy pattern is observed for variation of coherence with frequencies which dampens out with distance from X_o. In general the coherence length is larger in upstream positions. The low frequency range coherence suggests the presence of large eddies occurring mainly around 100 Hz. Eddies associated to the mid-frequency range have a span wise extent of about 1 mm in the experiment.

The coherence for wall normal velocity fluctuations exhibits smaller length scales as compared to the streamwise fluctuations. A peak was observed as move downstream around St=0.6 which corresponds to the frequency of 300 Hz. Note that the oscillations of same frequency were observed in the planar analyses performed in the previous chapter. This phenomenon can also be observed in the plot of coherence length for wall normal velocity fluctuations which

Table 5.1: Spanwise correlation length corresponding to wall normal velocity fluctuations

$X_s - X_o[mm]$	Correlation Length (L_ρ)
0	1.3mm
3	1.19mm
6	1.33mm
9	1.58mm
12	1.85mm
15	1.94mm

Table 5.2: Spanwise correlation length corresponding to streamwise velocity fluctuations

$X_s - X_o[mm]$	Correlation Length (L_ρ)
0	2.15mm
3	2.02mm
6	2.14mm
9	2.37mm
12	2.47mm
15	2.41mm

shows quite large values in the downstream region around St=0.6. The trend of correlation as well as coherence suggests a shift in energy from streamwise to wall normal fluctuations. The more rapid loss in coherence for wall normal fluctuations might be explained with the arrangement of the measurement volume. The wall normal component is out of the plane component which implies an unfavourable condition for the measurement of the wall-normal velocity and therefore a larger random error.

The value of source coherence plotted on the same format have been shown in Figure 5.17. The source term was obtained by converting the velocity fluctuations in radial coordinates with origin at trailing edge. Then Welch's algorithm is used again for spectral estimation. The coherence coefficient ceases to drop to zero at lower frequencies, indicating zones of high spanwise coherence. The spanwise coherence is proportional to the emitted sound power. The spanwise source coherence falls below 20% at the spanwise separation of $0.1t$ which gives an order of magnitude of the spanwise wavelength of the process.

The coherence of source terms is also useful in determining the minimum size of the measurement domain for far field noise estimation. In a typical tomographic PIV measurement, the spanwise width L of the measurement domain is only a small fraction of the actual span L_o. For example, $L_o/L = 8$ for the present configuration with $L \approx 50mm$ and $L_o = 400mm$.

To predict the frequency spectrum of the sound pressure radiated from the entire span, one requires knowledge about the spanwise coherence of the source field. If $l_z(\omega)$ denote the coherence length for a given frequency, two limiting cases can be found (Wang and Moin, 2000)

(a) If $L \geqslant l_z(\omega)$, source regions radiate in a statistically independently manner. Hence, the total noise spectrum is the sum of contributions from L_o/L independent source regions along

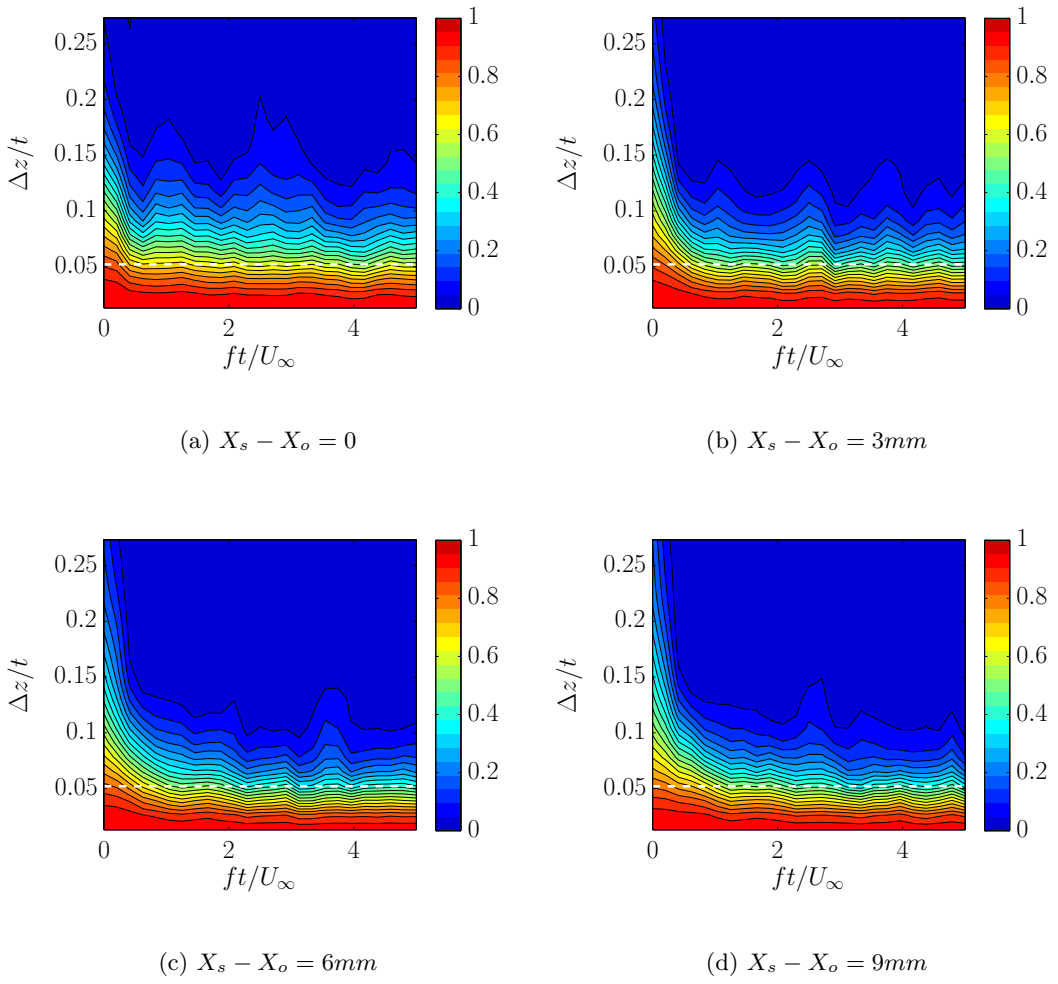

(a) $X_s - X_o = 0$

(b) $X_s - X_o = 3mm$

(c) $X_s - X_o = 6mm$

(d) $X_s - X_o = 9mm$

Figure 5.14: Spanwise Coherence of streamwise velocity fluctuations along the core of shear layer.

the span.

(b) If $L_o \leqslant l_z(\omega)$, the source is coherent along the entire span i.e. the source can be assumed to be two dimensional.

In the intermediate region $L < l_z(\omega) < L_o$ an accurate prediction of the total sound pressure is difficult to achieve. The measurement domain is too small to accommodate the spanwise flow scales, and thus the acoustic source functions are not computed reliably. The rigorous remedy is to increase the measurement domain size L along the span so that case a or b described above applies. This is, however, often prohibitively expensive. Kato (1993) resorted to an ad hoc approach in which z is approximated by extrapolating from the slowly-decaying coherence function, and a hybrid formula based on cases a and b is used to estimate the noise radiation. Figure 5.18 shows the coherence length of source terms. At lower frequencies and

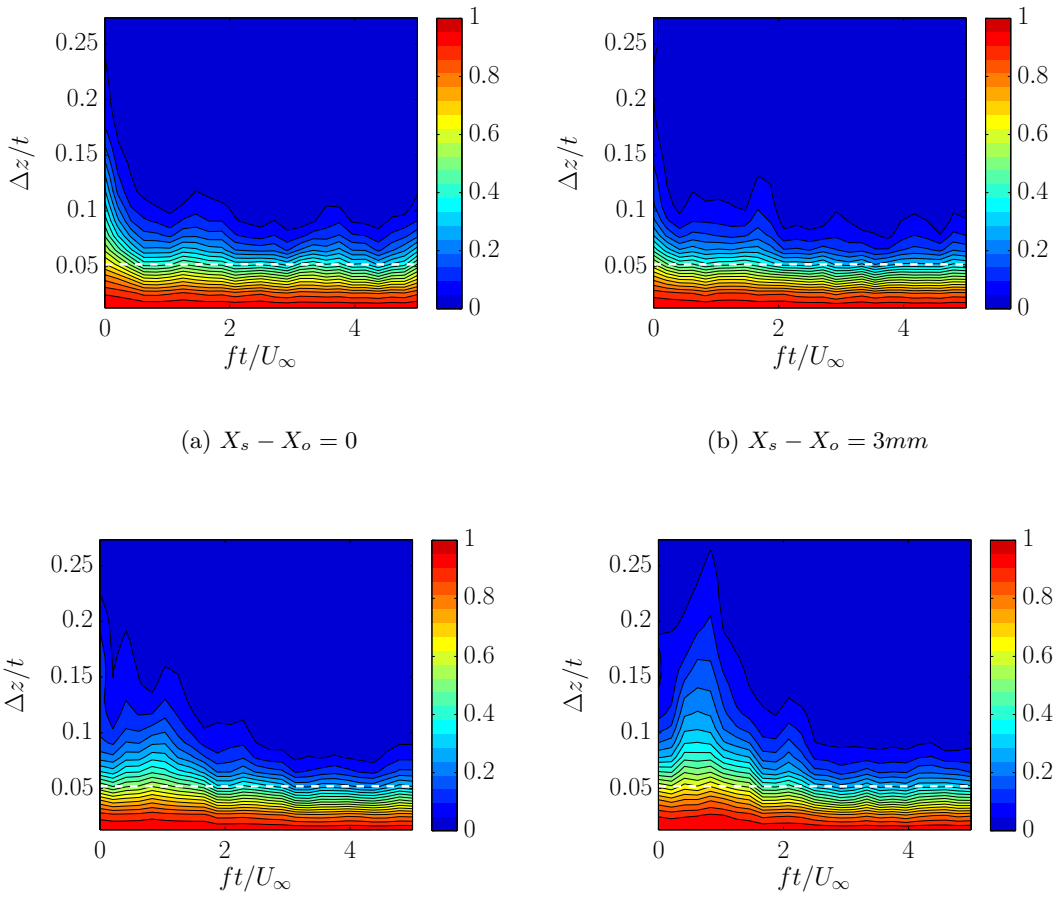

(a) $X_s - X_o = 0$

(b) $X_s - X_o = 3mm$

(c) $X_s - X_o = 6mm$

(d) $X_s - X_o = 9mm$

Figure 5.15: Spanwise Coherence of wall normal velocity fluctuations along the core of shear layer.

smaller distance from X_o, the value of coherence length is around 3mm. This is somewhat an incorrect estimate of the coherence length at lower frequencies and the actual values can be much higher because the coherence does not decay to zero within the considered spanwise separation. However, the assumption of $(t \ll \lambda_a \ll C)$ is not valid for such lower frequencies. This suggests that Ffowcs-Williams and Hall's analogy might under predict the far field noise by not considering the possible large contributions at lower frequencies. For larger frequencies, the coherence length is significantly smaller than the measurement domain and the analogy can be applied considering that source regions are radiating in a statistically independently manner along span.

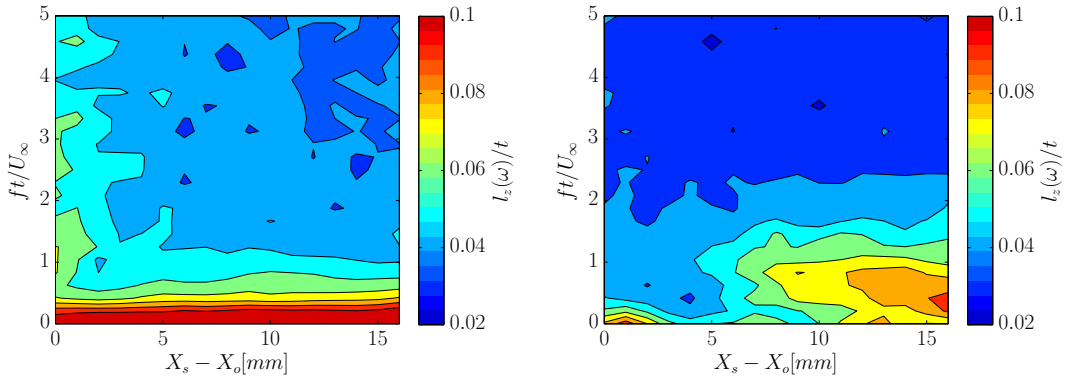

(a) Streamwise fluctuations

(b) Wall normal fluctuations

Figure 5.16: Coherence length estimated along the core of shear layer for velocity fluctuations.

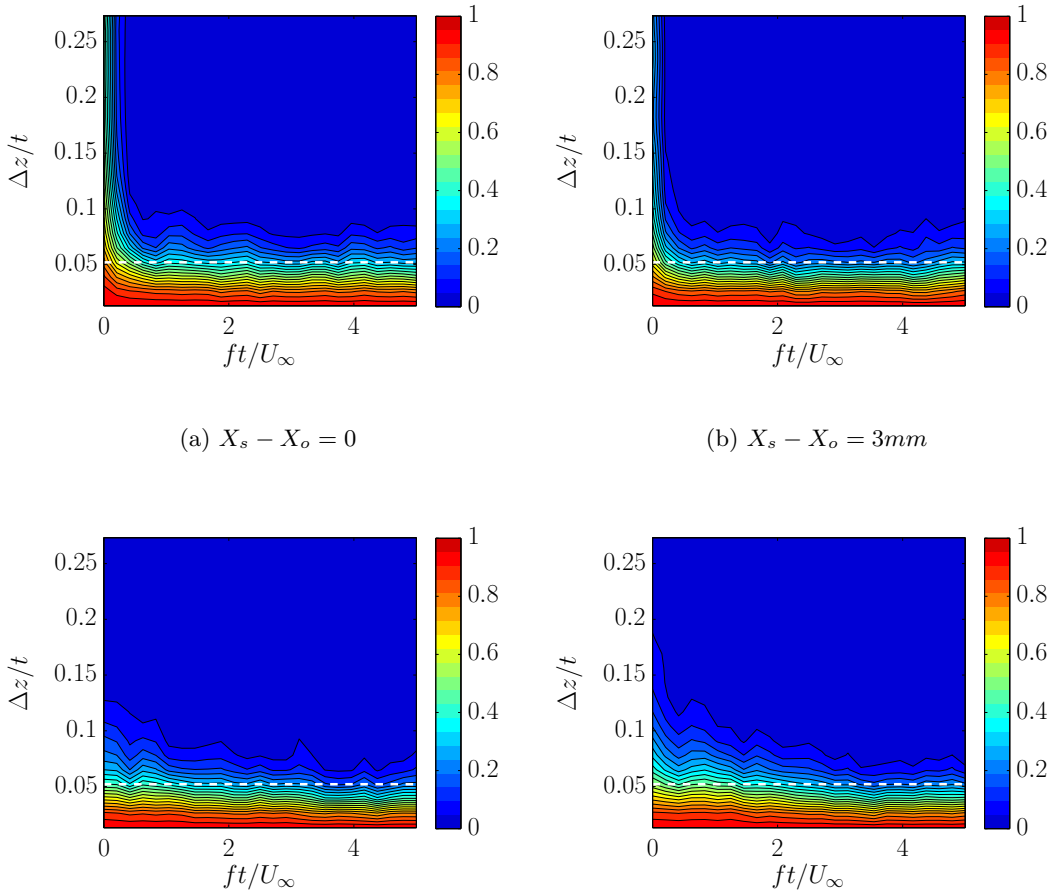

(a) $X_s - X_o = 0$

(b) $X_s - X_o = 3mm$

(c) $X_s - X_o = 6mm$

(d) $X_s - X_o = 9mm$

Figure 5.17: Spanwise Coherence of source term along the core of shear layer.

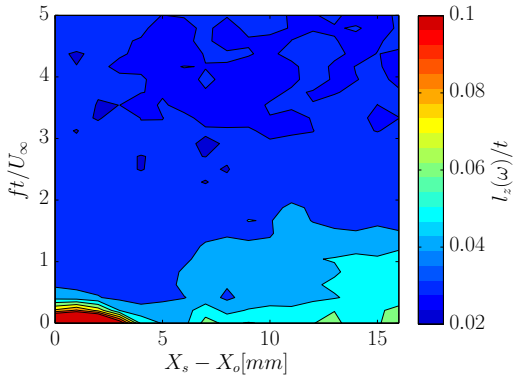

Figure 5.18: Coherence length estimated along the core of shear layer for source terms

Chapter 6

Conclusion

Aeroacoustic investigation of flow around a beveled trailing edge was performed using high-speed particle image velocimetry. Velocity fields were obtained with high temporal and spatial resolution. Advanced image interrogation including sliding average correlation and fluid trajectory correlation were implemented for the analysis of PIV images. A statistical analysis was done to identify the flow structure around beveled trailing edges. Transition from laminar to turbulent flow was observed at $Re_c = 1.82 \times 10^5$. For R4 profile at $Re_c = 2.68 \times 10^5$, the boundary layer on the suction side separates upstream of the trailing edge, while the boundary layer on the pressure side separates at the sharp edge. The separation point at the suction side moves downstream with increasing Reynolds number and radius of curvature. Separation was not observed for R10 at the same Reynolds number due to the less intense adverse pressure gradient caused by larger surface curvature.

The velocity fields obtained from the high-speed measurements were used to calculate the power spectral density of velocity fluctuations. A broadband spectrum was observed. Instantaneous flow visualization suggested a dominant frequency of f=333Hz representing the dominant frequency of the oscillatory vortical motions in the upper shear layer. Ffowcs-Williams and Hall's acoustic analogy was implemented to evaluate activity of potential sound sources around trailing edges.

The velocity fields obtained from tomographic PIV were compared to the results of planar PIV. A good agreement was observed between the results obtained from the two techniques. For the visualization of vortical structures in the flow, the Q-criterion was used and applied to the velocity data which was obtained by tomographic PIV. Coherent structures were observed relatively close to the separation point. The structures with origin in the boundary layer upstream of the trailing-edge appearing in the form of canes (incomplete or asymmetric hairpin structures) were observed. Large coherent structures appearing downstream of the separation point with high vorticity level were identified. Most of these structures showed a relatively large spanwise coherence and were associated with the Kelvin Helmholtz instability. Finally, the behaviour of spatial correlation and coherence along spanwise direction was

analysed along the core shear layer and the corresponding length scales were evaluated. The integral length scales obtained using the correlation coefficient were of the order of 2mm. The coherence of wall normal velocity fluctuations also exhibit larger larger values around 333 Hz which was observed as the dominant frequency in the upper shear layer. The coherence length of source term was observed to be significantly smaller than the measurement domain implying that the Ffowcs-Williams and Hall's analogy can be applied considering that various source regions are radiating in a statistically independently manner along span.

The analysis of aeroacoustic analysis of beveled trailing edges using HS-PIV was able to predict the source activity of the acoustic field qualitatively. The dominant frequencies and coherent structures were captured as well as the trend of the broad-band noise. The acoustic emissions largely depends on flow structure and the flow structure in turn depends on the geometrical parameters (θ, R/t) and the flow parameters (Re). Hence, an experimental determination of the flow structure allows assessing the noise reduction potential.

The potential of further research in the aeroacoustic investigation of trailing edge flow is tremendous. At this point, the author would like to emphasize the fact that less than a quarter of the data acquired during the experimental campaign was analysed as a part of this thesis. Some recommendations for further investigation in continuation of the current project have been listed below:

1. **Pressure reconstruction and far field noise estimation** The velocity fields obtained from the volume II of the present experimental campaign can be used to calculate the unsteady pressure field by means of a Poisson solver. The obtained pressure can be used to estimate the far field noise using Amiet's diffraction theory (Amiet, 1976).
2. **Implementation of pattern recognition techniques** Pattern recognition algorithms can be applied for characterization of structures using tomographic PIV as already illustrated by Ghaemi and Scarano (2011).
3. **Larger spatial and temporal resolution** A higher spatial and temporal resolution can go a long way in resolving small scale fluctuations and improving our understanding of the flow dynamics and aeroacoustic behaviour. With continuing breakthroughs in high-speed camera and laser technologies, this line of action is feasible. The improvement in spatial resolution of digital cameras will also aid in capturing the smaller scale vortices, which are highly correlated to pressure fluctuations, thus improving pressure evaluation. Another alternative is to use the the use of a vortex-in-cell (VIC) inviscid, incompressible Navier-Stokes solver to increase temporal resolution of time-resolved 3D fluid-velocity data obtained from tomographic PIV experiments (Schneiders et al., 2013).
4. **Investigation of** 45 deg **beveled trailing edge** The present work was focused on 25 deg beveled trailing edge. It might be interesting to perform the similar analysis using tomographic PIV on the 45 deg beveled trailing edge which exhibits large scale vortex shedding linked to tonal noise.

The present investigation, in the limits of the experimental conditions, revealed that experimental approaches are suitable for aeroacoustic predictions. The continuous improvements of

the experimental devices for high-speed flow measurement techniques provide good prospects for developments of experimental PIV-based aeroacoustic investigations.

Bibliography

Ronald J Adrian. Twenty years of particle image velocimetry. *Experiments in Fluids*, 39(2): 159–169, 2005.

R K Amiet. Noise due to turbulent flow past a trailing edge. *Journal of Sound and Vibration*, 47(3):387–393, 1976. URL http://linkinghub.elsevier.com/retrieve/pii/0022460X76909482.

William K Blake. A statistical description of pressure and velocity fields at the trailing edges of a flat strut. Technical report, DTIC Document, 1975.

WK Blake. Trailing edge flow and aerodynamic sound. part 1. tonal pressure and velocity fluctuations. part 2. random pressure and velocity fluctuations. Technical report, DTIC Document, 1984.

TF Brooks and TH Hodgson. Trailing edge noise prediction from measured surface pressures. *Journal of Sound and Vibration*, 78(1):69–117, 1981.

DG Crighton and FG Leppington. On the scattering of aerodynamic noise. *J. Fluid Mech*, 46(3):577–597, 1971.

N Curle. The influence of solid boundaries upon aerodynamic sound. *Proceedings of the Royal Society of London. Series A. Mathematical and Physical Sciences*, 231(1187):505–514, 1955.

Lars Davidson et al. An introduction to turbulence models. *Department of Thermo and Fluid Dynamics, Chalmers University of Technology, Sweden*, 2003.

William J Devenport, Chittiappa Muthanna, Ruolong Ma, and Stewart A L. Glegg. Two-point descriptions of wake turbulence with application to noise prediction. *AIAA journal*, 39(12):2302–2307, 2001.

GE Elsinga, F Scarano, B Wieneke, and BW Van Oudheusden. Tomographic particle image velocimetry. *Experiments in Fluids*, 41(6):933–947, 2006.

Gerrit E Elsinga, Bernhard Wieneke, Fulvio Scarano, and Andreas Schröder. Tomographic 3d-piv and applications. In *Particle Image Velocimetry*, pages 103–125. Springer, 2008.

Jordi Estevadeordal and Stanley J Kleis. Double-helical pairing in plane mixing layers. *Physics of Fluids*, 11:1691, 1999.

J E Ffowcs Williams and L H Hall. Aerodynamic sound generation by turbulent flow in the vicinity of a scattering half plane. *Journal of Fluid Mechanics*, 40(04):657–670, 1970. URL http://www.journals.cambridge.org/abstract_S0022112070000368.

Sina Ghaemi and Fulvio Scarano. Multi-pass light amplification for tomographic particle image velocimetry applications. *Measurement science and technology*, 21(12):127002, 2010.

Sina Ghaemi and Fulvio Scarano. Counter-hairpin vortices in the turbulent wake of a sharp trailing edge. *J Fluid Mech*, 689:317–356, 2011.

RE Hayden, HL Fox, and RC Chanaud. Some factors influencing radiation of sound from flow interaction with edges of finite surfaces. *Technical Report, 1973-1976 Bolt, Beranek, and Newman, Inc., Cambridge, MA.*, 1, 1976.

Michael S Howe. *Theory of vortex sound*, volume 33. Cambridge University Press, 2003.

M.S. Howe. A review of the theory of trailing edge noise. *Journal of Sound and Vibration*, 61 (3):437–465, December 1978. ISSN 0022460X. doi: 10.1016/0022-460X(78)90391-7. URL http://linkinghub.elsevier.com/retrieve/pii/0022460X78903917.

MS Howe. The influence of surface rounding on trailing edge noise. *Journal of sound and vibration*, 126(3):503–523, 1988.

M.S. Howe. TRAILING EDGE NOISE AT LOW MACH NUMBERS. *Journal of Sound and vibration*, 225:211–238, 1999.

M.S. Howe. Trailing Edge Noise At Low Mach Numbers, Part 2: Attached and Separated Edge Flows. *Journal of Sound and Vibration*, 234(5):761–775, July 2000. ISSN 0022460X. doi: 10.1006/jsvi.1999.2861. URL http://linkinghub.elsevier.com/retrieve/pii/S0022460X99928614.

P. Moin J. C. R. Hunt, A. Wray. Eddies, stream, and convergence zones in turbulent flows. *Center for turbulence research report, CTR-S88*, 1988.

V. Koschatzky, P. D. Moore, J. Westerweel, F. Scarano, and B. J. Boersma. High speed PIV applied to aerodynamic noise investigation. *Experiments in Fluids*, 50(4):863–876, July 2010. ISSN 0723-4864. doi: 10.1007/s00348-010-0935-8. URL http://link.springer.com/10.1007/s00348-010-0935-8.

Claudia Kunze. *Acoustic and velocity measurements in the flow past an airfoil trailing edge*. PhD thesis, University of Notre Dame, 2004.

Marcel Lesieur. *Turbulence in fluids*, volume 84. Springer, 2008.

Michael J Lighthill. On sound generated aerodynamically. i. general theory. *Proceedings of the Royal Society of London. Series A. Mathematical and Physical Sciences*, 211(1107): 564–587, 1952.

Valerio Lorenzoni. Aeroacoustic Investigation of Rod-Airfoil Noise based on Time-Resolved PIV. 2008.

Kyle Lynch and Fulvio Scarano. Enhancing the velocity dynamic range and accuracy of time-resolved PIV through fluid trajectory correlation 2 . Fluid Trajectory Correlation Concept. (2011):9–12, 2012.

Carl D Meinhart, Time-averaged Velocity Fields, Steve T Wereley, and Juan G Santiago. A PIV Algorithm for Estimating. 122(June):285–289, 2000.

Theodoros Michelis. On the Interaction of NS-DBD Plasma Actuation with Flat Plate Boundary Layers. (December), 2012.

Scott C. Morris. Shear-Layer Instabilities: Particle Image Velocimetry Measurements and Implications for Acoustics. *Annual Review of Fluid Mechanics*, 43(1):529–550, January 2011. ISSN 0066-4189. doi: 10.1146/annurev-fluid-122109-160742. URL http://www.annualreviews.org/doi/abs/10.1146/annurev-fluid-122109-160742.

Stefan Oerlemans. *Detection of aeroacoustic sound sources on aircraft and wind turbines*. University of Twente, 2009.

Alan Powell. Aerodynamic noise and the plane boundary. *The journal of the Acoustical Society of America*, 32:982, 1960.

S. Probsting. Coherent Structures at the Serrated Trailing-Edge of a NACA 0012. 2011.

Stefan Pröbsting, Fulvio Scarano, Matteo Bernardini, and Sergio Pirozzoli. On the estimation of wall pressure coherence using time-resolved tomographic piv. *Experiments in Fluids*, 54 (7):1–15, 2013.

Stephen K Robinson. Coherent motions in the turbulent boundary layer. *Annual Review of Fluid Mechanics*, 23(1):601–639, 1991.

F Scarano. Tomographic PIV: principles and practice. *Measurement Science and Technology*, 24(1):012001, January 2013. ISSN 0957-0233. doi: 10.1088/0957-0233/24/1/012001. URL http://stacks.iop.org/0957-0233/24/i=1/a=012001?key=crossref.06bb53d64ea6b5ebccdce8da58d8006e.

J Schneiders, RP Dwight, and F Scarano. Vortex-in-cell method for time-supersampling of piv data. 2013.

Andrea Sciacchitano, Fulvio Scarano, and Bernhard Wieneke. Multi-frame pyramid correlation for time-resolved PIV. *Experiments in Fluids*, 53(4):1087–1105, July 2012. ISSN 0723-4864. doi: 10.1007/s00348-012-1345-x. URL http://link.springer.com/10.1007/s00348-012-1345-x.

Daniel W. Shannon. *Flow field and acoustic measurements*. PhD thesis, University of Notre Dame, 2007.

Daniel W. Shannon and Scott C. Morris. Experimental investigation of a blunt trailing edge flow field with application to sound generation. *Experiments in Fluids*, 41(5):777–788, September 2006. ISSN 0723-4864. doi: 10.1007/s00348-006-0200-3. URL http://link.springer.com/10.1007/s00348-006-0200-3.

M. Stanislas, K. Okamoto, C. J. Kähler, J. Westerweel, and F. Scarano. Main results of the third international PIV Challenge. *Experiments in Fluids*, 45(1):27–71, April 2008. ISSN 0723-4864. doi: 10.1007/s00348-008-0462-z. URL http://link.springer.com/10.1007/s00348-008-0462-z.

Christopher KW Tam and N Reddy. Prediction method for broadband shock-associated noise from supersonic rectangular jets. *Journal of aircraft*, 33(2):298–303, 1996.

Theodore Theodorsen. Mechanism of turbulence. In *Proceedings of the Second Midwestern Conference on Fluid Mechanics*, pages 1–18. Ohio State University, 1952.

B. E. Thompson and J. H. Whitelaw. Characteristics of a trailing-edge flow with turbulent boundary-layer separation. *Journal of Fluid Mechanics*, 157(-1):305–326, April 1985. ISSN 0022-1120. doi: 10.1017/S0022112085002397. URL http://www.journals.cambridge.org/abstract_S0022112085002397.

Daniele Violato and Fulvio Scarano. Three-dimensional evolution of flow structures in transitional circular and chevron jets. *Physics of Fluids*, 23(12):124104, 2011. ISSN 10706631. doi: 10.1063/1.3665141. URL http://link.aip.org/link/PHFLE6/v23/i12/p124104/s1&Agg=doi.

By M Wang. Computation of trailing-edge aeroacoustics with vortex shedding. 2005.

Meng Wang and Parviz Moin. Computation of Trailing-Edge Flow and Noise Using LES. 38 (12), 2000.

Peter Welch. The use of fast fourier transform for the estimation of power spectra: a method based on time averaging over short, modified periodograms. *Audio and Electroacoustics, IEEE Transactions on*, 15(2):70–73, 1967.

WW Willmarth and Bo Jang Tu. Structure of turbulence in the boundary layer near the wall. 1967.

Alec David Young and JH Paterson. Aircraft excrescence drag. Technical report, DTIC Document, 1981.

Appendix A

Boundary Layer Tripping

We know that surface imperfections can induce an earlier transition than on a smooth surface because they generate disturbances in the boundary layer in the form of eddies and vortices which modify the shape of the boundary layer velocity profile in their neighborhood and wake so that the boundary layer is rendered more unstable. In addition, the drag of the roughness is manifest in an increase of the boundary layer momentum thickness and the associated boundary layer Reynolds number and this will also tend to enhance the instability of the boundary layer and hasten the transition process.

If we consider an isolated excrescence located in the laminar boundary layer for a particular body in motion we find that there is a critical roughness height below which no significant effect on transition is apparent. This height depends primarily on the roughness shape, location, the pressure distribution over the body, the body Reynolds number, the external turbulence and on the transition position on the smooth surface. As the height is increased, the transition moves upstream until a second critical height is reached at which transition occurs just downstream of the roughness and no further transition movement occurs with further increase of roughness height. Young and Paterson (1981). The second critical roughness height is given by equation A.1.

$$k_{crit,2} = \frac{163.7 \times Re_x^{0.15} \times \nu}{U_o} \tag{A.1}$$

This equation gives a critical roughness height of the order of 1mm for the transition to occur almost quarter chord point for the freestream velocity of 10m/s.

Appendix B

Basics of PIV: Seeding, Imaging and Processing

B.1 Flow Seeding

In PIV measurement techniques, a microscopic particles are introduced to track the fluid flow. The concentration of tracer particle plays a vital role. It should be introduced in an appropriate amount so that it doesn't alter the fluid flow. The concentration of seeding tracer particle ranges about 10^9 and 10^{12} $particles/m^3$. Above this range it will start affecting the flows (which is also known as multiphase flows effects). The process is governed by the mass ratio $m_{fluid}/m_{particles}$, which for micron size droplets in air flows should not exceed the order of 10^{-3}. The three important properties of tracer particles need to be considered. Firstly, the tracer particles exactly follow the motion of fluid. Secondly, the tracer particles do not alter the motion of fluid. Thirdly, the tracer particles should have sufficient light scattering properties. In the flow medium, the tracer particles are randomly distributed and they are convected along the local flow trajectory without altering their properties Adrian (2005). The knowledge of mechanical principles for small particles immersed in fluid flows is critical in order to have accurate flow tracing.

B.1.1 Mechanical properties

In low speed motions the Stoke drag dominates the motion of the particles with respect to the difference between the particle velocity (V) and that of the surrounding fluid (U).

$$V - U = \frac{2}{9}a^2\frac{\rho_p - \rho_f}{\mu}\frac{dV}{dt} \tag{B.1}$$

where V-U is referred as settling velocity or slip velocity, d_p is the particle diameter, ρ_p density of the particles, ρ_f the density of the fluid, μ the dynamic viscosity and a the local acceleration

of a fluid parcel. The condition of buoyancy neutral particles $\frac{\rho_p - \rho_f}{\mu}$ allows to obtain particles tracers accurately following the flow. For liquid flows it is easy to achieved as compared to gas flows. Typical values of density ratios $\frac{\rho_p}{\rho_f} = 0(10^3)$ and particles with a smaller diameter $(0.5\mu m < d_p < 5\mu m)$ are employed.

$$\tau_p = d_p^2 \frac{\rho_p}{18\mu} \tag{B.2}$$

From the equation 5.3 , τ_p is a characteristics time and it is related to particle Stoke number S_k as given below:

$$S_k = \frac{\tau_p}{\tau_f} \tag{B.3}$$

Stoke number is a good indication for the ability of the tracers to follow the fluid given that $St << 1$. But due to practical limitations $St < 0.1$ is used.

B.1.2 Scattering properties of tracer particles

The requirements of accurate flow tracking and sufficient light scattering conflict with each other. Therefore, it requires a trade-off solution to obtain an optimum. The scattering efficiency of the particles depends on the ratio of refractive index n/n_f, wavelength of light λ^{-4} and particle diameter d_p. The micro-metric particles scattered light in the Mie regime. In this regime the particle diameter is comparable or larger than the light wavelength λ. The scattering efficiency is maximum at 180 degrees and 0 degrees and lower on the sides. Unfortunately most of the PIV technique is applied with a view oriented at 90 degrees where the scattered light intensity attains a minimum Adrian (2005).

B.2 Illumination

For PIV measurement techniques, lasers are used as an illumination sources. As a light source different kind of monochromatic lasers are used. These monochromatic lasers are differ in the laser material, power consumption, geometrical dimensions, resulting pulse energy, pulse repetition rate and wavelength of the emitted light. They can produce a pulsed, collimated and monochromatic light beam that can be easily shaped into a thin light sheet. Some lasers can be used in continuous wave mode(CW) while others emit light only in the form of short pulses with a duration from a few nanoseconds up to a hundred microseconds. Pulsed light sources are most used because of the high temporal definition of the illumination pulse (in order of nanoseconds) whereas CW lasers can be used when the flow velocity is limited and the duration of illumination can be controlled by the camera exposure time shutter (nowadays electronic). CW lasers are relatively less expensive and simpler than pulsed ones. Moreover no signal losses due to partial light sheet overlap can occur since a single light beam is used Adrian (2005).

B.3 Imaging

The images of the tracer particles are formed by the lens on the surface of an image sensor. The imaging of the particle is limited by diffraction due to the small particles diameters. This implies that the wavelength of the light has an influence on the aperture of the camera and as well as on the size of the particle image. The characteristics of imaging system is depended on focal length (f),aperture number ($f_{\#}$) which is defined as the ratio of focal length to the aperture diameter (D) and image magnification (M) which is defined as the ratio of the image distance d_i and object distance d_o. And its mathematical representation is presented below:

$$\frac{1}{f} = \frac{1}{d_i} + \frac{1}{d_0}; M = \frac{d_i}{d_0} \tag{B.4}$$

The effective particle diameter in combination of the geometric optics effect is given by equation 5.3.

$$d_{geom} = d_p M \tag{B.5}$$

where d_p is the effective particle diameter and then diffraction effect is given by:

$$d_{diff} = 2.44\lambda(1+M)f_{\#} \tag{B.6}$$

where λ is the wavelength of light source.

$$d_\tau = \sqrt{(Md_p)^2 + (d_{diff})^2} \tag{B.7}$$

An approximation of the resulting particle diameter using Euclidean sum of the above terms is given by eq 5.8. Also, the geometric image of the particle Md_p is often neglected as compared to the diffraction limited image diameter.

$$\delta z = 4.88\lambda f\#^2 \frac{M+1}{M}^2 \tag{B.8}$$

Above eq 5.8 is applicable for particle image diameter only for the particle images in focus. That is when the light sheet thickness Δz_0 is smaller than the focal depth δz of the optical system given by eq 5.9. A large value of the numerical aperture is desired to obtain a higher depth of field while a small value has a positive effect on the light intensity collected by the sensor, posing another trade-off which is especially critical for recordings at high repetition-rates where the power per light pulse decreases

B.4 Processing

The next step is image processing that need to be done after gathering images. These images are processed to extract and analyse the velocity vector fields. The basic idea is to find the shift of tracer pattern between two frames recorded at a known time separation of Δt and then the cross-correlation operator is applied where correlation peak indicates the particle shift Δx

in unit of pixels. The minimum correlation window size is restricted by the minimum number of tracer particles required for the accurate cross correlation. The average velocity of a fluid in the correlation volume is given by the following equation , where Δx is the particle shift, Δt time separation, M magnification factor, l_{px} physical pixel size (property of the sensor).

$$U = \frac{\Delta x M l_{px}}{\Delta t} + \frac{\epsilon M l_{px}}{\Delta t} \tag{B.9}$$

In order to have higher vector resolution and statistically independent velocity vectors, a small correlation windows are required without large overlap. But this requirement creates an issue that tracer particles might travel further than the linear dimension of the correlation window during defined time separation. This makes cross-correlation between the correlation windows impossible as long as the windows are centred on identical pixels in both frames. As a result there is an decrease in signal to noise ratio. This problem can be overcome by using multi-pass iteration procedure. In Multi-pass iteration procedure, a correlation process is repeated for windows of different sizes. During first iteration step, relatively large window size is used to have an initial idea for the velocity vectors which is used to apply a shift between correlation windows in the second iteration step. It also facilitates to reduce the correlation window size in the second iteration without losing correlation peak. The particle displacement must not be too small since this decreases the accuracy due to the constant error ϵ. There are certain pre-processing techniques are often applied in order to improve the image and cross- correlation quality. Preprocessing helps to remove spurious light by subtraction of the minimum for each individual pixel. Furthermore, in order to increase the reliability of vectors close to the reflecting surfaces, a normalisations such as multiplication by a constant and division by the average are used Probsting (2011). subsectionOptimization rules The cross relation operator is applied in order to find the shift of the tracer pattern between two frames recorded at time separation of Δt. The correlation peak indicates the particle shift Δx in units of pixels. There are important conditions need to follow for an optimal experiment. Firstly, The maximum in-plane displacement should be smaller than $\frac{1}{4}$of the window size. Secondly, The maximum out-of-plane displacement should be less that $\frac{1}{4}$ of the light sheet thickness. Thirdly, The maximum in-plane variation of particle image displacement for particles inside the same window should not exceed the particle image diameter.